Title
Characterization of the 3D nanostructure of Calcium Silicate Hydrates by using Transmission Electron Microscope (TEM)

Author
Viseshchitra, Panod

Publication Date
2021

Peer reviewed|Thesis/dissertation

Characterization of the 3D nanostructure of Calcium Silicate Hydrates by using Transmission Electron Microscope (TEM)

By

Panod Viseshchitra

A dissertation submitted in partial satisfaction of the

requirements for the degree of

Doctor of Philosophy

in

Earth and Planetary Science

in the

Graduate Division

of the

University of California, Berkeley

Committee in charge:

Professor Hans-Rudolf Wenk, Chair
Professor Jill Banfield
Professor Paulo J. M. Monteiro

Spring 2021

Characterization of the 3D nanostructure of Calcium Silicate Hydrates by using Transmission Electron Microscope (TEM)

Panod Viseshchitra

Abstract

Characterization of the 3D nanostructure of Calcium Silicate Hydrates by using Transmission Electron Microscope (TEM)

by

Panod Viseshchitra

Doctor of Philosophy in Earth and Planetary Science

University of California, Berkeley

Professor Hans-Rudolf Wenk, Chair

Calcium silicate hydrate (C-S-H) is the main hydration product of Portland cement that mainly contributes to concrete's physical and mechanical properties. The porosity of C-S-H plays a vital role in the durability-based performance of concrete. Most of the information about the microstructure of C-S-H now is only in 2D due to the complex morphologies of hydration products.

This dissertation aims to investigate synthetic C-S-H and C-A-S-H with various Ca/Si ratios and curing temperatures using Transmission Electron Microscope (TEM) tomography. The 3D reconstructions of all samples were done using the simultaneous iterative reconstruction technique (SIRT). The highest beam dose that doesn't damage the samples for TEM tomography is 5000 $e^-/(nm^2\ s)$ for all samples. The 3D reconstructions and selected ROI analysis confirm that there are only foil-like structures for all C-S-H and C-A-S-H samples. Both CPSD and CMIP reveal that most of the pore sizes of all samples are below 40 nm. However, C-S-H at Ca/Si ratio 1.0 and 1.6 seem to have pore sizes larger than 100 nm. The curing temperature causes a lower porosity in the structure of both C-S-H and C-A-S-H. However, the porosity is not affected by chemical composition.

Scanning transmission electron microscopy (STEM) is used to compare the results with TEM. The 3D results of both TEM and STEM tomography show no significant difference. Still, the continuous pore size distribution with CMIP simulations shows a remarkable difference. C-S-H at Ca/Si ratio 1.0 from TEM tomography has 3 dominant pore sizes at 22.2, 28.8 and 37.7 nm, while STEM tomography has only

one dominant pore size at 6.0 nm. The pore network's size of TEM_C-S-H 1.0 is significantly larger but less dense than STEM_C-S-H 1.0.

A preliminary study of a fluid flow model has been accomplished. Both porosity and permeability increase with samples higher Ca/Si ratio, and higher equilibrated temperatures. The successful model will enhance the understanding of the relationship of mechanical properties and porosity of cement and concrete.

TEM tomography combine with Xlib plugin in ImageJ shows the capability to determine the 3D nanostructure and pore networks of C-S-H and C-A-S-H. To determine the sustainability of cements and concrete, the understanding of the relationship of mechanical properties and porosity is needed. The resulting information of 3D nanostructure and pore analysis provide these critical information for developing a new generation of optimized green cement and concrete.

Table of Contents

Table of Figures

Acknowledgment

First of all, I would like to thank Prof. Hans-Rudolf Wenk. He is the best advisor I've ever met. He always supports me during a hard time, pushes me to do incredible things, and shows me what a good researcher should be. He also shaped my knowledge in mineralogy, Synchrotron techniques.

I cannot find words to express my gratitude to Prof. Paulo J.M. Monteiro, the best cement and concrete expert. He has built my knowledge through the classroom, experiments, publishing papers, and this dissertation.

Thanks to my wife for taking care of my life, our baby, and everything here. Without her sacrifice, I could never accomplish my degree.

With the financial support from SCG Cement-Building Material, I can study here without worrying about the expense.

Thanks to my colleagues for both Wenk and Monteiro group: Chase Chandler, Eloisa Zepeda-Alarcon, Jiaqi Li, Guoqing Geng, Ke Xu, Ying Tsun Su, Daniela Martínez. You were great friends and offered great support for technical and non-technical issues.

Thanks to my office mates in EPS: Li-Wei Chen, Dana Lapides, Runze Miao, Anna Clinger, Ari Melinger-Cohen, Naomi Intrator, Thomas Smart, Matthew Diamond, for all the stress-relief dinner and coffee breaks.

I would like to acknowledge people at NCEM: Peter Ercius, Alex Lin, Mary Scott, Rohan Dhall, Karen Bustillo, Chengyu Song, John Turner. They offered me an excellent opportunity to do great experiments via STEM tomography.

I would like to express my gratitude to Daniela Ushizima and Ravi A. Patel to get me through the world of coding and modeling.

I would like to acknowledge people at EML: Guangwei Min, Reena Zalpuri, Danielle Jorgens for supporting my TEM tomography experiment.

I wish to thank the staff at ALS: Nobumichi Tamura, Martin Kunz, David Shapiro, Young-Sang Yu for helping me through the synchrotron techniques.

It was a pleasure to work with the best learning and scientific community at UC Berkeley and Lawrence Berkeley National Lab. The staff at EPS is also important.

They did many administrative works, which are not easy to see but very important for me.

Finally, I would like to thank my parents. They have taught me how to be a good person. They always support everything I've made.

1. Introduction

Portland cement was first discovered by Joseph Aspin in 1824 (Bogue, 1947; Hewlett & Liska, 2019). Portland cement-based concrete has been used as the primary construction material for the modern infrastructure for over one hundred years (Monteiro et al., 2017). The reasons behind its success are attributed to its robust, excellent resistance to water, leading to a controllable and high-performance behavior, and to the low cost and global availability of the raw materials used in Portland cement manufacture and concrete production (Mehta & Monteiro, 2014). According to the U.S. Geological Survey, the yearly production of Portland cement has increased dramatically in the past century, with annual manufacture of 4.1 billion metric tons in 2018 (U.S. Geological Survey, 2018), adding 2.9 billion metric tons of CO_2 into the atmosphere and contributing significantly to global warming. Green concrete contains alternative compounds to reduce the carbon footprint during the manufacturing process (Imbabi et al., 2012; Phair, 2006). It uses less energy in its production and may contain industrial by-products such as fly ash or blast furnace slag, reducing the generation of CO_2. The change in existing technologies to produce efficient green concrete requires optimization of the micro/nano structure such that less cement will be needed in its manufacture. Some essential hydration products such as calcium silicate hydrate (C-S-H) consist of particles generally a few nanometers in size (McDonald et al., 2010; Scrivener & Nonat, 2011), which significantly contribute to the concrete mechanical behavior (Königsberger et al., 2018; Scrivener et al., 2004). Several imaging techniques have been used to characterize the pore network, such as transmission electron microscopy (TEM) (Taylor et al., 2015), Focused Ion Beam/ Scanning Electron Microscopy (FIB/SEM) (Holzer, Gasser, and Müench 2006; Münch and Holzer 2008), and X-ray imaging (Bae, Taylor, Shapiro, et al., 2015; Bossa et al., 2015; Li et al., 2019).

The reactive Portland cement powder, mainly consisting of tricalcium silicate (Ca_3SiO_5, or C_3S in the cement notation which C for CaO, S for SiO_2) and dicalcium silicate (Ca_2SiO_4, or C_2S), can be mixed with water to produce a hardened material through complex reactions that produce the main binding product: calcium silicate hydrate (C-S-H).

C-S-H formed during the hydration process is the main binding phase and primary contributor to the mechanical properties of most hydrated Portland cement and

concretes. The C-S-H phases have poorly ordered crystal structures resembling the mineral tobermorite ($Ca_5Si_6O_{16}(OH)_2 \cdot 7H_2O$) (Bonaccorsi et al., 2005; H. F. W. Taylor, 1997). The poor crystallinity and short-range order character of C-S-H have prevented a satisfactory structural description with conventional X-ray diffraction techniques (H. F. W. Taylor, 1992). To better understand the C-S-H structure, a precise 3-dimensional model of C-S-H at the nanoscale is needed.

The porosity of C-S-H plays a crucial role in the durability-based performance of concrete. The size distribution and connectivity of the pores determine the ability of fluids and ions to flow through the network, potentially degrading the material. The nanostructure of C-S-H determines both the porosity and the pore size distribution. To date, there have been several studies on the nanostructure and morphology of a variety of Portland-cement-based systems (Bae, Taylor, Hernández-Cruz, et al. 2015; Bae, Taylor, Shapiro, et al. 2015; Korpa, Kowald, and Trettin 2009; Richardson 2000; Taylor, Richardson, and Brydson 2010). While such studies answer many questions, such as phase development in the system, the results of these techniques, including scanning electron microscopy, are distilled into two-dimensional (2D) information that provides only limited, often inferred, volumetric information of the nanostructure, and the pore network for a bulk paste. Simulations can also be used for these investigations (e.g. Garboczi & Bentz, 1992; Navi & Pignat, 1999). Due to the complex nature of cement hydration and the sensitivity of the products formed, only a few studies of the three-dimensional (3D) structure at the nanoscale have been completed (Song et al., 2019).

Transmission electron microscopy (TEM) can image specimens at very high resolution. It is widely used in materials science, including observations of cement, for example, to observe the morphology of hydration products of cements (Richardson, 1999, 2008; Richardson & Groves, 1992; Richardson, Skibsted, Black, & Kirkpatrick, 2010; Taylor et al., 2010). to characterize the effect of mineral admixtures, such as fly ash, slag, and metakaolin (Trusilewicz et al., 2012), on the hydration reactions (Bullard et al., 2011).

Electron tomography uses TEM images to reconstruct the 3D structure of an object from a series of projection images from different viewing angles. This method has been applied to many porous systems in materials science, such as in the imaging of nanoscale dendrites (Saghi et al., 2008). A recent study (Taylor et al., 2015) used electron tomography to investigate the nanostructure and pore network of C-S-H and found two separate networks of pores that are most likely attributed to two

particles of the same phase in different orientations. Due to the sensitivity of C-S-H to the electron beam, beam damage still occurred, and improvements are needed to develop a robust protocol for TEM tomographic studies of cementitious materials. To acquire tomographic tilt series, the sample is rotated, and a series of 2D projection images is measured at different tilt angles (Ercius et al., 2015). This research studied synthetic C-S-H instead of hydrated C3S because of the desire to have only one phase in the system. The 3D reconstruction method used in this experiment is the simultaneous iterative reconstruction technique (SIRT) method (Miao et al., 2016).

Scanning transmission electron microscopy (STEM) is another mode of TEM. STEM satisfies the incoherent imaging approximation in which diffraction and phase contrast is decreased, and the image intensity depends on the sample thickness and the atomic number (LeBeau et al., 2008). Also, the digital control of the beam in STEMs can minimize radiation damage (Marks, 1999). With STEM, we can reach higher magnification and less beam damage compared to conventional TEM (Scott et al., 2012).

Combining of electron tomography and model analysis giving detail of pore size distribution and permeability. This study investigates and compares the 3D structure of C-S-H and C-A-S-H with various Ca/Si ratios at the nanoscale using 3D electron tomography. The resulting information of pore analysis is critical for the development of a new generation of optimized green cement.

2. Literature review

2.1 Portland cement and Concrete

Cement is a material that becomes rigid and develops compressive strength, properties known as setting and hardening when hydration reactions with water take place. It is produced by heating a mixture of limestone ($CaCO_3$) and SiO_2 with traces of Al_2O_3 and Fe_2O_3 up to 1450°C. In the heating process, $CaCO_3$ decarbonates to form CaO, and then, four phases are formed at higher temperatures undergoing clinkering reactions. The typical elemental composition of the finished product, clinker, is about 65% CaO (C), 25% SiO_2 (S), 5% Al_2O_3 (A), 3% Fe_2O_3 (F) and 2% of other components. Some gypsum (calcium sulfate) is added to the clinker, in order to slower the hydration reaction, and the mixture is ground to form cement. Cement contains 4 main hydraulic phases: C_3S or alite (Ca_3SiO_5), C_2S or belite (Ca_2SiO_4), C_3A or tricalcium aluminate ($Ca_3Al_2O_6$) and C_4AF or calcium aluminoferrite ($Ca_2(Al, Fe)O_5$) (Taylor 1997).

Tricalcium silicate (C_3S or alite) is stable within the temperature range of 1250-1800 ºC. The high-temperature forms can be stabilized at room temperature by adding ions from the raw materials used in cement manufacture, and it is this impure C_3S which is known as alite. Alite is normally monoclinic. The most common ions that alite contains in clinkers are Mg^{2+}, Al^{3+}, Fe^{3+}, K^+, $Na^{+,}$ and SO_3.

Dicalcium silicate (C_2S or belite) is found in clinkers is typically βC_2S, which is stabilized at room temperature with substituent ions. The ions found in solid solution are mainly Al^{3+}, Fe^{3+}, Mg^{2+}, K^+, SO_4^{2-} and PO_4^{3-}. The presence of alkalis, such as K^+, stabilizes βC_2S with respect to γC_2S after the clinkering process during cooling.

Tricalcium aluminate (C_3A) is cubic when pure. It reacts vigorously with water, but the strength of the product is low. It can also contain substituent ions such as Fe^{3+}, Mg^{2+}, Na^+, K^+ , and Si^{4+}.

Calcium aluminoferrite (C_4AF) is the only phase of the particular compositions of ferrite that is found in clinkers. Some foreign ions can also be found in this phase, the most common being Mg^{2+}, Si^{4+}, and Ti^{4+}. Increasing the A/F ratio enhances the reactivity of calcium aluminoferrite with water, which is moderate in general.

The reaction of tricalcium silicate with water gives two hydration products (Equation 2.1).

$$2C_3S + 7H \rightarrow C_3S_2H_4 + 3CH \qquad \text{Equation 2.1}$$

The products are an almost amorphous calcium silicate hydrate phase and portlandite (calcium hydroxide, CH) (Taylor, 1997). This phase has the form of hexagonal crystals and has been found to be present as finely dispersed microcrystals in cement pastes of low water to solid ratio (Groves, 1981), or large imperfect crystals in C_3S pastes (Groves et al., 1986). The calcium silicate hydrate phase is named C-S-H, where the hyphens imply that its chemical composition can vary.

In hydration, the quantity of silicate species changes in C-S-H. The isolated silicate tetrahedra in C_3S are transformed to disilicate ions, and a higher degree of polymerization appears over time. Polymerization occurs in chains rather than sheets or 3D networks. After six months, the dimer content reaches a maximum of around 60% and decreases to about 50% after one year. Meanwhile, the content of polymeric species rises to 50% from the first year to 30 years of hydration (Mohan & Taylor, 1982).

The reaction of dicalcium silicate with water also gives C-S-H and CH (Equation 2.2).

$$2C_2S + 5H \rightarrow C_3S_2H_4 + CH \qquad \text{Equation 2.2}$$

The proportion of produced CH is about a fifth of the amount produced in the hydration of tricalcium silicate. The rate of hydration of C_2S is much lower than for tricalcium silicate. The rate of hydration does not affect the C-S-H composition, which is the same composition that results from hydrating C_3S (Taylor 1997).

2.2 Calcium Silicate Hydrate (C-S-H)

There are several minerals such as gyrolite, xonotlite, clinotobermorite, tobermorite 9Å, tobermorite 11Å, tobermorite 14 Å and jennite that have similar structure like calcium silicate hydrates. The comparison of XRD patterns of C-S-H formed in cement pastes with those of the natural minerals tobermorite, and jennite has shown that C-S-H has some structural features related to them (Bonaccorsi, Merlino, and Taylor 2004; Elena Bonaccorsi, Merlino, and Kampf 2005). Synthetic imperfect forms of tobermorite and jennite formed in aqueous suspensions, called C-S-H (I) and C-S-H (II) are also related to C-S-H (Taylor 1997). Thomas et al. (2010) have shown that C-S-H has a much higher atomic packing density than both tobermorite and jennite. This may be due to its defective atomic structure and to nano solid effects linked to its nanoparticulate morphology. The example of a TEM image of C-S-H at Ca/Si ratio 1.6 is shown in Figure 2.1.

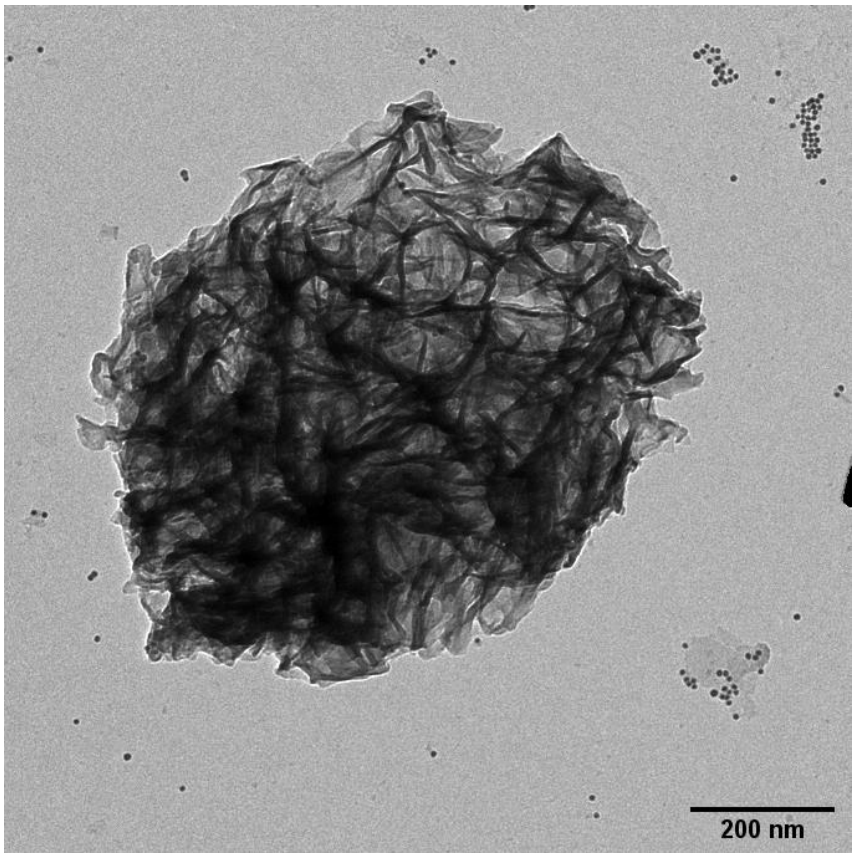

Figure 2.1 TEM image of C-S-H at Ca/Si ratio 1.6

Richardson and Groves (1992, 1993) proposed a general model that could be interpreted from the tobermorite/jennite or tobermorite/calcium hydroxide perspective. This model did not fix the level of protonation of the silicate chain. The generalized model is very similar to many previous models for the structure of C-S-H, but its generality allows for the specific inconsistencies of other models to be compensated.

The widely proposed molecular structure of C-S-H, at curing temperature below 80 °C, is similar to tobermorite 14Å (Bullard et al., 2011). The current model of C-S-H consists of complex layers of central octahedral calcium oxide sheets with tetrahedral silicate chains on both sides, which are attached with a periodicity of three tetrahedra (Figure 2.2). The space between two complex layers contains additional calcium cations and H_2O.

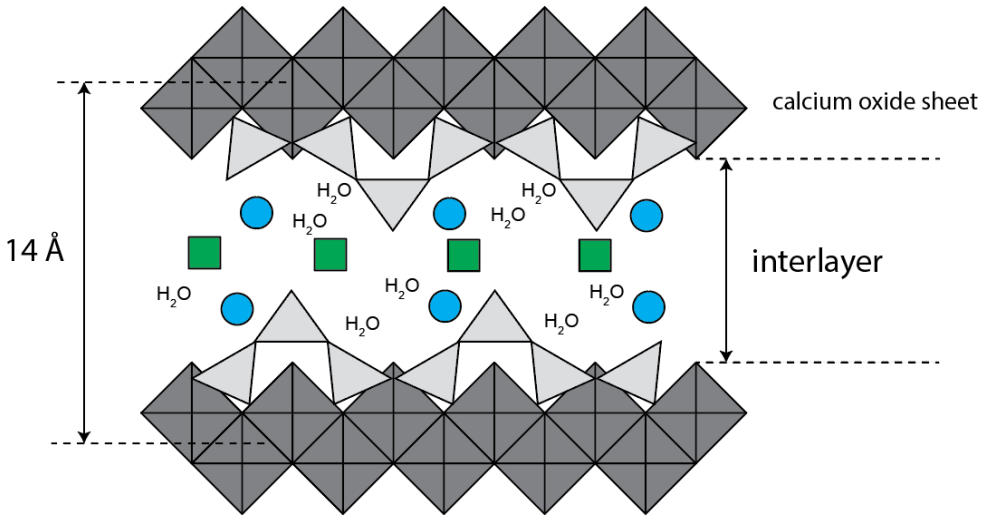

Figure 2.2 Schematic of the atomic structure of C-S-H. The layers of octahedral calcium oxide sheet (CaO_6) are drawn in dark grey, whereas the light grey triangles are SiO_4^{4-} tetrahedra. The interlayer contains water and positively-charged species (blue circles and green squares, respectively) that can neutralize the structure (e.g. Ca^{2+} and/or K^+) (Bonaccorsi et al., 2005)

2.3 Calcium Alumino Silicate Hydrate (C-A-S-H)

C-A-S-H is another key binding phase and a primary contributor to the mechanical properties of most hydrated cement and concretes. Increasing amounts of Al-containing cementitious precursors, mainly industrial wastes, e.g. fly ash, ground granulated blast furnace slag (GGBFS), and calcined clay, are being used in modern cements. These cements form C-A-S-H with higher Al content on hydration. The example of C-A-S-H at Ca/Si ratio 1.0 Al/Si ratio 0.05 is shown in Figure 2.3.

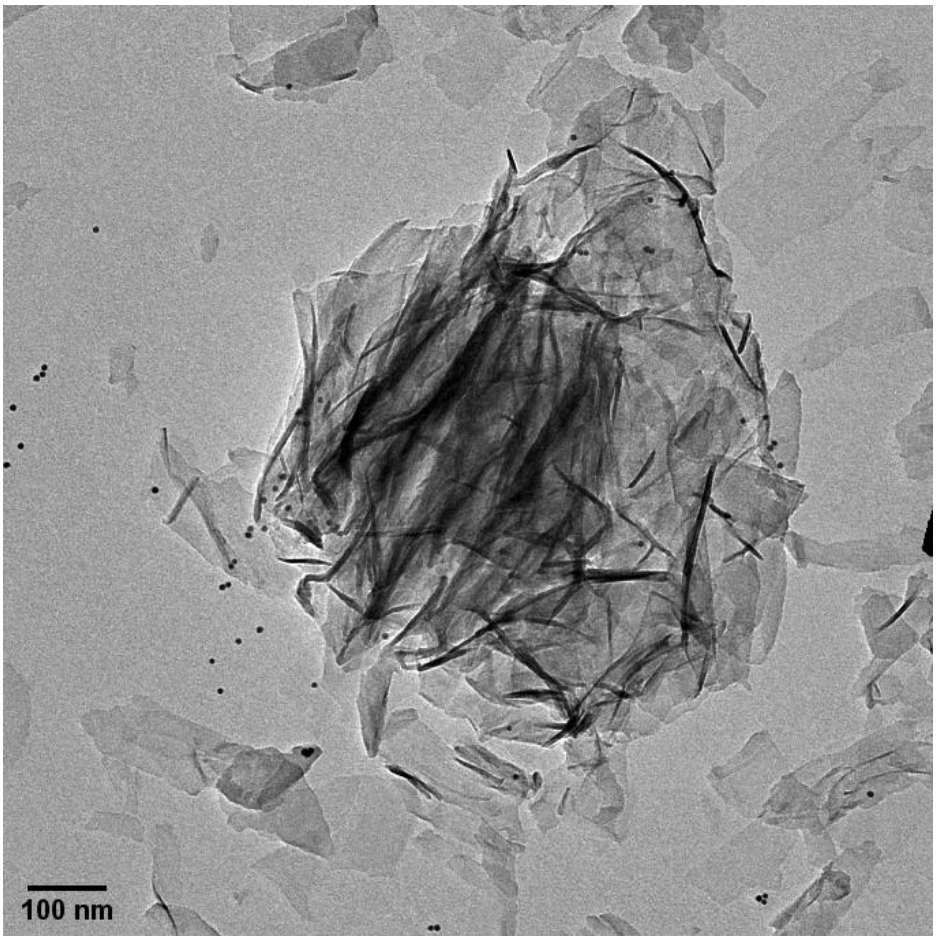

Figure 2.3 TEM image of C-A-S-H at Ca/Si ratio 1.0, Al/Si ratio 0.05

The atomic structure of non-cross-linked C-A-S-H is similar to non-cross-linked C-S-H, but the aluminate tetrahedron is incorporated in the silicate chain of C-S-H at bridging sites. The substitution of tetrahedral silicate by tetrahedral aluminate

gives more negative charged basal layer, which requires more cations to charge-balance the entire structure compared to C-S-H (Abdolhosseini et al., 2012). The atomic structure of C-A-S-H at a curing temperature of 80 °C or higher is similar to Al-tobermorite 11Å (Merlino et al., 2001). Double chains of tetrahedral aluminosilicate in cross-linked C-A-S-H are formed by cross-linking of two bridging sites (Yang et al., 2018). The atomic structure of C-A-S-H is shown in Figure 2.4.

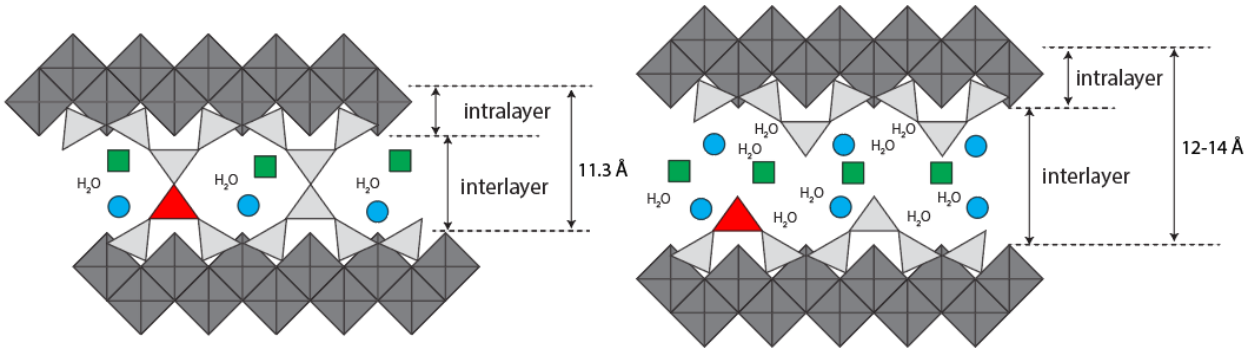

Figure 2.4 Schematic of the atomic structure of non-cross-linked C-A-S-H (left) and cross-linked C-A-S-H (right). The layers of octahedral calcium oxide sheet are drawn in dark grey, whereas the light grey triangles are SiO_4^{4-} tetrahedra. The red triangles represent aluminate tetrahedra at bridging sites and cross-linking sites. The interlayer contains water and positively-charged species (blue circles and green squares, respectively) that can neutralize the structure (e.g., Ca^{2+} and/or K^+)

The solid phase for both of C-S-H at Ca/Si ratio 1.0 and C-A-S-H at Ca/Si ratio 1.0, Al/Si ratio 0.05 was analyzed by X-ray diffractometry (XRD) and only 3 peaks of C-S-H is observed at around 8°, 34°, and 37° 2θ . There is no portlandite nor evidence of carbonation. The XRD results are shown in Figure 2.5.

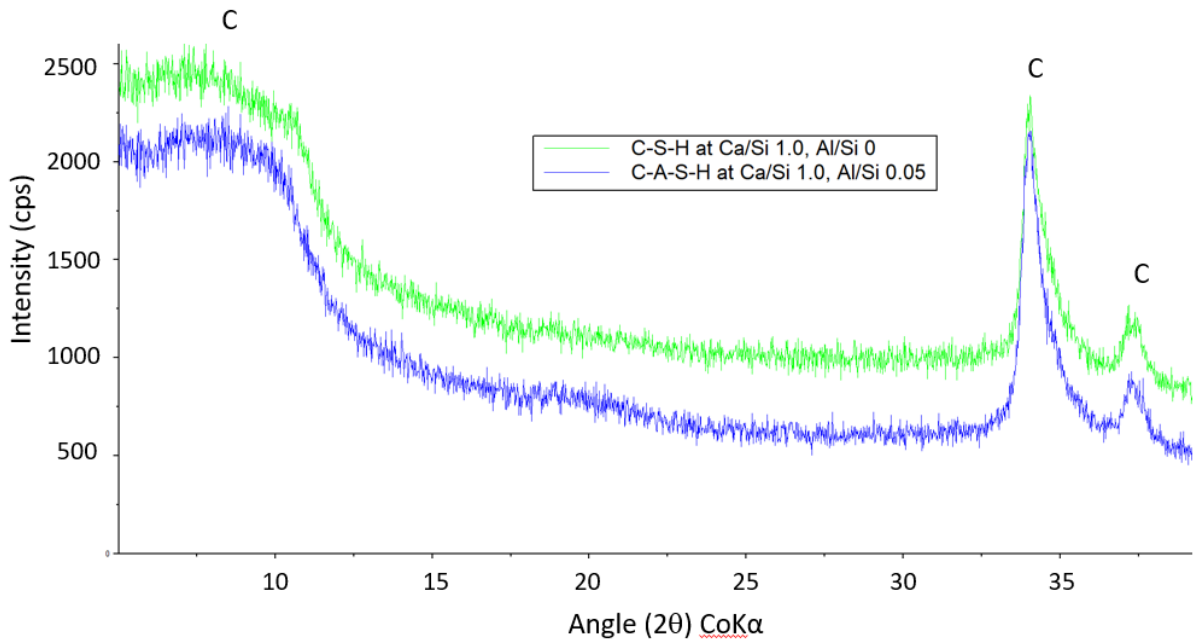

Figure 2.5 XRD results of C-S-H at Ca/Si ratio 1.0 (green line) and C-A-S-H at Ca/Si ratio 1.0, Al/Si ratio 0.05 (blue line). Three main peaks of both C-S-H and C-A-S-H are at around 8°, 34°, and 37° 2θ.

3. Transmission Electron Microscope (TEM) tomography

3.1 Introduction

The TEM is based on the transmission of an electron beam through a very thin sample (thickness less than 100 nm). The field emission gun generates a beam of electrons accelerated to high voltage (the TEM working voltage). The electron beam is first focused by the two condenser lenses on the sample, which largely determines the spot size of the experiment. The beam is limited by the condenser aperture, knocking out high-angle electrons. The beam strikes the sample, and parts of it are transmitted. This transmitted beam is focused by the objective lens into an image. Optional Objective and Selected Area apertures can restrict the beam; the Objective aperture is enhancing contrast by blocking out high-angle diffracted electrons, the Selected Area aperture enabling the user to examine the periodic diffraction of electrons by ordered arrangements of atoms in the sample. The image is passed through the column through the intermediate and projector lenses, being enlarged all the way. The image hits the phosphor screen, and light is generated, allowing the user to see the image. (Reimer & Kohl, 2008; Williams & Carter, 2009).

Three types of images can be taken in TEM, which are bright field, dark field, and high-resolution images. In the bright field mode, an aperture is inserted in the back focal plane of the objective lens to block the diffracted beams. This results in a contrast image where the areas of the sample that diffract more appear dark while the areas of the sample where the electron beam is more transmitted straight through appear bright. TEM bright field images have been widely used in cement and concrete research. For taking images of cementitious samples, it is important not to go to much higher magnification because serious beam damage can be induced in the sample. The higher magnification means the smaller area but the same intensity. Hydrated cement has low melting temperatures and low thermal conductivity, leading to thermal damage (Richardson, 2002).

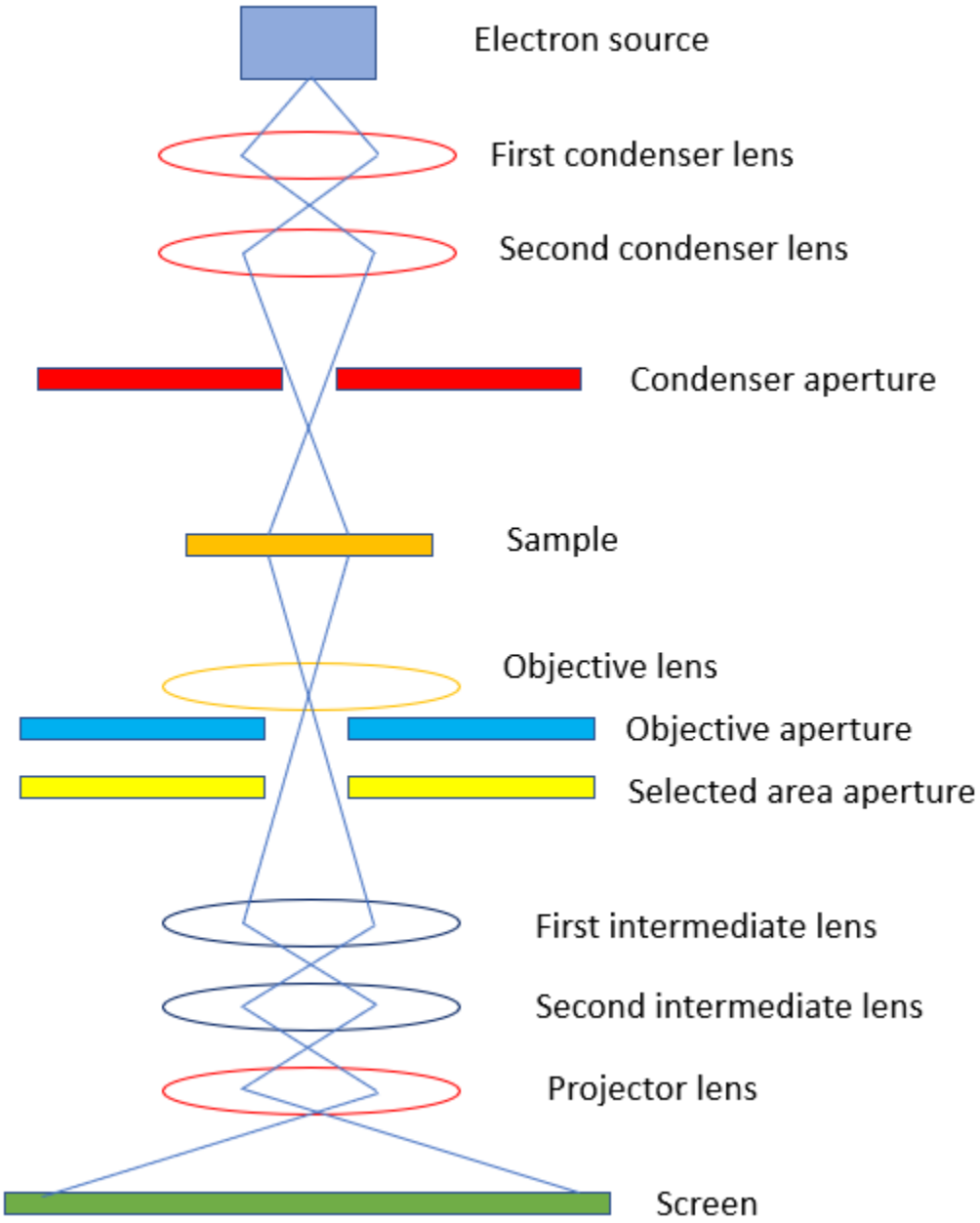

Figure 3.1 Schematic diagram of TEM (Williams & Carter, 2009).

3.2 Tomography

The term tomography has been used to describe the process of imaging by sections (Penczek, 2010). The tomography was done in 5 steps, including sample preparation, data acquisition, data alignment, data reconstruction, and object visualization.

The sample can be prepared the same way as a conventional TEM sample. For data acquisition, the sample is tilted to the highest degree until the view is blocked by the instrument. The number of images can be different while ensuring the tilting range is at the full possible range to record more images. The angle increment is normally set as 2°, 1° or 0.5°. Images in a tilt series were manually aligned to a common coordinate system then shifted and rotated to center the axis of rotation. To align the data, we have to choose one fixed point (FP) (Brandt, 2006; Liu et al., 1995). This fixpoint should be easy to see and have high contrast in all images. Gold fiducial markers are usually added to the system to generate the dominant FP. Then we have to align the FP to be in the same position in both X and Y directions.

Data reconstruction is a mathematical process that is straightforward using existing computing programs. There are many different algorithms for reconstructing a 3D object from a tilt series, such as simple back projection (BP) (Berry et al., 1970; Bracewell & Riddle, 1967), weighted-back projection (WBP) (P. F. Gilbert & Aaron, 1972), algebraic reconstruction technique (ART) (Gordon et al., 1970), simultaneous iterative reconstruction technique (SIRT) (P. Gilbert, 1972). In electron tomography, tilt ranges are limited to 130 degrees. This results in a missing wedge of information, obviously as artifacts in a reconstruction (Arslan et al., 2005; Midgley & Weyland, 2003). The missing wedge in a weighted back-projection reconstruction can be directly visualized by reducing the threshold intensity value displayed in the color map and then viewing the object down the experimental tilt axis. Although several techniques, including proper sample preparation, data acquisition, and denoising methods, can decrease the experimental errors and reduce noise, iterative tomographic reconstruction algorithms are more suitable than noniterative methods. The in-depth detail of some reconstruction methods is provided in the next part.

Visualization of the reconstructed volume is done either by volume rendering or by surface rendering. The volume rendering was optimized by adjusting the color and the transparency of the different parts. For the surface rendering, an initial segmentation was obtained by thresholding the data(Kübel et al., 2005). The alignment, reconstruction, and visualization were done using the tomviz software

(Levin et al., 2018). Tomviz is an open-source software for volumetric visualization and data processing, especially for electron tomography. The tomviz platform based on Python allows graphical analysis of 3D datasets.

3.3 The reconstruction methods

3.3.1 Weighted-Back projection

The basic method is Simple Back Projection, which projects 2D images back into 3D, and compares the projections acquired at different angles to try to recover the structure of the 3D object. In this study, a weighted-back projection algorithm, which builds on these more basic algorithms to produce high-quality reconstructions, is used. The relation between the three-dimensional Fourier transform and the mass density distribution (Reimer & Kohl, 2008) of the specimen is written as:

$$F(q_x, q_y, q_z) = \iiint \rho(x, y, z) \exp\left[-2\pi i\left(q_x x + q_y y + q_z z\right)\right] dxdydz \qquad \text{Equation 3.1}$$

Where $\rho(x, y, z)$ is the specimen density distribution from a series of projections. However, a micrograph with the electrons incident parallel to z corresponds to a central section through the Fourier space in the q_x, q_y plane, so the transform reduces to:

$$F(q_x, q_y, 0) = \iint \rho(x, y, z) \exp\left[-2\pi i\left(q_x x + q_y y\right)\right] dxdy \qquad \text{Equation 3.2}$$

We will get $F(q_x, q_y, q_z)$ from a tilt series, which is equivalent to a bundle of central sections through the Fourier space, so ρ(x, y, z) can be calculated by an inverse Fourier transform.

In electron tomography, tilt ranges are limited to about 140 degrees due to shadowing of the specimen holder and space limitations in the TEM specimen chamber. This results in a missing wedge of information, which produces artifacts in a reconstruction (Arslan et al., 2005; Midgley & Weyland, 2003). The missing wedge in a weighted back-projection reconstruction can be directly visualized by reducing the threshold intensity value displayed in the color map and then viewing the object down the experimental tilt axis. Although several techniques, including well sample preparation, data acquisition, and denoising methods, can decrease

the experimental errors and reduce noise, iterative tomographic reconstruction algorithms are more suitable than noniterative methods.

3.3.2 Simultaneous iterative reconstruction technique (SIRT)

The concept of SIRT is to iterative reconstruct a system of linear equations to reduce artifacts. In other words, we repeat doing WBP until we get a better result. We start with the linear system

$$Ax = b \quad (1) \qquad \text{Equation 3.3}$$

where x represents the image, b represents the projections, and matrix A represents the image process (forward projection). The transposed matrix, $A^{T,}$ back-projects the projections onto the reconstruction area. SIRT takes forward and back projections repeatedly. The update equation is

$$x^{t+1} = x^{(t)} + GA^{T}R\,(b - Ax^{(t)}) \qquad \text{Equation 3.4}$$

Where G and R are diagonal matrices that contain the inverse of the sum of the columns and rows of the system matrix. Iterations start with $x^{(0)}=0$. The updated equation then does the following things. The current reconstruction at $x^{(t)}$ is forward projected, $Ax^{(t)}$. The result is subtracted from the originals: $b - Ax^{(t)}$. The difference is the back-projected, which is done by multiplying with A^{T}, but weighted with G and R. This results in the correction factor $GA^{T}R\,(b - Ax^{(t)})$. The corrective factor is added to the current reconstruction, and the whole process is repeated.

3.4 Experimental Methods

3.4.1 Materials

C-S-H and C-A-S-H was synthesized by mixing calcium oxide (CaO), silica fume (SiO_2), and monocalcium aluminate ($CaO \cdot Al_2O_3$) at different Ca/Si and Al/Si molar ratios with water. CaO was obtained by burning calcium carbonate ($CaCO_3$, Merck, pro analysis) at 1000 °C for 12 hours. SiO_2, provided by Aerosil 200, Evonik, was chosen for its high specific surface area. The synthesis process and all the sample handling were carried out in an N_2 filled glovebox to prevent CO_2 contamination. The samples were stored in 100 mL high-density polyethylene (HDPE) containers placed on a shaker moving at 100 rpm and equilibrated at various temperatures. For each equilibration time, a separate sample was prepared. After equilibrated for 182 days, the solid and the liquid phase were separated by filtration using a 0.45 µm nylon filter. Each sample detail is shown in Table 3.1.

Table 3.1 Detail of Ca/Si ratio, Al/Si ratio, and equilibrated temperature for each sample.

Ca/Si ratio	Al/Si ratio	Equilibrated Temperature (°C)	Angle Start (°)	Angle End (°)	Angle increment (°)
0.6	0.00	20	-60	60	1
0.8	0.00	20	-70	70	2
1.0	0.00	20	-45	70	1
1.2	0.00	20	-65	65	1
1.4	0.00	20	-60	60	2
1.6	0.00	20	-60	60	1
1.0	0.00	7	-70	70	2
1.0	0.00	50	-65	65	1
1.0	0.00	80	-70	70	1
1.0	0.05	7	-65	65	2
1.0	0.05	50	-65	65	2
1.0	0.05	80	-65	65	1

3.4.2 Electron Tomography

The electron tomography requires several steps, including sample preparation, data acquisition, data alignment, data reconstruction, and object visualization, as described in section 3.2. The sample was suspended in ethanol and deposited on a 200 mesh ultra-thin copper hexagonal grid with carbon film support (CF200H-Cu-UL, Electron Microscopy Sciences). 10 nm gold fiducial markers (Aldrich) were deposited to aid in tilt series alignment. Data acquisition was acquired on a Tecnai 12 TEM (Figure 3.2), operating at 120 kV. All images were acquired automatically using the SerialEM software. The angle start, angle end, and angle increment are shown in Table 3.1. The number of images for each sample is equal to the total images(angle start plus angle end) divided by the angle increment.

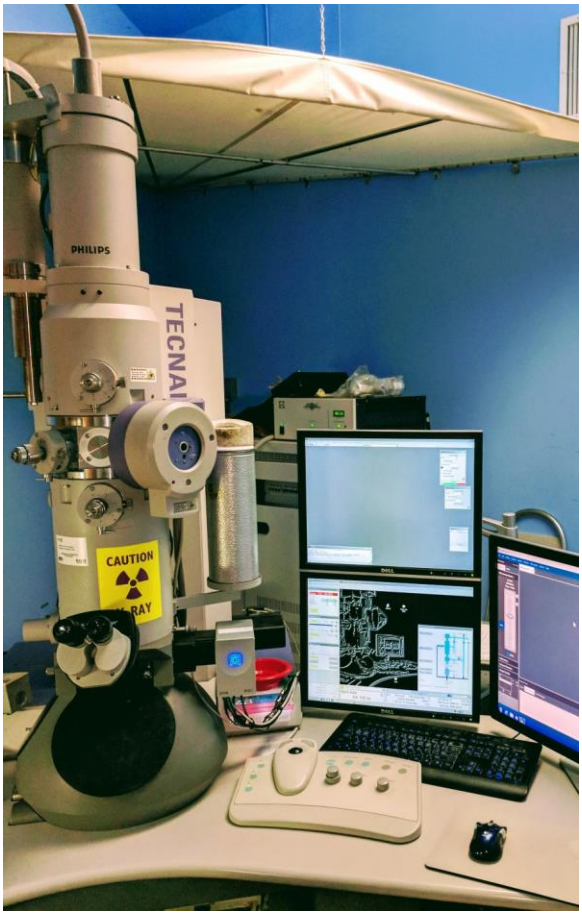

Figure 3.2 TEM Tecnai 12 at Electron Microscope Lab (EML), UC Berkeley

The alignment, reconstruction were done by using the IMOD software (Kremer et al., 1996). More detail on the alignment and reconstruction are in section 7.1 and 7.2. Visualization of the reconstructed volume was done either by volume or surface rendering. The volume rendering was optimized by manually adjusting the color and the transparency. The visualizations were done using the Tomviz 1.8 software (Levin et al., 2018) and napari (Sofroniew et al., 2021). IMOD, Tomviz, and napari are open source software for volumetric data processing and visualization, especially for electron tomography. The example of a TEM image of C-S-H with Ca/Si ratio 1.0 is shown in Figure 3.3.

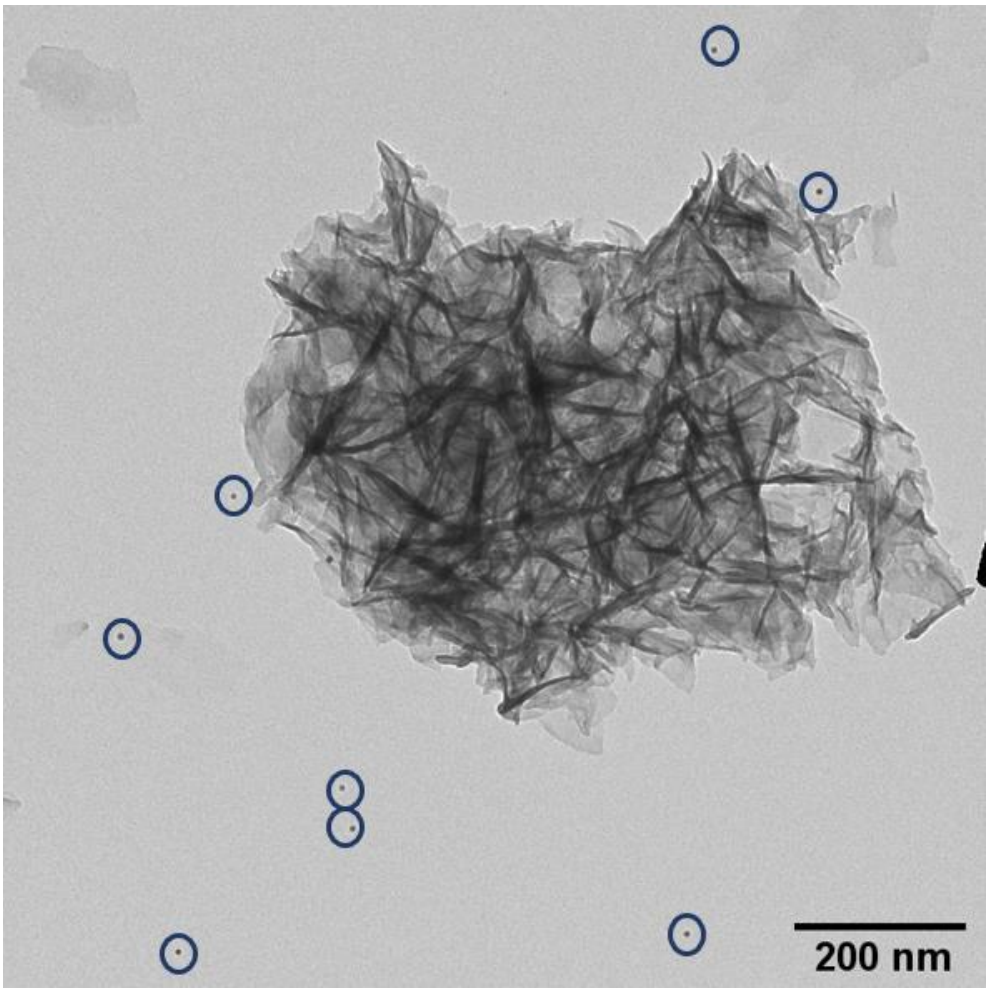

Figure 3.3 2D image of C-S-H with Ca/Si ratio 1.0. The black dots in blue circles are gold fiducial markers.

3.4.3 Model analysis

The pore analysis of the reconstructed models was obtained by using the Fiji/ImageJ software. The segmentation, which allows isolating pores to C-S-H, is based on global thresholding with the Otsu algorithm (Otsu, 1979). The porosity is calculated based on the ratio of the white area (particles) divided by the total area. The continuous pore size distribution (CPSD) and continuous pore size distribution with mercury intrusion porosimetry simulation (CMIP) were determined by using the Xlib plugin (Münch & Holzer, 2008) in ImageJ. For CPSD, the pore space is separated into regions of different radii that can be filled with objects of different radii (Münch & Holzer, 2008). The sizes of these radii are attached to the respective locations. For CMIP, same PSD definition as for the CPSD. However, the balls of different radii are intruded into the pore volume from one of the faces of the 3D image cube or from one of the edges of the 2D image, respectively. This definition of the PSD corresponds to the data collected by mercury intrusion porosimetry (MIP) (Münch & Holzer, 2008).

3.5 Results and Discussion

3.5.1 Beam damage on TEM tomography

Beam damage is a major problem in electron tomography due to the longer time to complete the whole series of images. Our particles were sensitive to beam irradiation, so we were careful to limit the dose and to check for damage before 3D reconstruction.

$$\text{The electron dose } (e^-/(nm^2\ s)) = \frac{M}{D \cdot A \cdot E} \qquad \text{Equation 3.5}$$

Where M is the average number of counts per pixel (counts / pixel).

D is the number of counts per electron (counts per electron).

A is the area per pixel (nm^2 / pixel).

E is the acquisition time per image (second).

A beam dose of 5000 $e^-/(nm^2\ s)$ is suitable for this research and applies to all conventional TEM tomography for both C-S-H and C-A-S-H. The example of the effect of beam damage is shown in Figure 3.4. As seen in equation 3.5, the magnification is directly proportional to M, so the higher magnification means the greater beam damage.

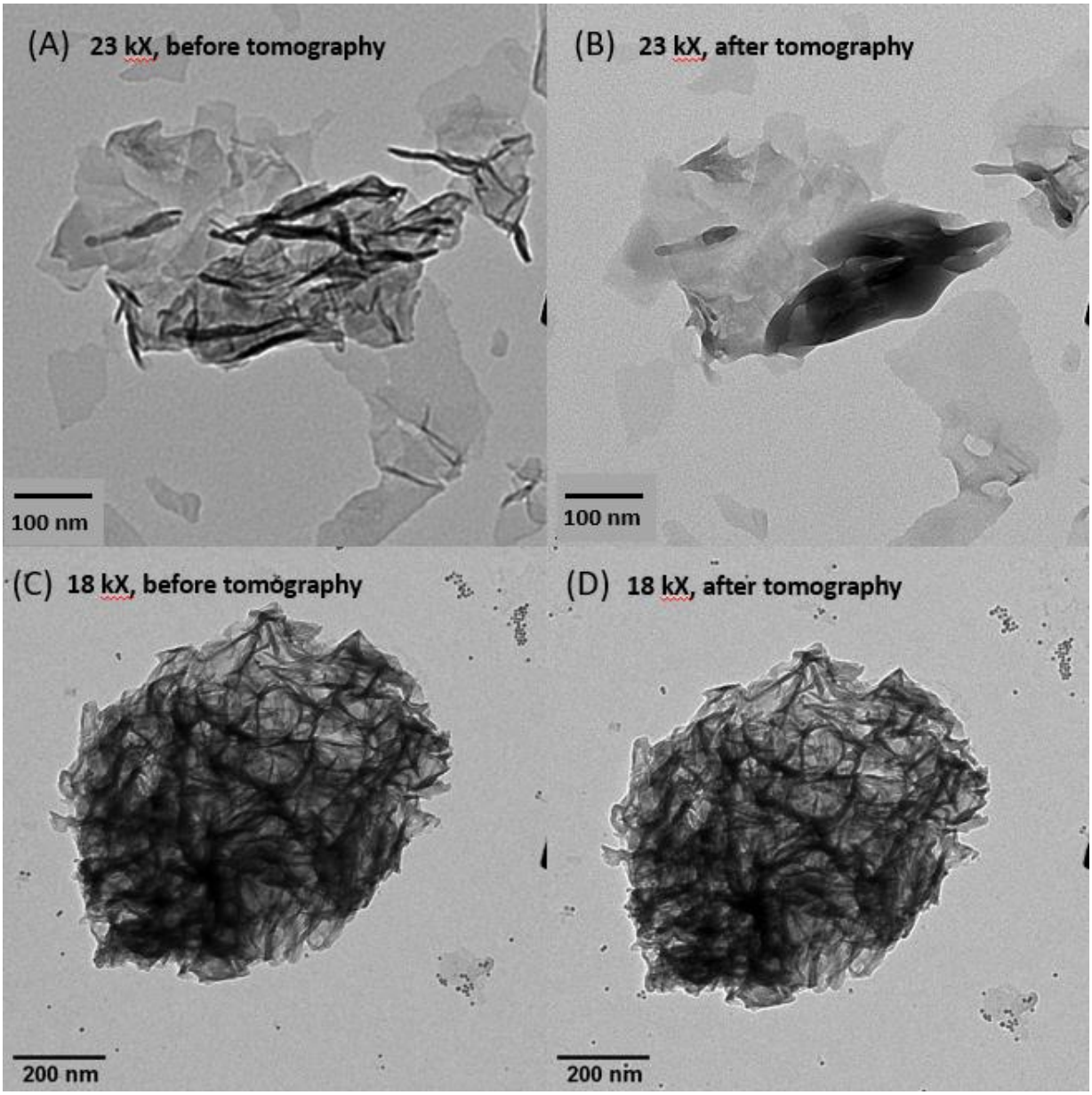

Figure 3.4 Compare the 2D images of C-S-H 1.6 at 0° rotation (A) before and (B) after tomography at 23 kX magnification. (C) before and (D) after tomography at 18 kX magnification.

3.5.2 Effects of Ca/Si ratio on the structure of C-S-H

The 2D images and 3D reconstructed models are shown in Figure 3.5 to Figure 3.10. The distinguished black dots that may appear in several models are gold fiducial markers.

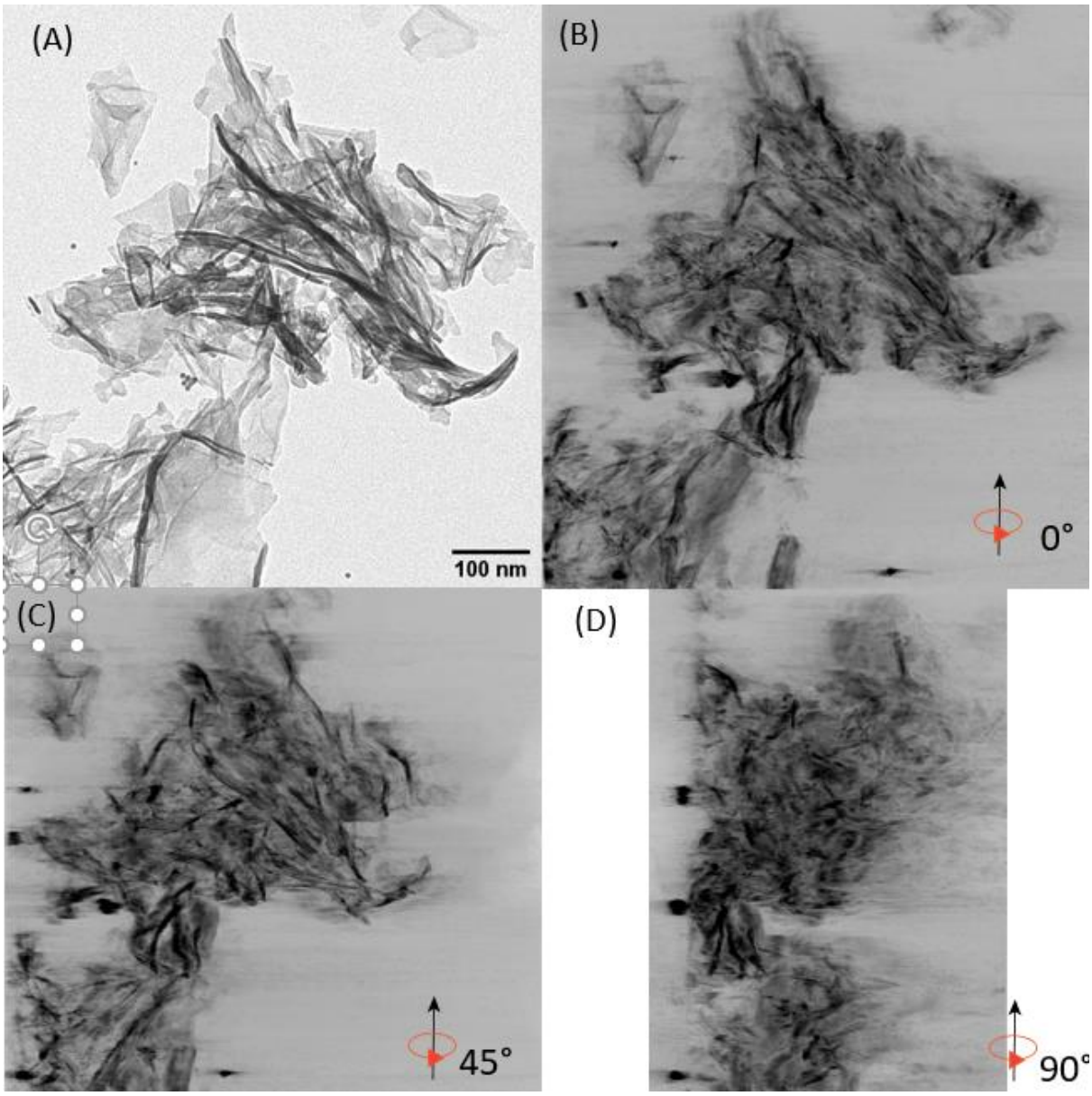

Figure 3.5 2D image and 3D reconstruction of C-S-H 0.6: (A) 2D image, (B) 3D at 0° rotation, (C) 3D at 45° rotation, (D) 3D at 90° rotation. The 3D image is a 2D section through the 3D model.

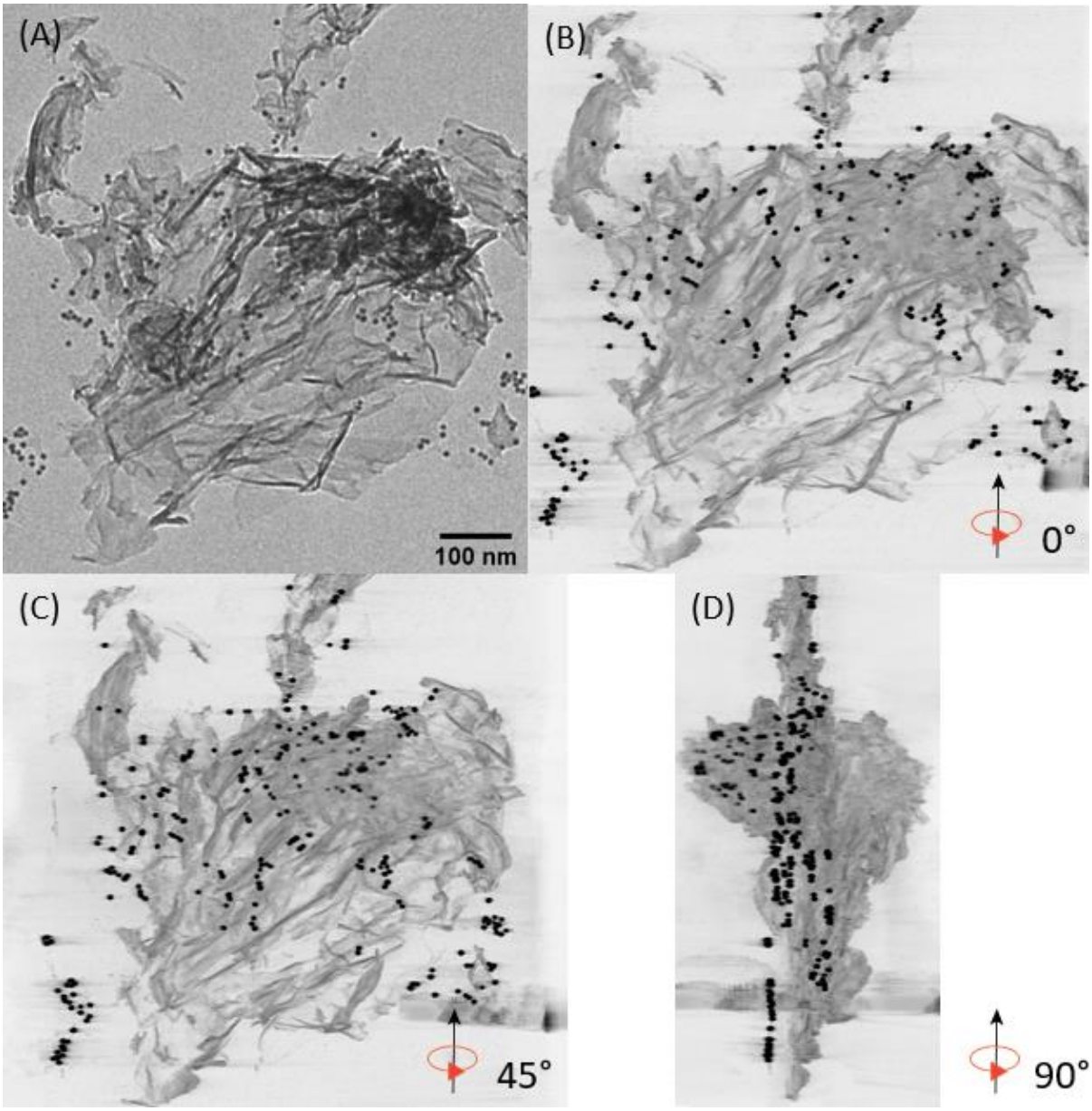

Figure 3.6 2D image and 3D reconstruction of C-S-H 0.8: (A) 2D image, (B) 3D at 0° rotation, (C) 3D at 45° rotation, (D) 3D at 90° rotation. The 3D image is a 2D section through the 3D model.

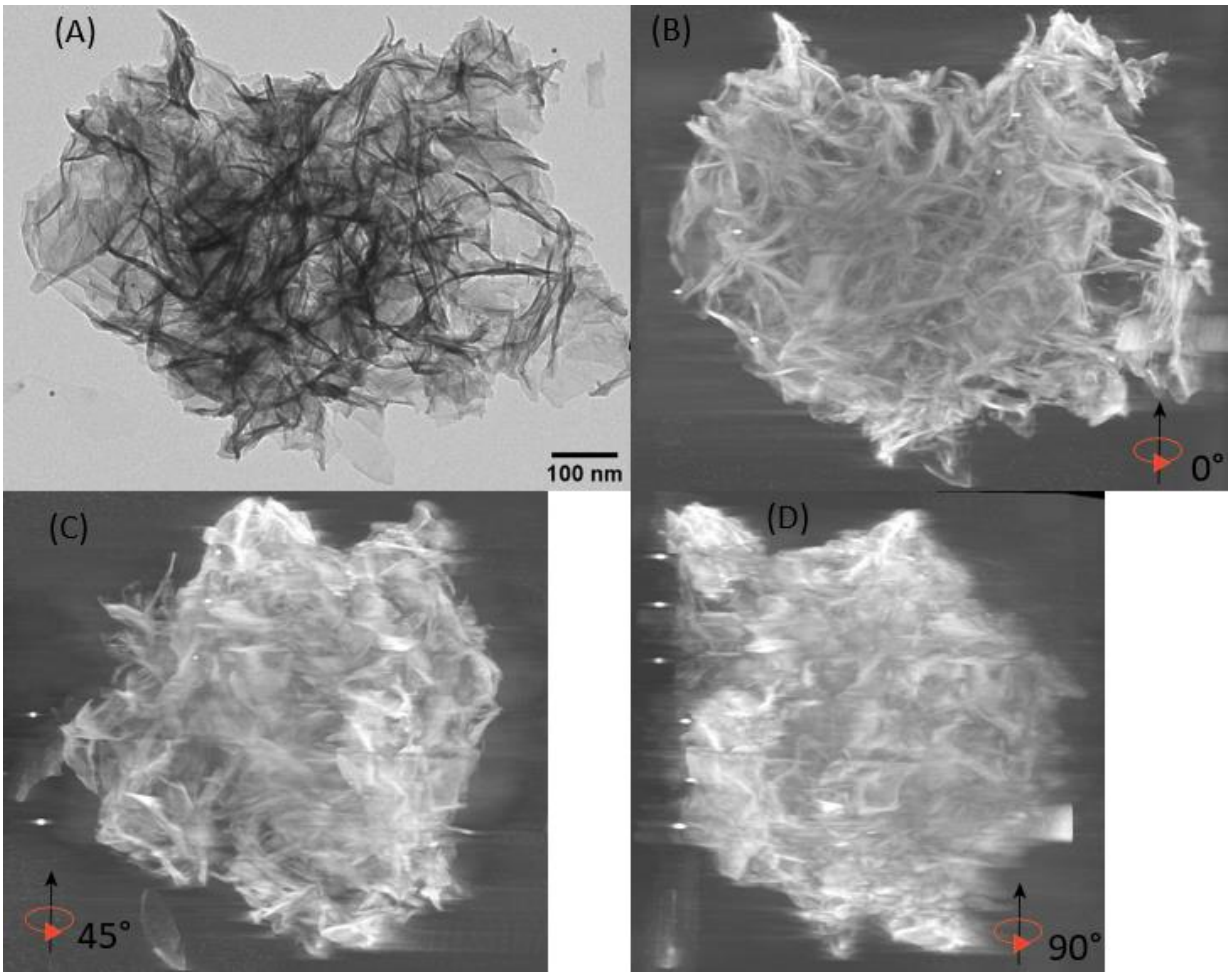

Figure 3.7 2D image and 3D reconstruction of C-S-H 1.0: (A) 2D image, (B) 3D at 0° rotation, (C) 3D at 45° rotation, (D) 3D at 90° rotation. The 3D image is a 2D section through the 3D model.

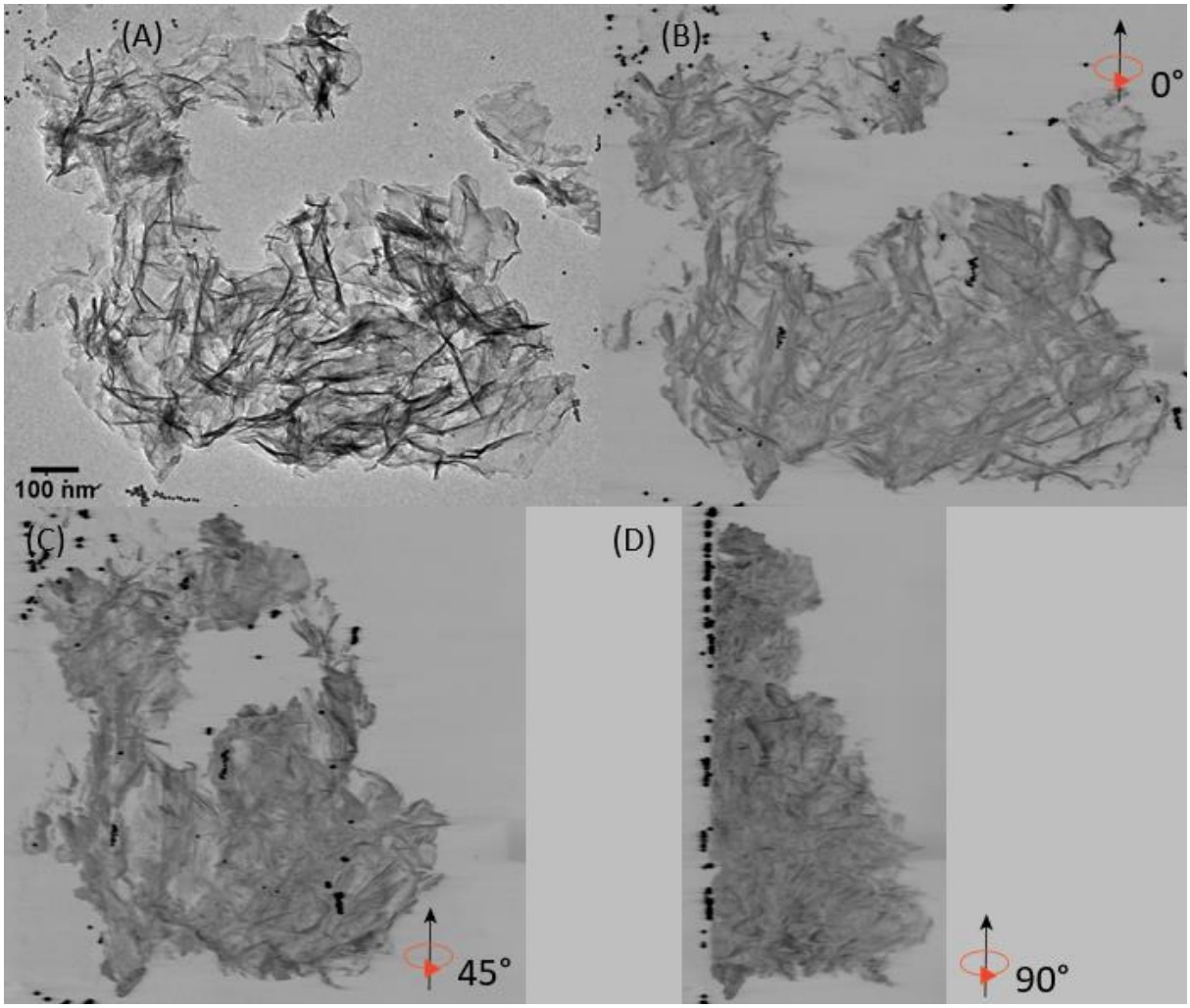

Figure 3.8 2D image and 3D reconstruction of C-S-H 1.2: (A) 2D image, (B) 3D at 0° rotation, (C) 3D at 45° rotation, (D) 3D at 90° rotation. The 3D image is a 2D section through the 3D model.

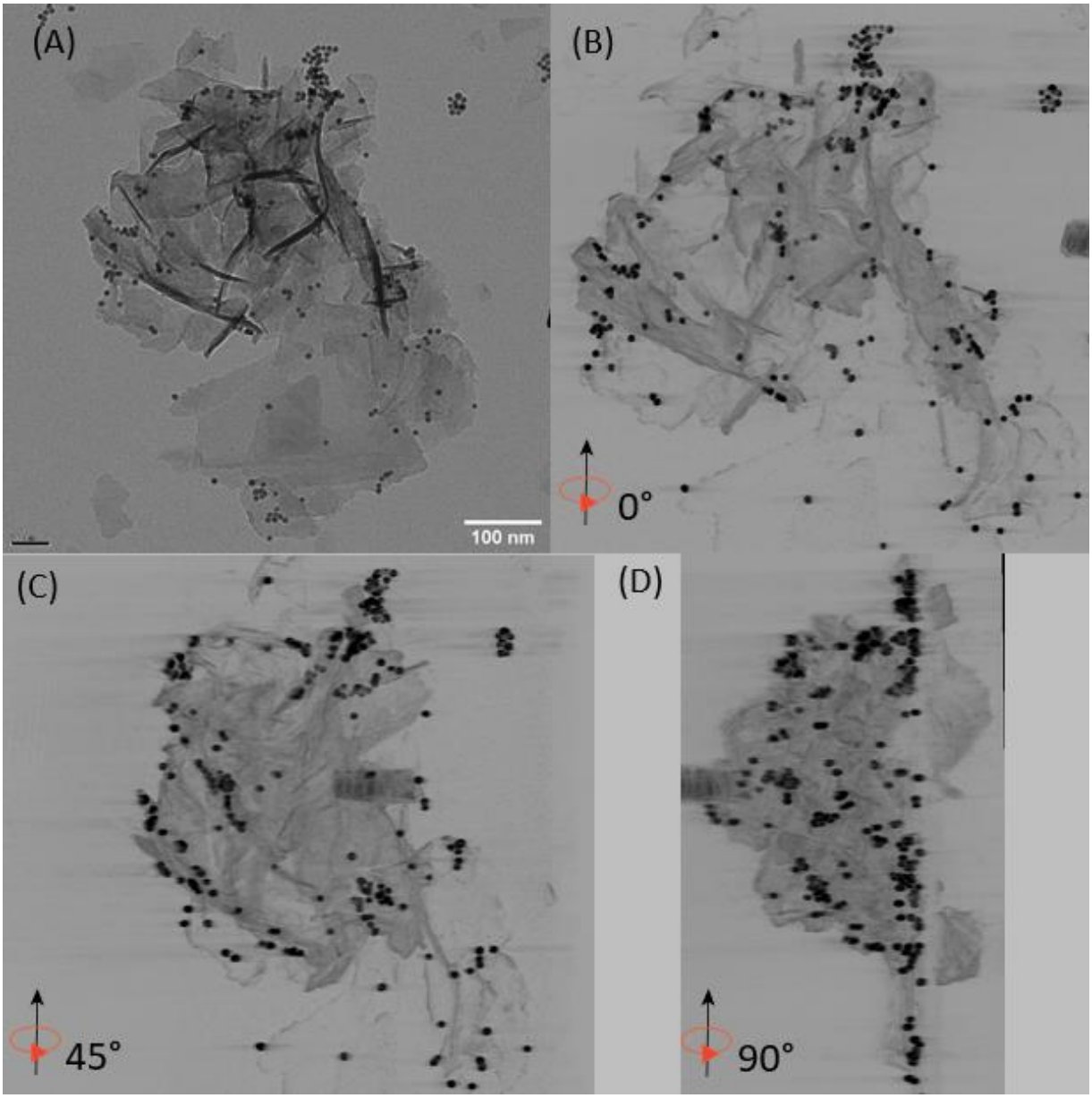

Figure 3.9 2D image and 3D reconstruction of C-S-H 1.4: (A) 2D image, (B) 3D at 0° rotation, (C) 3D at 45° rotation, (D) 3D at 90° rotation. The 3D image is a 2D section through the 3D model.

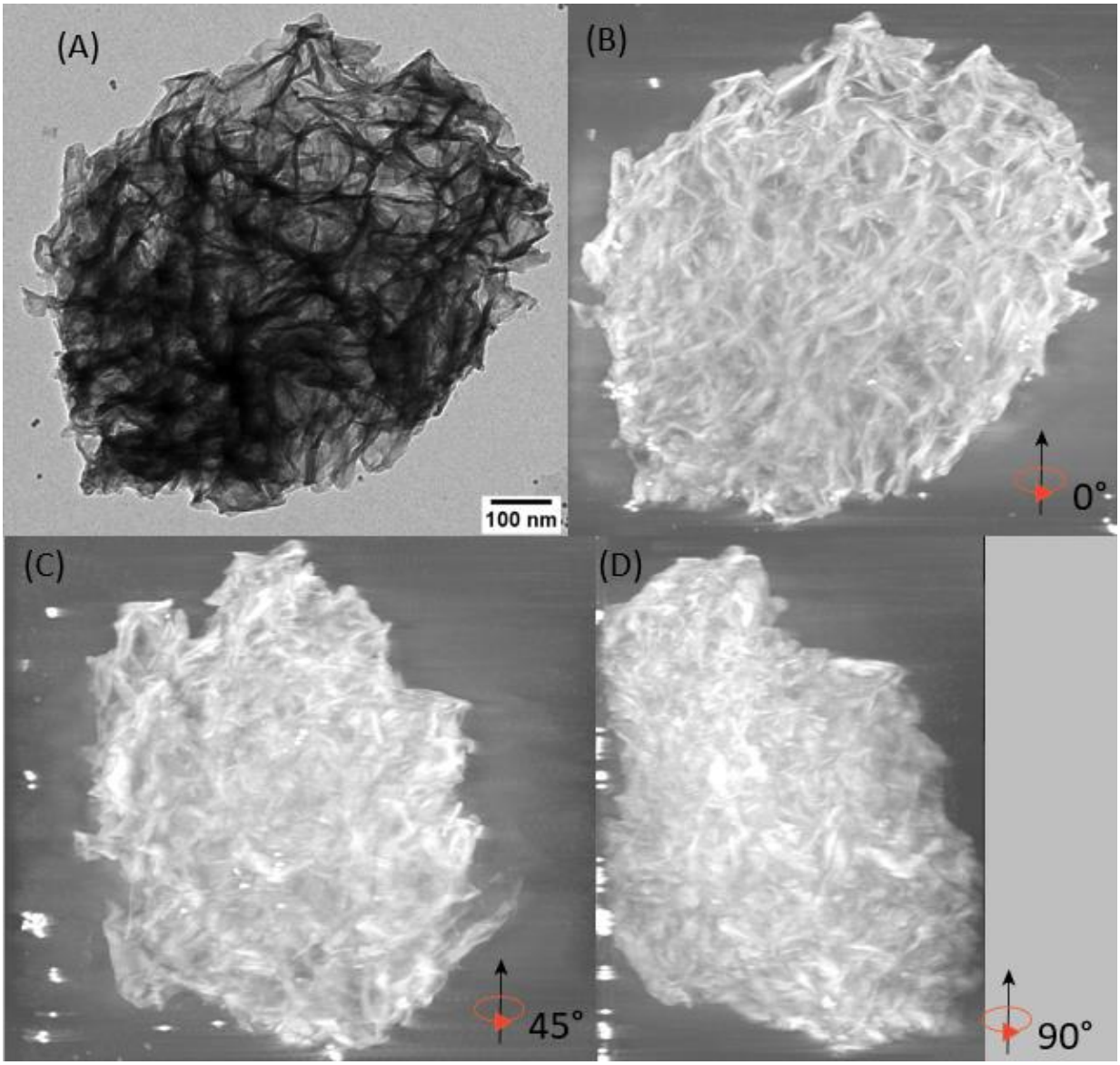

Figure 3.10 2D image and 3D reconstruction of C-S-H 1.6: (A) 2D image, (B) 3D at 0° rotation, (C) 3D at 45° rotation, (D) 3D at 90° rotation. The 3D image is a 2D section through the 3D model.

The 2D images are collected in Brightfield TEM mode. We can see that the C-S-H morphology of all Ca/Si ratios in the system is a combination of foil-like structures and elongated (fiber-like) structures. However, these particles have a complex 3D morphology, and simple 2D TEM projection images are insufficient to describe the morphology.

The morphologies of C-S-H are determined by the structure and chemical composition and/or kinetically of the hydration reaction (Richardson, 2004). The morphologies of both C-S-H are made up of elongated, connected structures with different orientations.

Next, we will take a closer look at the elongated regions of interest (ROIs) to investigate the underlying morphology at higher resolution. Elongated ROIs refer to foil-like structures that are perceived as fibers when observing the original 2D projection images of such structures. Two samples, C-S-H 1.0 and C-S-H 1.6, were selected to determine the real morphology. The visualization of two models were done by software Tomviz (Levin et al., 2018). Five ROIs were selected for each sample (Figure 3.11). The particles sit randomly on a TEM grid. The original projection direction with the grid approximately flat is arbitrary set as 0-degree rotation. Then we rotate 90° around the parent fiber direction. Each ROI is shown in 0° rotation and 90° rotation (Figure 3.12 for C-S-H 1.0 and Figure 3.13 for C-S-H 1.6). The actual geometry and aspect ratios of these ROIs are shown in Table 3.2. The thickness (a) of each ROI can be determined from the orientation looking along with the plate. The width (b) and length (c) can be determined from the direction normal to the plate. The thickness (a), width (b), and length (c) are represented by red lines in both Figure 3.12 and Figure 3.13. Both 2D aspect ratios have high values (more than 5), indicating that all of them are elongated platelets, not fibers.

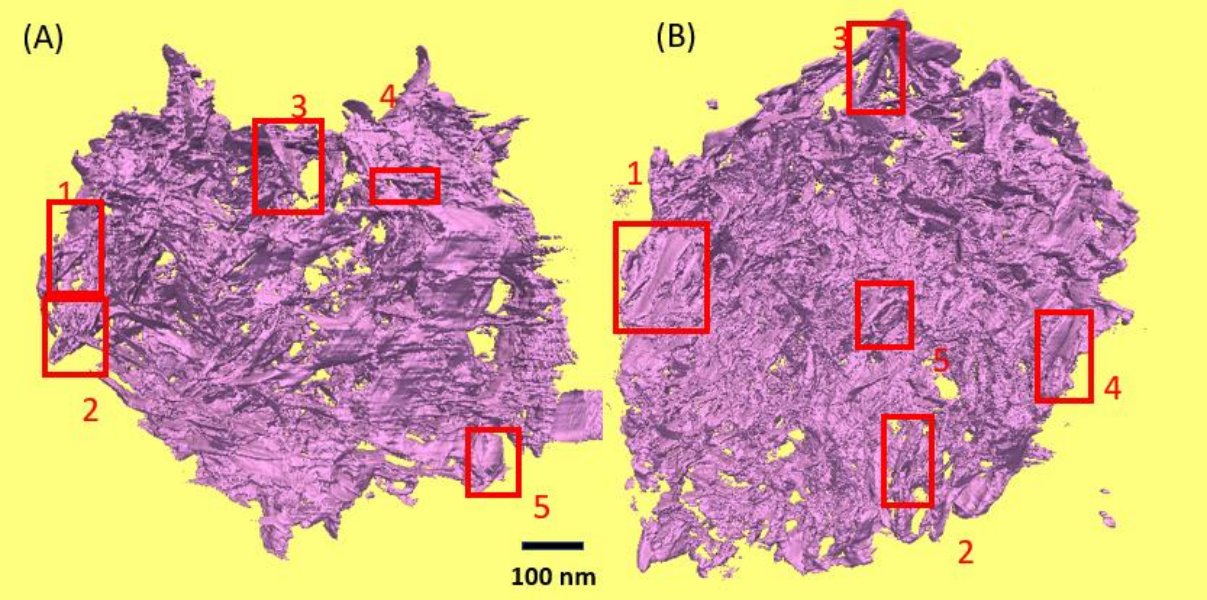

Figure 3.11 The 3D models C-S-H 1.0 (A) and 1.6 (B) visualized by software Tomviz. Five selected elongated ROIs are indicated by red rectangles.

Table 3.2 Actual geometry and aspect ratio of selected ROIs of both samples.

Sample					
C-S-H 1.0	Thickness (a) (nm)	Width (b) (nm)	Length (c) (nm)	2D Aspect ratio (b/a)	2D Aspect ratio (c/a)
Particle 1	7.15	73.00	149.00	10	21
Particle 2	7.76	84.89	171.52	11	22
Particle 3	6.06	76.89	106.24	13	18
Particle 4	6.32	68.11	78.97	11	12
Particle 5	5.46	62.10	99.37	11	18
C-S-H 1.6	Thickness (a) (nm)	Width (b) (nm)	Length (c) (nm)	2D Aspect ratio (b/a)	2D Aspect ratio (c/a)
Particle 1	8.13	58.85	141.06	7	17
Particle 2	4.27	56.05	83.16	13	19
Particle 3	10.19	49.82	156.05	5	15
Particle 4	4.94	42.50	94.80	9	19
Particle 5	3.83	37.63	76.40	10	20

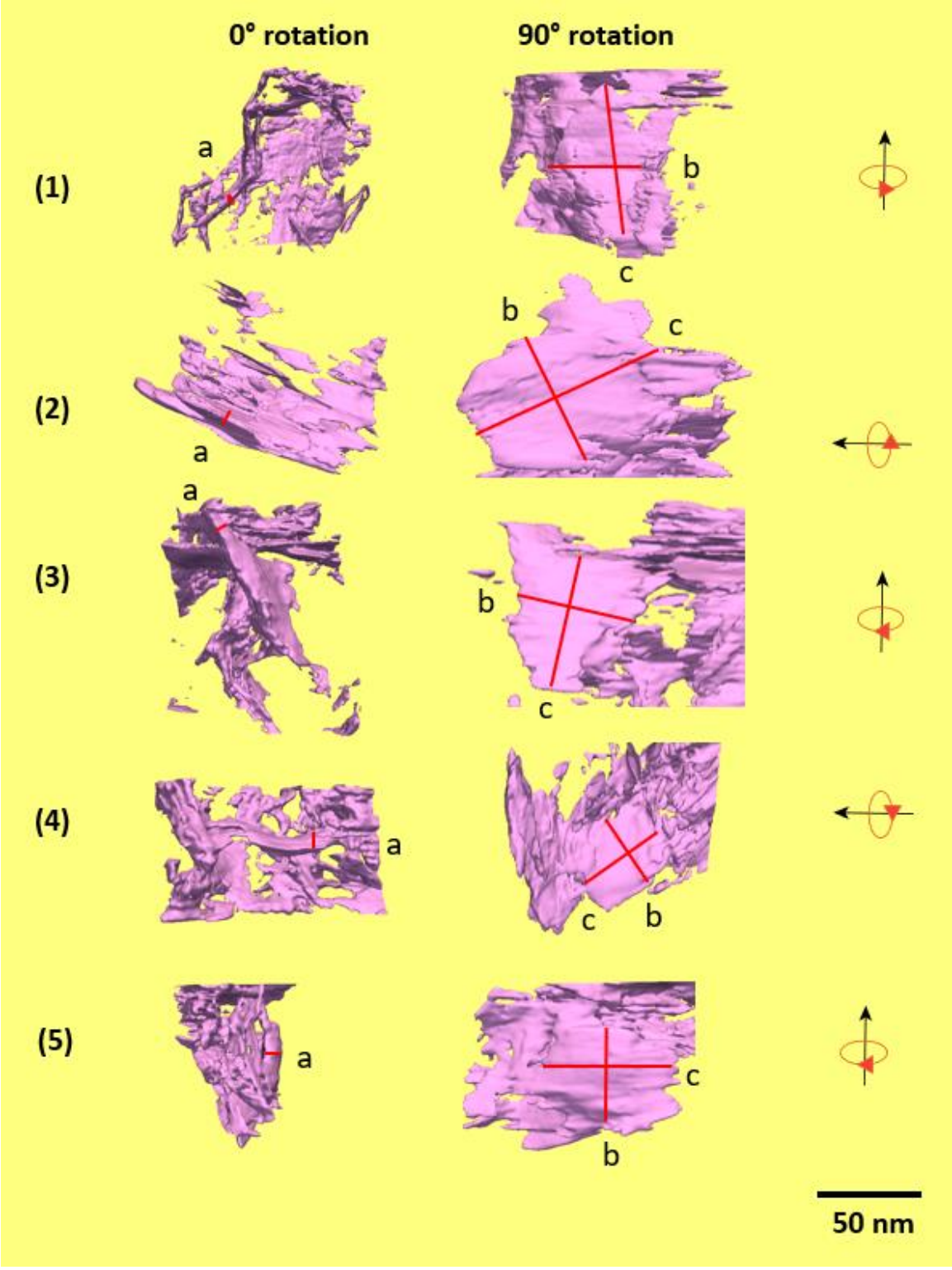

Figure 3.12 Morphologies of five selected elongated ROIs of C-S-H 1.0

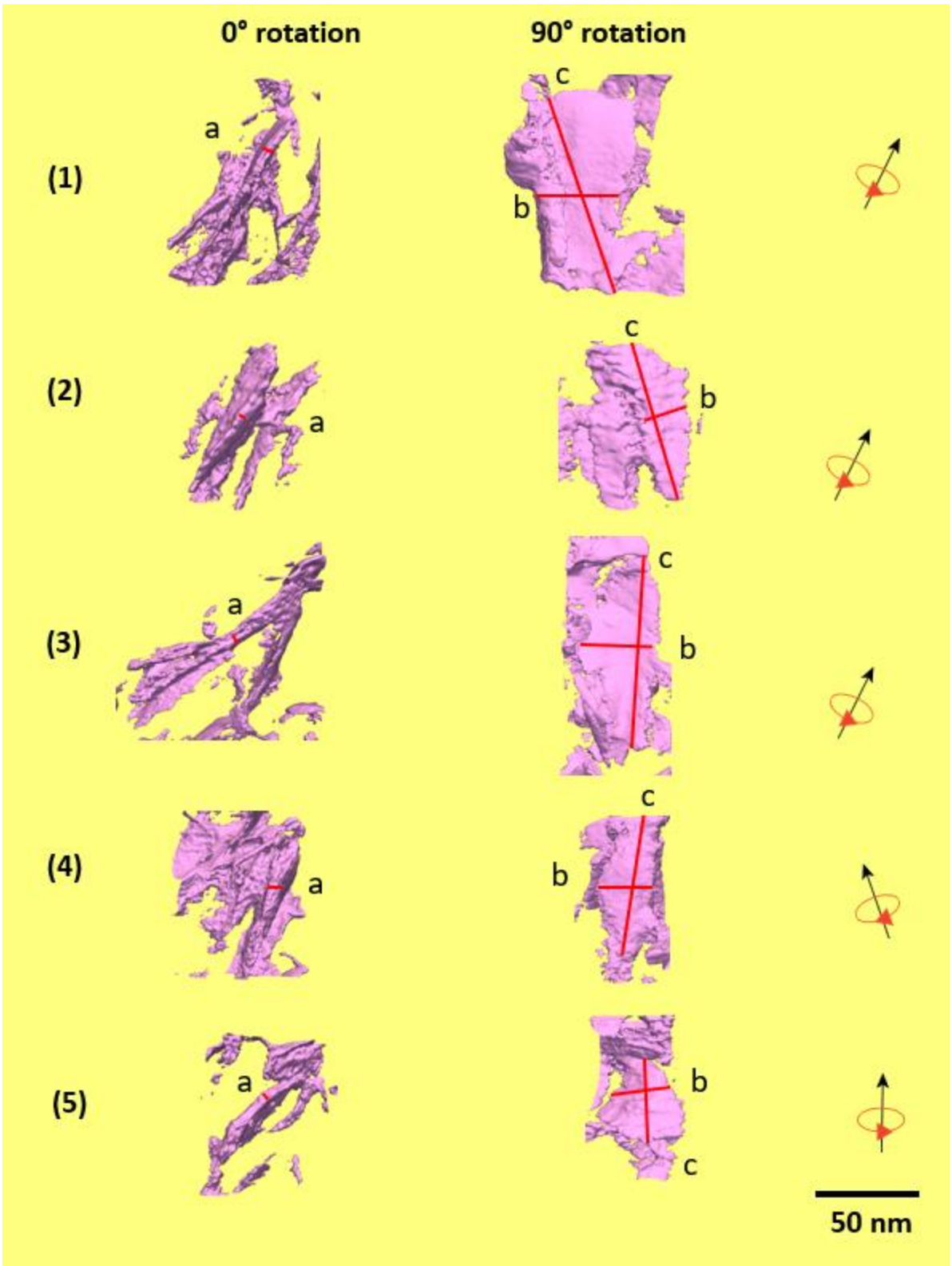

Figure 3.13 Morphologies of five selected elongated ROIs of C-S-H 1.6

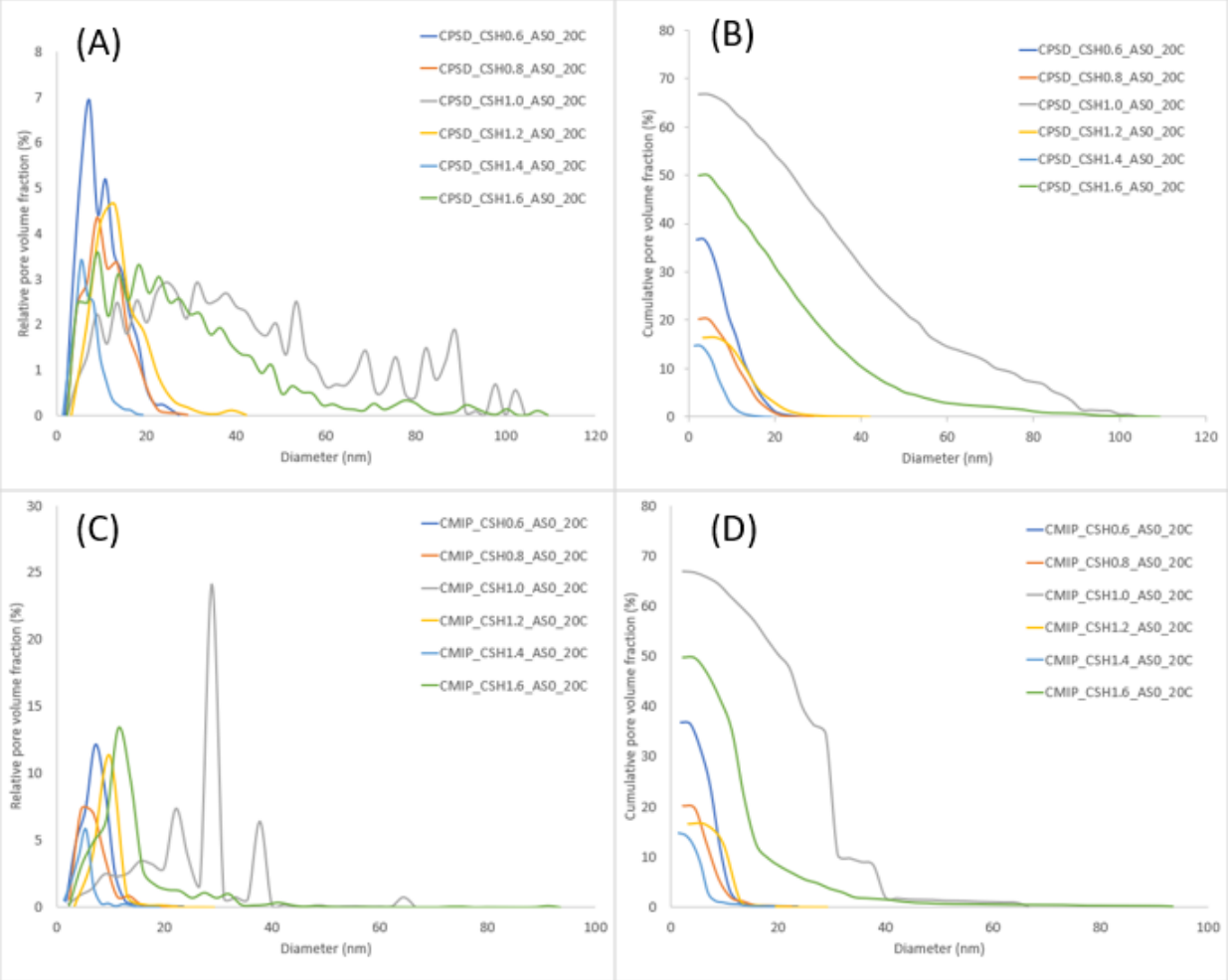

Figure 3.14 Pore size distributions of C-S-H at Ca/Si ratio 0.6, 0.8, 1.0, 1.2, 1.4 and 1.6 at curing temperature 20° C (A) Continuous pore size distribution (CPSD), (B) Cumulative continuous pore size distribution (CCPSD), (C) Continuous pore size distribution with MIP simulation (CMIP), (D) Cumulative continuous pore size distribution with MIP simulation (CCMIP)

Continuous pore size distribution (CPSD) and Continuous pore size distribution with MIP simulation (CMIP) was analyzed in this research (Figure 3.14). The voxel sizes and porosities are shown in Table 3.3. Both CPSD and CMIP reveal that most of the pore sizes of all samples are below 40 nm. However, C-S-H 1.0 and C-S-H 1.6 seem to have larger pore sizes than the rest. For CPSD, both C-S-H 1.0 and C-S-H 1.6 have a larger pore size up to 100 nm (Figure 3.14A). For CMIP, C-S-H 1.0 and C-S-H 1.6 have a dominant peak at 28.8 nm.

Table 3.3 Voxel size, porosity, pore size range for C-S-H with various ratios

Sample	Voxel size (nm)	Porosity (%)	CPSD pore size range (nm)	CMIP pore size range (nm)
C-S-H0.6_AS0_20C	0.91	36.7	2 - 27	2 - 23
C-S-H0.8_AS0_20C	1.12	20.2	2 - 29	2 - 22
C-S-H1.0_AS0_20C	1.11	66.8	2 - 104	2 - 66
C-S-H1.2_AS0_20C	1.62	16.5	3 - 42	3 - 29
C-S-H1.4_AS0_20C	0.69	14.7	1 - 19	1 - 19
C-S-H1.6_AS0_20C	1.14	49.8	2 - 109	2 - 93

3.5.3 Effect of curing temperature on the structure of C-S-H and C-A-S-H

The 2D images and 3D reconstructed models are shown in Figure 3.15 to Figure 3.20.

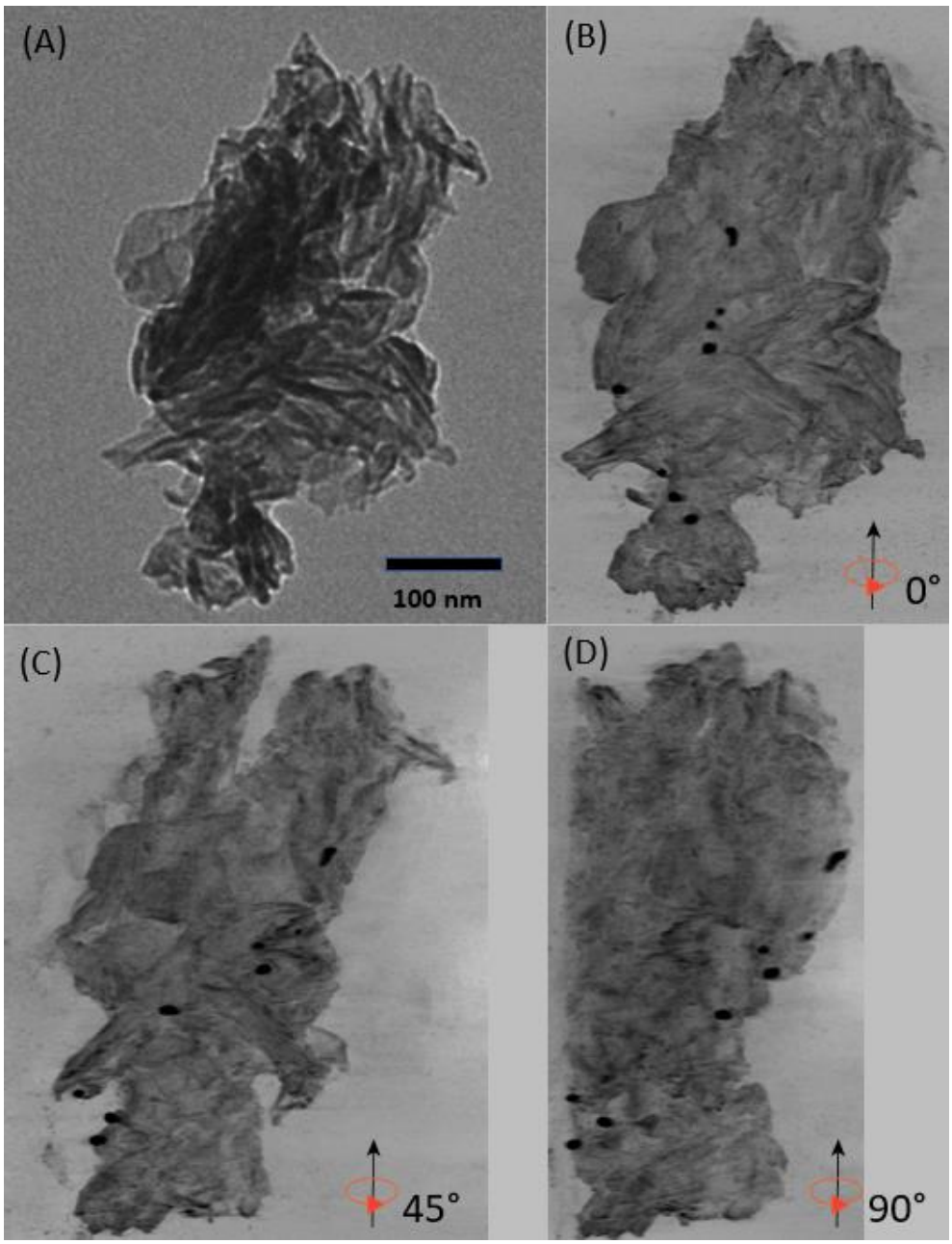

Figure 3.15 2D image and 3D reconstruction of C-S-H 1.0 at curing temperature 7° C : (A) 2D image, (B) 3D at 0° rotation, (C) 3D at 45° rotation, (D) 3D at 90° rotation. The 3D image is a 2D section through the 3D model.

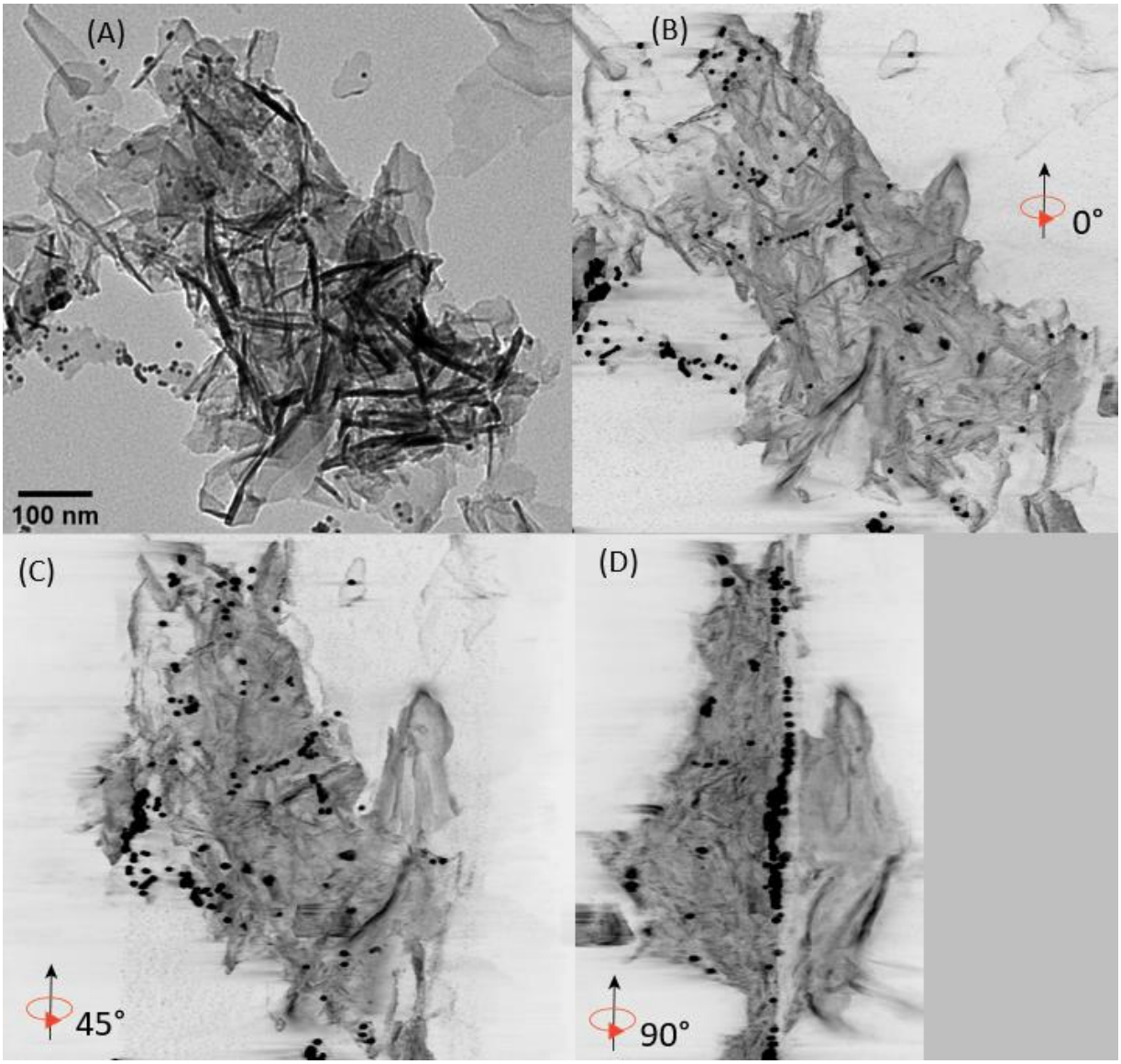

Figure 3.16 2D image and 3D reconstruction of C-S-H 1.0 at curing temperature 50° C : (A) 2D image, (B) 3D at 0° rotation, (C) 3D at 45° rotation, (D) 3D at 90° rotation. The 3D image is a 2D section through the 3D model.

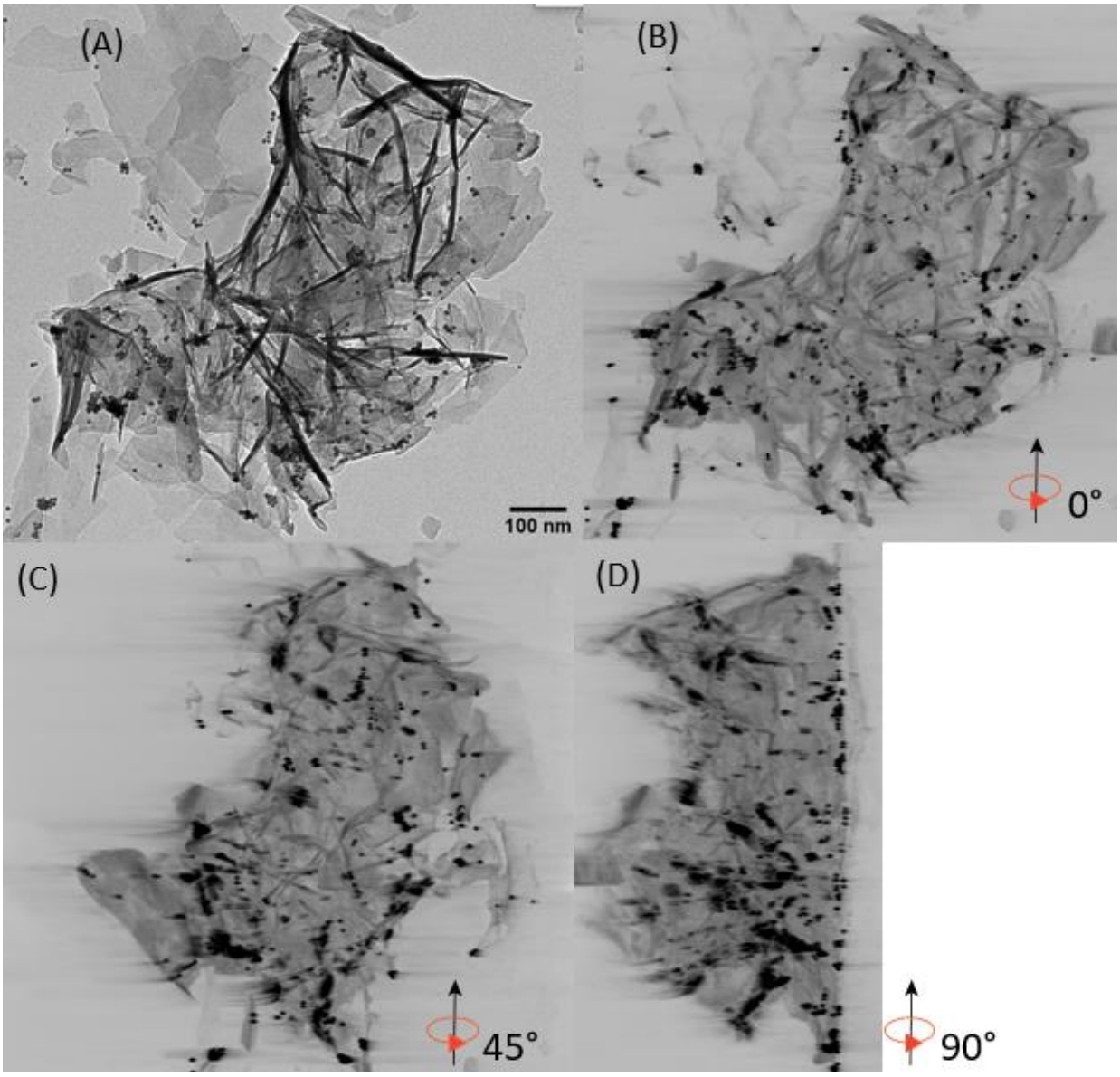

Figure 3.17 2D image and 3D reconstruction of C-S-H 1.0 at curing temperature 80° C : (A) 2D image, (B) 3D at 0° rotation, (C) 3D at 45° rotation, (D) 3D at 90° rotation. The 3D image is a 2D section through the 3D model.

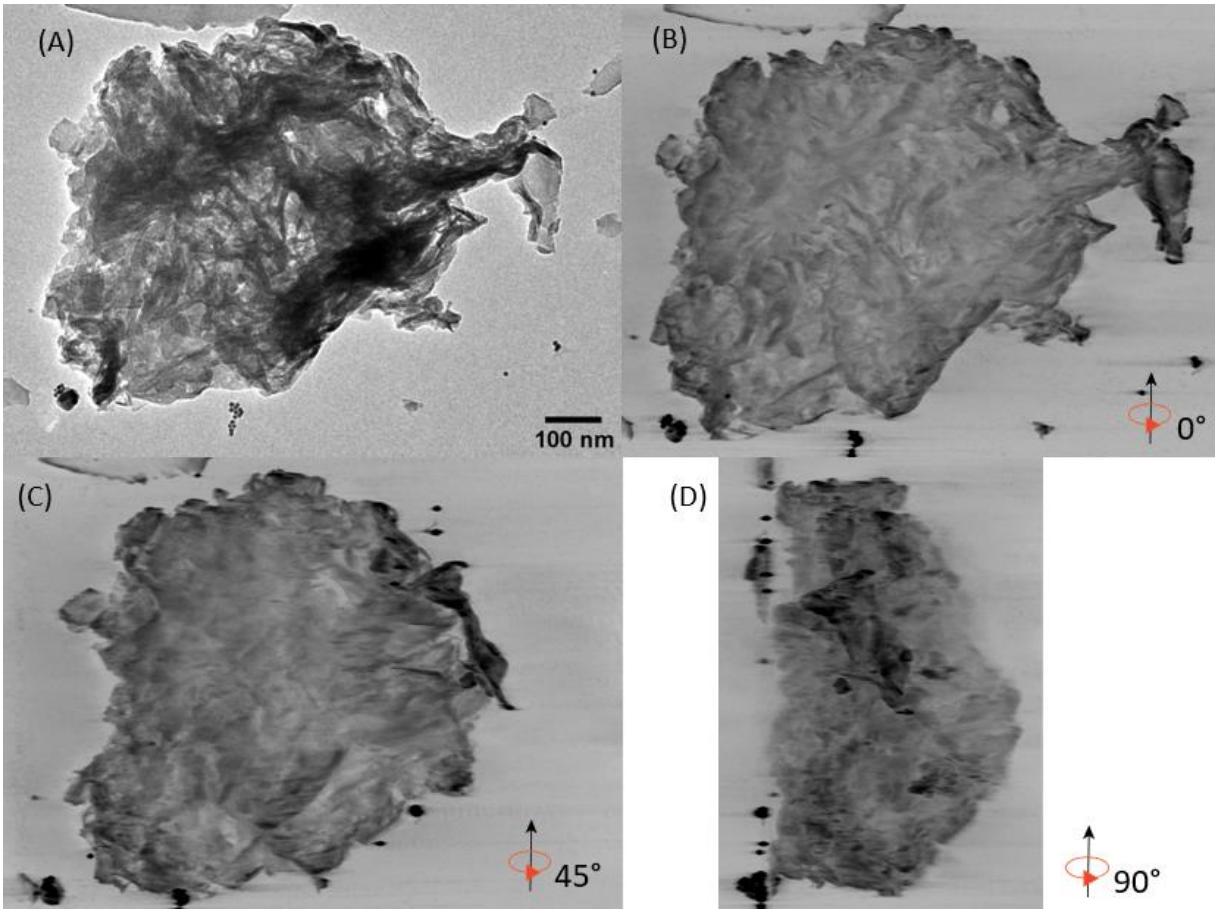

Figure 3.18 2D image and 3D reconstruction of C-A-S-H 1.0 with Al/Si 0.05 at curing temperature 7° C : (A) 2D image, (B) 3D at 0° rotation, (C) 3D at 45° rotation, (D) 3D at 90° rotation. The 3D image is a 2D section through the 3D model.

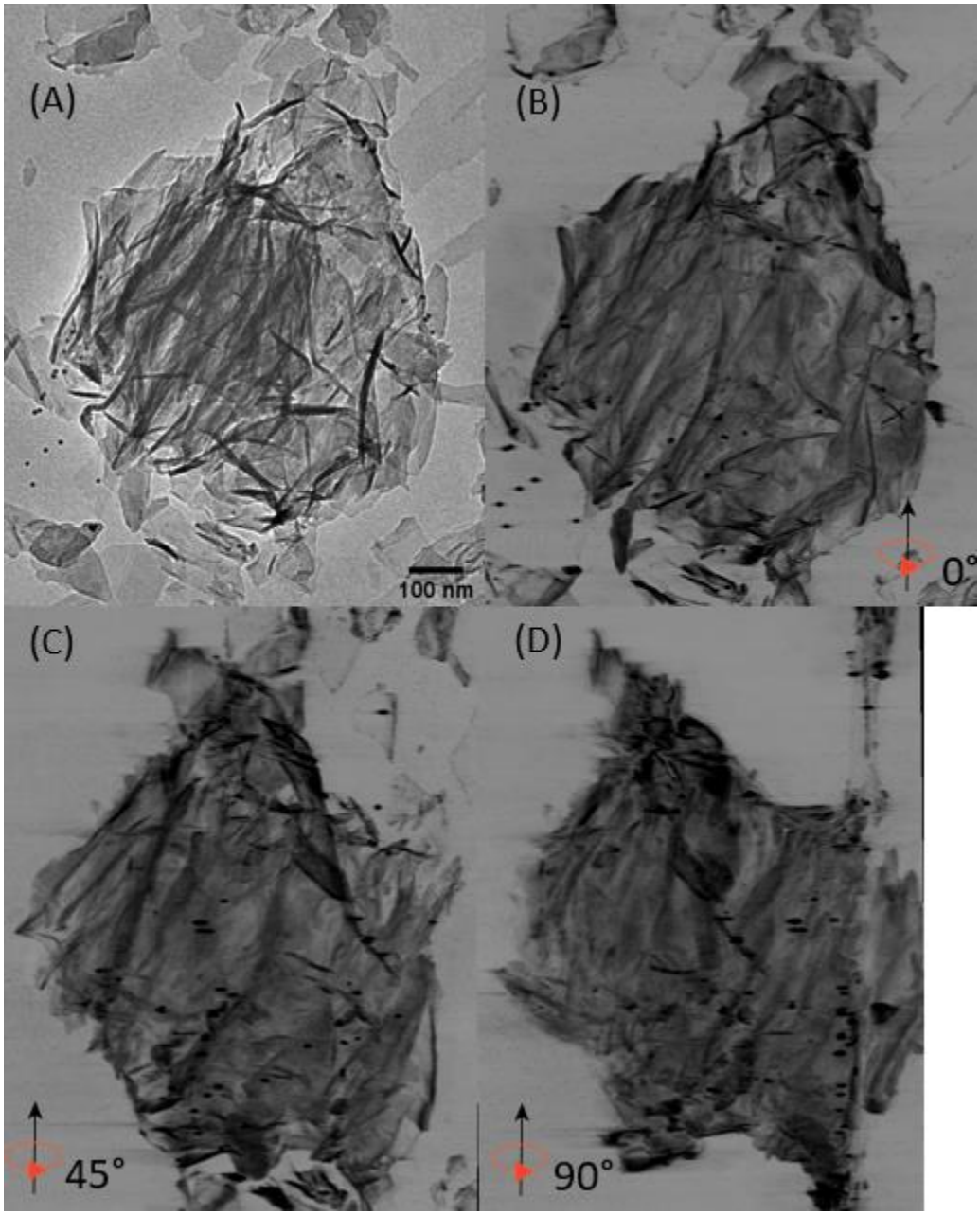

Figure 3.19 2D image and 3D reconstruction of C-A-S-H 1.0 with Al/Si 0.05 at curing temperature 50° C : (A) 2D image, (B) 3D at 0° rotation, (C) 3D at 45° rotation, (D) 3D at 90° rotation. The 3D image is a 2D section through the 3D model.

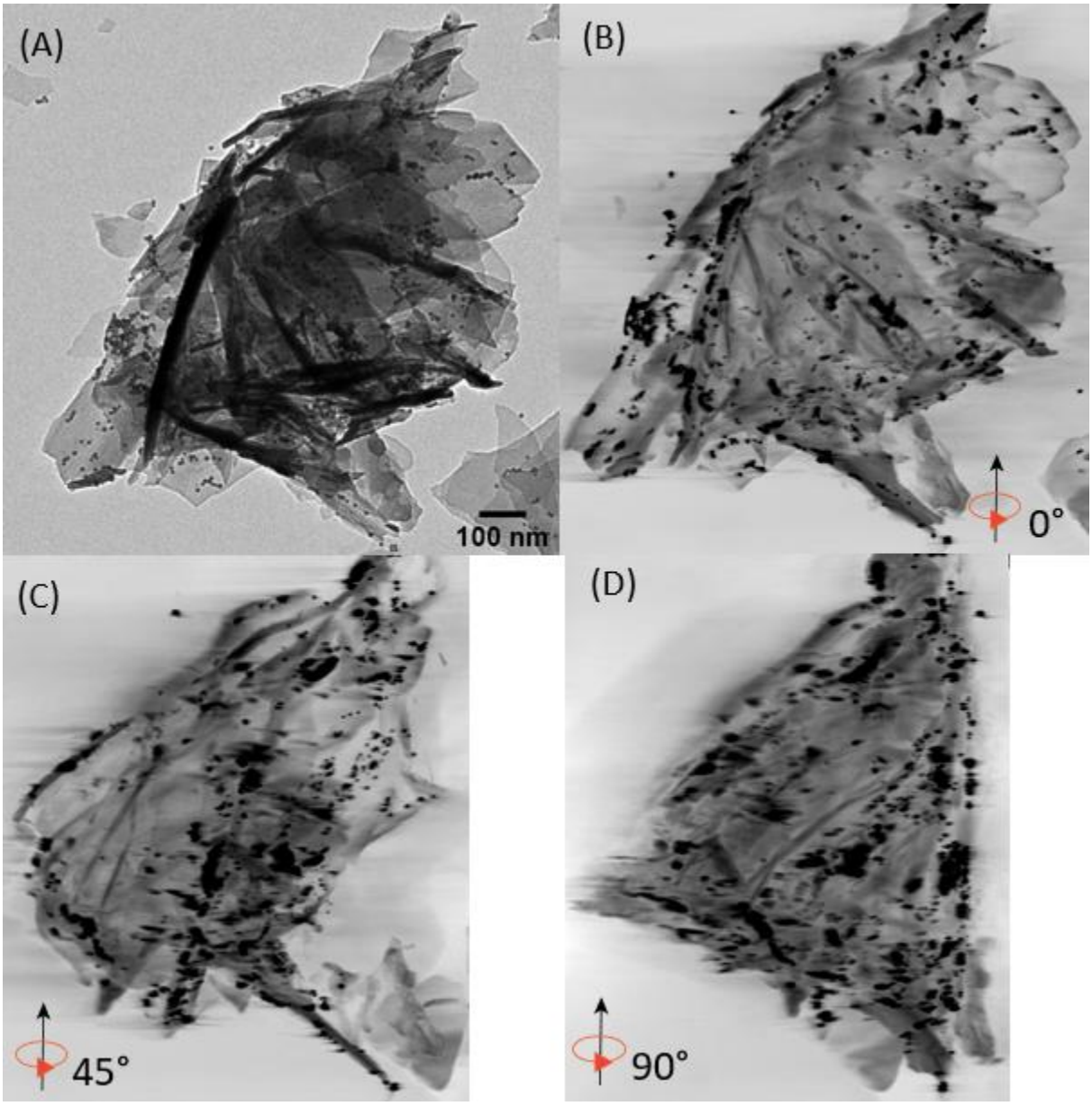

Figure 3.20 2D image and 3D reconstruction of C-A-S-H 1.0 with Al/Si 0.05 at curing temperature 80° C : (A) 2D image, (B) 3D at 0° rotation, (C) 3D at 45° rotation, (D) 3D at 90° rotation. The 3D image is a 2D section through the 3D model.

The morphology of all C-S-H and C-A-S-H at various curing temperatures are only foil-like structures. The elongated morphology is still platelets, not fibers.

Continuous pore size distribution (CPSD) and Continuous pore size distribution with MIP simulation (CMIP) were also analyzed in this research (Figure 3.21). The voxel sizes and porosities are shown in Table 3.4. Both CPSD and CMIP, all C-S-H samples have a pore size range below 40 nm, while C-A-S-H samples have a higher pore size range around 31 and 69 nm. For CMIP, C-A-S-H1.0_AS0.05_50C has a dominant peak at 19.4 nm (Figure 3.21C).

For the porosity, results strongly indicated that the higher the curing temperature, the lower porosity occurred.

Table 3.4 Voxel size, porosity, the pore size range for C-S-H with various ratios

Sample	Voxel size (nm)	Porosity (%)	CPSD pore size range (nm)	CMIP pore size range (nm)
C-S-H1.0_AS0_7C	0.91	47.7	2 - 38	2 - 23
C-S-H1.0_AS0_50C	1.14	24.8	2 - 27	2 - 25
C-S-H1.0_AS0_80C	1.14	21.1	2 - 41	2 - 25
C-A-S-H1.0_AS0.05_7C	1.62	51.7	3 - 68	3 - 55
C-A-S-H1.0_AS0.05_50C	1.14	24.6	2 - 31	2 - 23
C-A-S-H1.0_AS0.05_80C	1.92	20.2	4 - 69	4 - 50

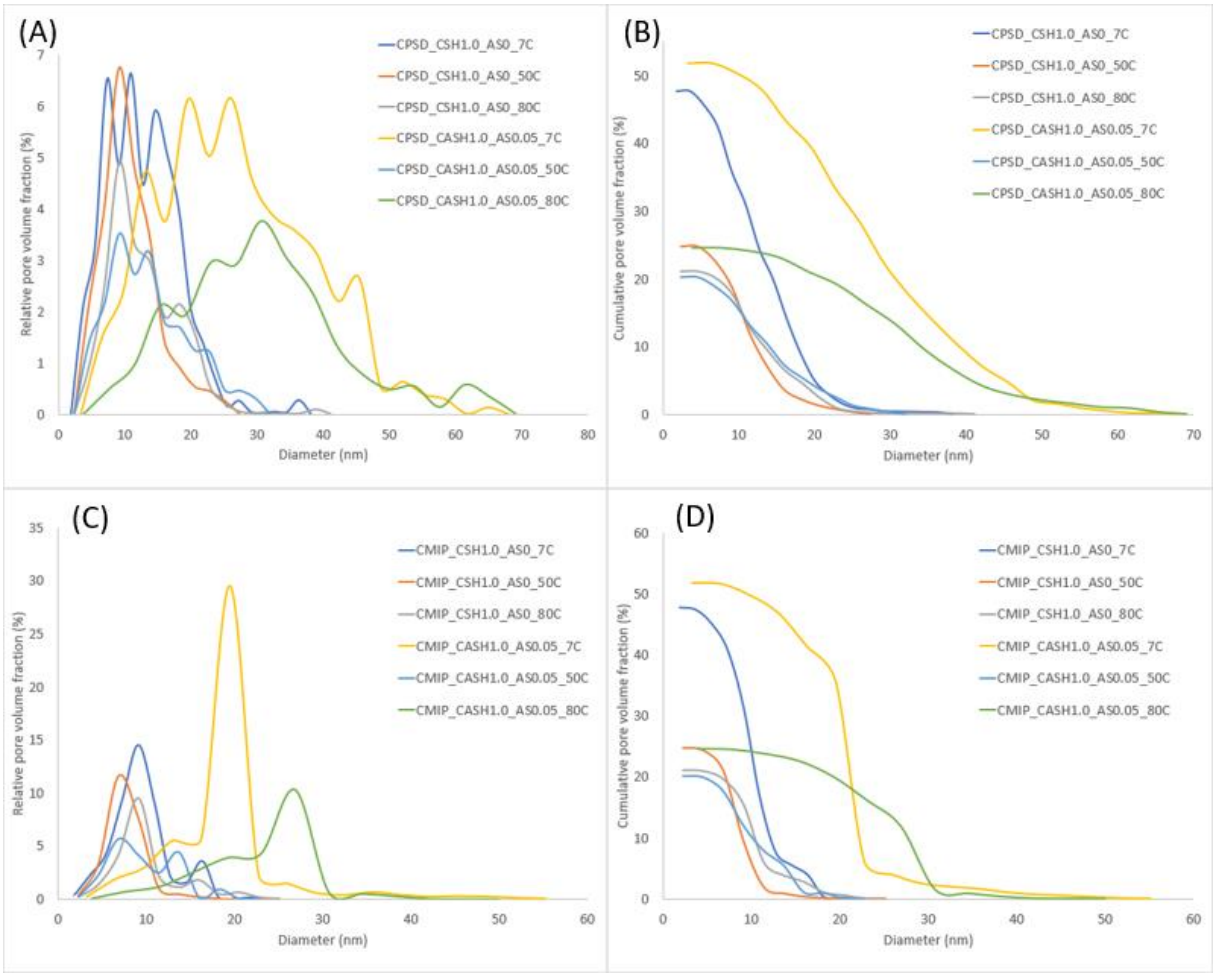

Figure 3.21 Pore size distributions of C-S-H 1.0 at curing temperature 7, 50, 80° C and C-A-S-H 1.0, A/S 0.05: at curing temperature 7, 50, 80° C (A) Continuous pore size distribution (CPSD), (B) Cumulative continuous pore size distribution (CCPSD), (C) Continuous pore size distribution with MIP simulation (CMIP), (D) Cumulative continuous pore size distribution with MIP simulation (CCMIP)

3.6 Conclusions

This chapter uses TEM tomography with simultaneous iterative reconstruction technique (SIRT) to generate the 3D reconstruction of C-S-H and C-A-S-H microstructures which can be found in Portland cement paste or C_3S paste. The projection images were aligned using the 10 nm gold nanoparticles as references. The highest beam dose that can achieve this with a little beam damage is 5000 $e^-/(nm^2\ s)$ for all samples.

The 3D reconstructions and selected ROI analysis confirm that there are only foil-like structures for all C-S-H and C-A-S-H with various Ca/Si, Al/Si, and curing temperatures.

Both CPSD and CMIP reveal that most of the pore sizes of all samples are below 40 nm. However, C-S-H1.0_AS0_20C, C-S-H1.6_AS0_20C, C-A-S-H1.0_AS0.05_7C, and C-A-S-H1.0_AS0.05_80C seem to have larger pore size than the rest. The porosity is affected by the curing temperature. The higher curing temperature will make the lower porosity in the structure of both C-S-H and C-A-S-H.

There are many advanced reconstruction methods like The algebraic reconstruction technique (ART) (Herman et al., 1973), the equal slope tomography (EST) (Jiang et al., 2010; Lee et al., 2008) that can solve the missing wedge and other artifact problem better than the simultaneous iterative reconstruction technique (SIRT). However, these methods required longer analysis time, complex methodology, and high-performance computers.

TEM tomography combined with the Beat plugin in ImageJ shows the capability to determine the 3D nanostructure and pore networks of C-S-H and C-A-S-H.

4. Scanning Transmission Electron Microscope (STEM) tomography

4.1 Introduction

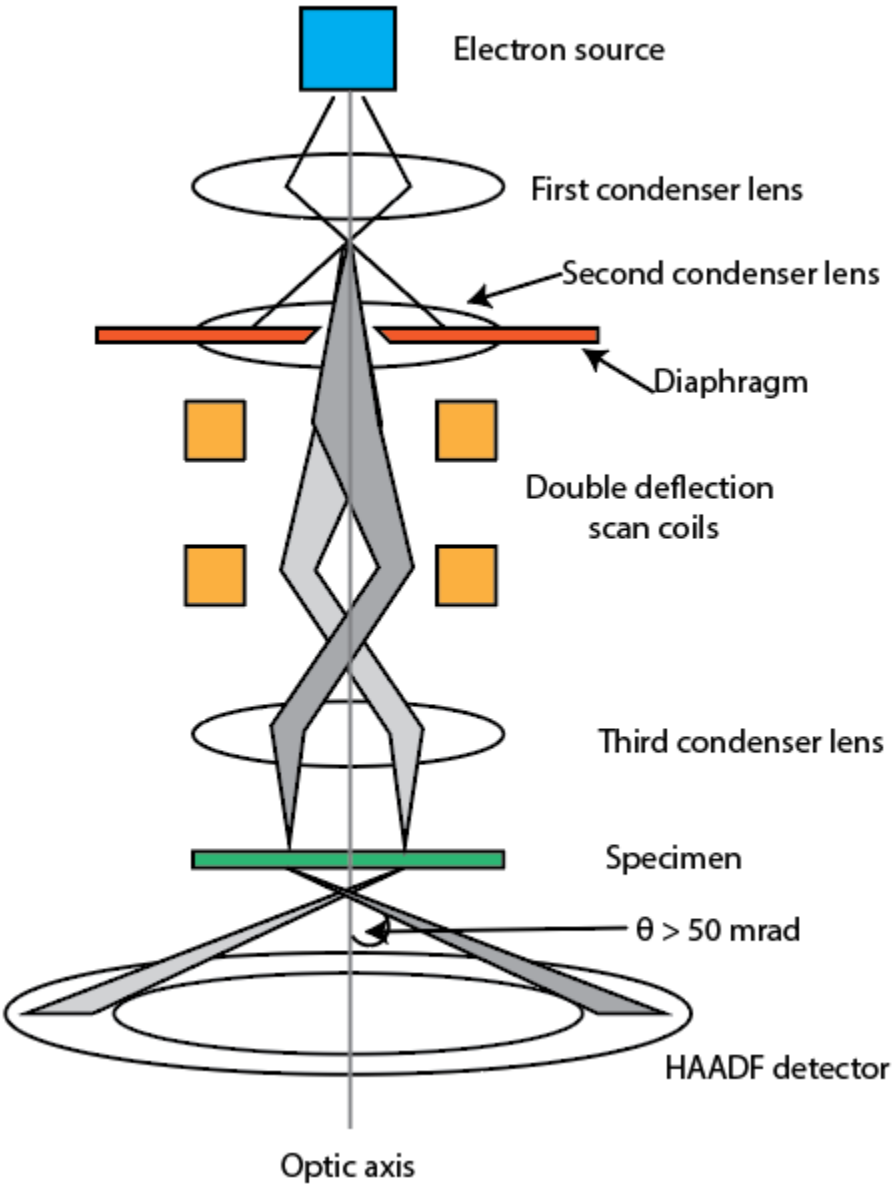

Figure 4.1 Schematic of the instrument configuration for STEM (Williams & Carter, 2009)

Scanning transmission electron microscopy (STEM) (Williams & Carter, 2009) combines the principles of transmission electron microscopy (TEM) and scanning electron microscopy (SEM). STEM requires very thin samples like TEM and focuses at electrons transmitted by the sample. A schematic of STEM is shown in Figure 4.1.

One of the TEM problems is the interference of the diffracted beam when it interacts with the crystalline solids at the atomic scale. A minor change in crystal structure or orientation can produce radically different intensities and patterns in the recorded image (Frank, 2008). This limits the application of electron tomography using TEM (Koster et al., 2000). This issue can be solved by using STEM. The pre-specimen optics create a convergent electron probe at the sample surface focused on a small diameter. The convergent beam electron diffraction (CBED) pattern is produced after the specimen, and a single-channel detector is used to combine the electron flux within a range of scattering angles. STEM provides a wide range of operating modes from nanometer to sub-angstrom resolution, depending on the electron source, accelerating voltage, convergence angle, and lens settings. The most common detector in STEM is a high-angle annular dark-field (HAADF) detector designed to collect only highly scattered electrons (more than 50 mrad) (Pennycook, 1989). HAADF-STEM can differentiate materials with different atomic numbers (Z -contrast imaging), but it has a high sensitivity for high-Z elements (Ercius et al., 2006). However, this characteristic is not an advantage to our materials because cements mainly consist of Calcium and Silicon, which are low-Z elements.

A significant advance in STEM with direct application to electron tomography has been the wide-scale introduction of aberration correctors. The focusing power of the electron lenses used in STEM is limited by spherical aberration, where the minimum probe size is defined as:

$$d_{min} = 0.43\lambda^{3/4}C_3^{1/4} \qquad \text{Equation 4.1}$$

Where C_3 is the third-order spherical aberration (also called C_s), and λ is the wavelength of the incident electrons (Scherzer, 1936). Spherical aberration causes electrons from the center of the lens to be focused to a different point

along the optical axis and increases the size of the focused electron beam at the sample. STEM is typically limited to electron probes with >1 Å resolution, making many important features at the atomic scale unresolvable. The round electron lenses always create positive spherical aberration coefficients, but it was shown that other optical with non-round symmetry could be combined to generate negative spherical aberration (Scherzer, 1947). Ideally, the C_3 value of round objective lenses can be compensated by introducing electron-optical elements to the column, but this has been proved extremely difficult for many years (Uhlemann & Haider, 1998).

Further developments in lens power supply, electron-optical theory, and other concerted efforts in the field have recently led to the realization of aberration correction through the use of multipole elements capable of compensating for the aberrations of an optical system (Krivanek et al., 2001). With this technology, almost all aspects of electron microscopy instrumentation have been improved. The resolution is reduced to 0.5–1 Å, the contrast is greatly improved, and the beam current is increased. These improvements now allow microscopists to measure atomic distances for most crystalline materials, even individual atoms, and make atomic-resolution spectroscopic measurements (Huang et al., 2012; Krivanek et al., 2013).

4.2 Experimental Methods

4.2.1 Materials

C-S-H 1.0 at curing temperature 20° C was used in this experiment. For sample details, see section 3.4.1. The angle range is modified to -70° to +69.5° with a 1.5-degree angle increment.

4.2.2 Electron tomography

The sample was suspended in ethanol and deposited on a 200 mesh ultra-thin copper hexagonal grid with carbon film support (CF200H-Cu-UL, Electron Microscopy Sciences). 10 nm gold fiducial markers (Aldrich) were deposited to aid in tilt series alignment. Data acquisition was acquired on a FEI TitanX 60-300

microscope (Figure 4.2), operating at 300 kV. Images are acquired with a Gatan HAADF detector for STEM. The reconstruction method and model analysis are similar to those described in sections 3.4.2 and 3.4.3.

Figure 4.2 TEM Titan X at The National Center for Electron Microscopy (NCEM), LBNL

4.2.3 Pore connectivity

The number of connected structures in a network can be determined by calculating the Euler characteristic. The Euler characteristic of a 3D structure is the number of particles plus the number of enclosed cavities minus the connectivity (Odgaard & Gundersen, 1993). The connectivity density can be calculated by dividing the connectivity estimate by the volume of the specimen. The algorithm in BoneJ's Connectivity uses voxel to calculate the Euler characteristic of the volume and adjusts this to give the contribution of the volume to the connectivity of the structure it was cut from. The analysis can be done in BoneJ (Doube et al., 2010),

which is a plugin in ImageJ. The connectivity density can be calculated from the equation below.

$$\text{C.D.} = \frac{1 - \Delta\chi}{\text{stack volume}} \qquad \text{Equation 4.2}$$

Where C.D. is the connectivity density, $\Delta\chi$ is the difference of Euler characteristic between the intersections of voxels and stack edges.

4.3 Results

In this section, two results are compared. The TEM tomography of C-S-H 1.0 at curing temperature 20° C (Figure 3.7) and STEM tomography of C-S-H 1.0 at curing temperature 20° C (STEM_C-S-H 1.0) is shown in Figure 4.3.

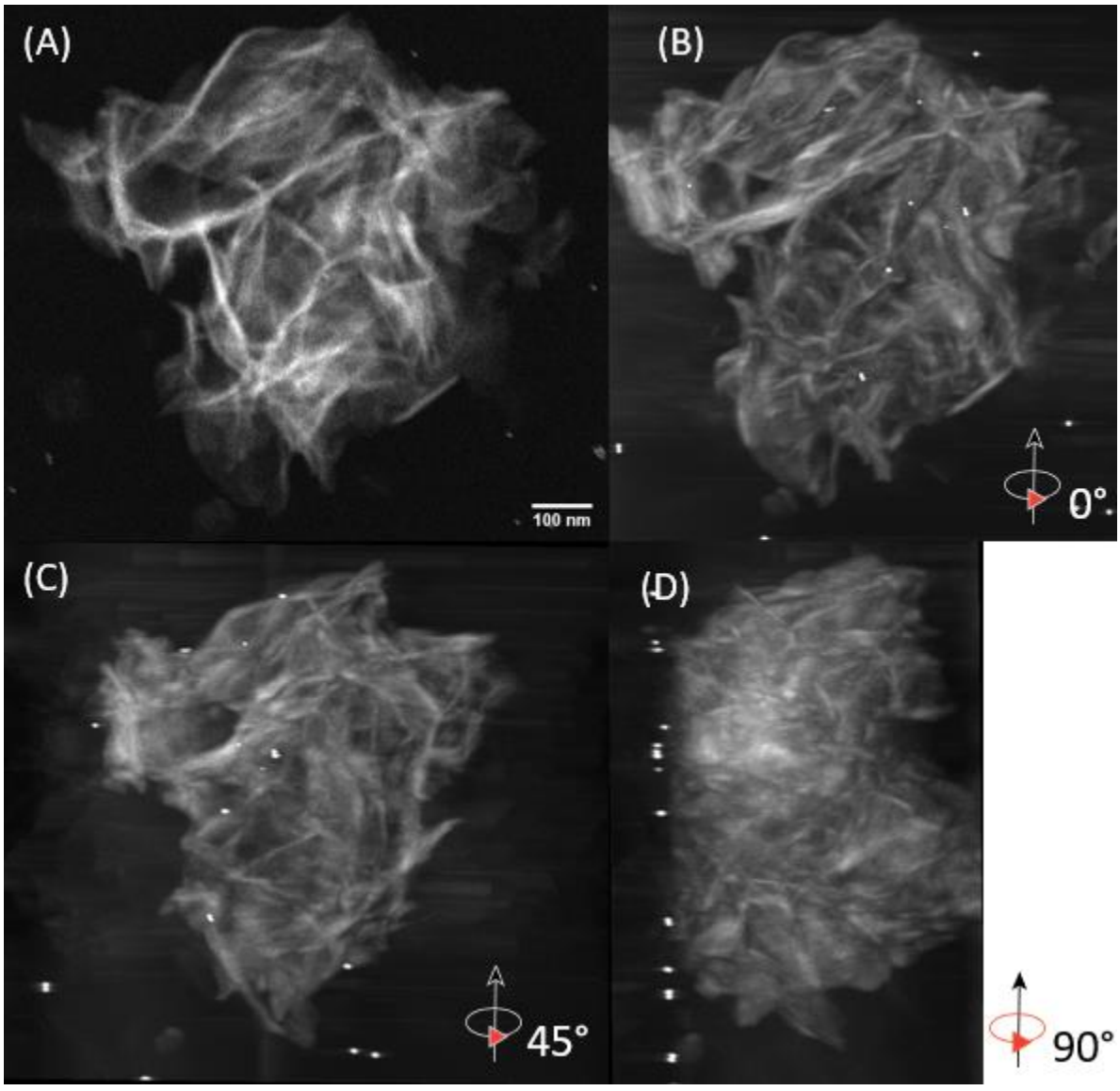

Figure 4.3 2D STEM image and 3D STEM reconstruction of C-S-H 1.0: (A) 2D image, (B) 3D at 0° rotation, (C) 3D at 45° rotation, (D) 3D at 90° rotation. The 3D image is a 2D section through the 3D model.

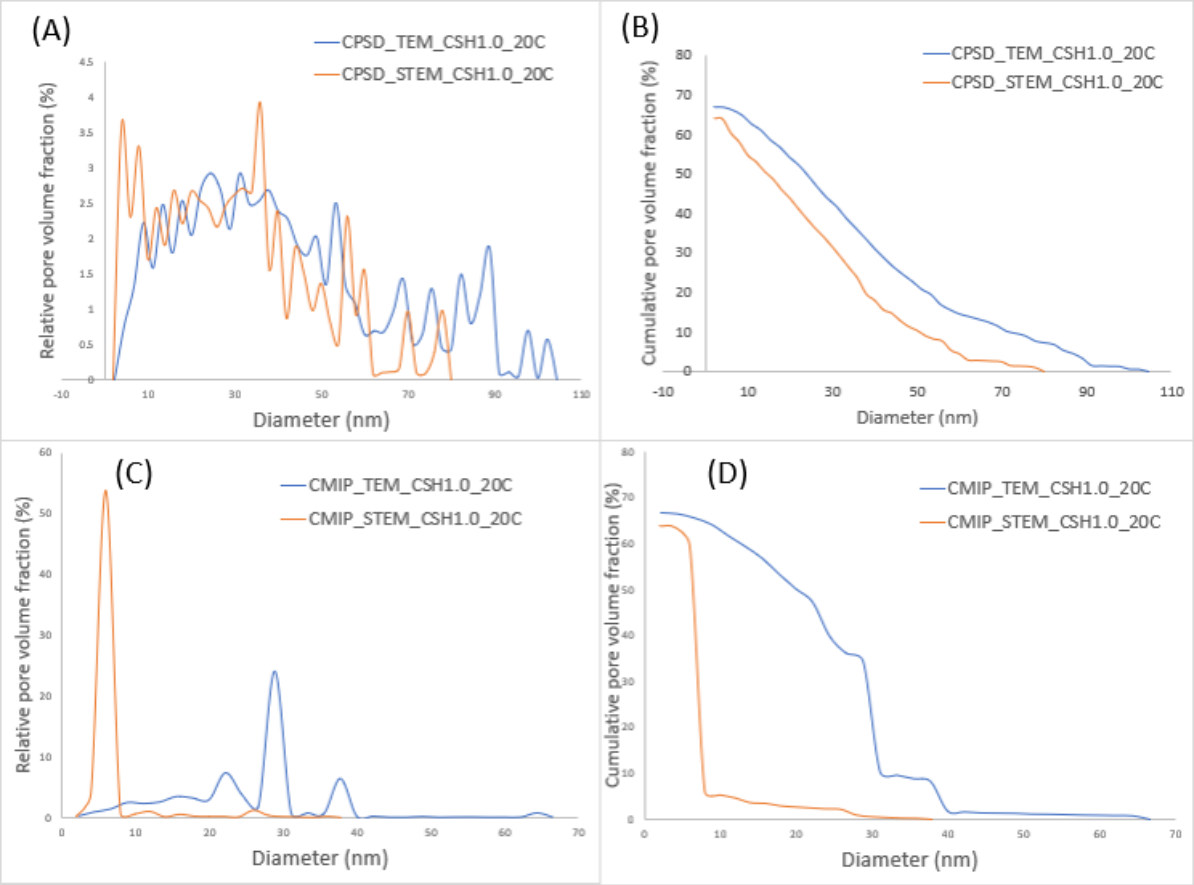

Figure 4.4 Pore size distributions of TEM_C-S-H 1.0 and STEM_C-S-H 1.0: (A) Continuous pore size distribution (CPSD), (B) Cumulative continuous pore size distribution (CCPSD), (C) Continuous pore size distribution with MIP simulation (CMIP), (D) Cumulative continuous pore size distribution with MIP simulation (CCMIP)

Table 4.1 Voxel size, porosity, pore size range, and connectivity density for C-S-H from TEM and STEM tomography

Sample	Voxel size (nm)	Porosity (%)	CPSD pore size range (nm)	CMIP pore size range (nm)	connectivity density (cm^{-3})
TEM_C-S-H 1.0	1.11	66.8	2 - 104	2 - 66	3.21E-03
STEM_C-S-H 1.0	1.40	63.9	2 - 80	2 - 38	7.60E-03

The morphologies of TEM_C-S-H 1.0 are similar to STEM_C-S-H 1.0. They are both made up of elongated, connected structures with different orientations. Also, there is no fiber-like structure in both samples. The voxel size, porosity, pore size range, and connectivity density of TEM_C-S-H 1.0 and STEM_C-S-H 1.0 are shown in Table 4.1.

The pore analysis shows that TEM_C-S-H 1.0 and STEM_C-S-H 1.0 have porosities of 66.8% and 63.9%, respectively. Continuous pore size distribution (CPSD) and Continuous pore size distribution with MIP simulation (CMIP) was analyzed in this research (Figure 4.4). CPSD (Figure 4.4A) reveals that TEM_C-S-H 1.0 has a pore size range between 2 – 110 nm, and STEM_C-S-H 1.0 has a pore size range between 2 – 75 nm. However, CMIP shows different results from CPSD. TEM_C-S-H 1.0 has three dominant peaks at 22.2, 28.8, and 37.7 nm, while STEM_C-S-H 1.0 has only one dominant peak at 6.0 nm. (Figure 4.4C). The connectivity density of TEM_C-S-H 1.0 is 3.21 x 10^{-3} cm^{-3} while STEM_C-S-H 1.0 is 7.60 x 10^{-3} cm^{-3}.

4.4 Discussion

There is no large difference in terms of morphologies for both 2D images or 3D models. Both TEM and STEM provide good quality images that can generate good 3D reconstructed models. The pore analysis in ImageJ suggests that TEM_C-S-H 1.0 has a little bit higher porosity than STEM_C-S-H 1.0 (66.8% and 63.9%, respectively). The cumulative pore size distribution for both CPSD and CMIP (Figure 4.4B, 4.4D) also indicates that TEM_C-S-H 1.0 has a higher porosity than STEM_C-S-H 1.0. The peak pore size for TEM_C-S-H 1.0 (Figure 4.4A, 4.4C) ranges from 2 to 110 nm, while for STEM_C-S-H 1.0, it ranges from 2 to 75 nm. There are also peaks with pore size larger than 100 nm for TEM_C-S-H 1.0 (Figure 4.4A, 4.4C) which means, the pore network's size of TEM_C-S-H 1.0 is significantly larger than of STEM_C-S-H 1.0. The connectivity density of STEM_C-S-H 1.0 is much higher than TEM_C-S-H 1.0. This result indicates that the pore network of STEM is denser than TEM. However, these results are not indicated that the two methods always give different results since they are the same sample.

From the results, there is no conclusion which methods is better. Both TEM and STEM have advantages and disadvantages for use in electron tomography for cementitious materials. TEM is more efficient compared to STEM due to the low probability of high-angle scattering required for STEM, especially for low-Z materials. Low-dose imaging is a strength of TEM, which is suitable for soft materials. STEM has the advantage that intensities of images are directly interpretable due to incoherent scattering.

Another advantage of STEM is that no Bragg diffracted electrons are collected due to the inner angle of the HAADF detector is made so larger than 50 mrad. The images, therefore, come from elastically scattered electrons that have passed very close to the atomic nuclei in the sample. STEM with HADDF works well with crystalline materials, but C-S-H are nanocrystalline materials, the image quality from STEM is not much different from conventional TEM.

Another point to consider is the stability of samples and beam damage. Since the STEM uses a focused beam of electrons to scan over a specimen, the exposure time to the electron beam is much longer. The samples may be moved or destroyed by the high-energy beam of the electron.

4.5 Conclusions

This chapter compared the result of C-S-H 1.0 at curing temperature 20° C from TEM and STEM tomography. The porosity from ImageJ shows that both TEM_C-S-H 1.0 and STEM_C-S-H 1.0 are not much different. However, the continuous pore size distribution with MIP simulation (CMIP) is different. The pore network's size of TEM_C-S-H 1.0 is significantly larger but less dense than STEM_C-S-H 1.0. Both TEM and STEM show the capability to determine the 3D nanostructure of cementitious materials.

5. A model of fluid flow in C-S-H and C-A-S-H

5.1 Introduction

Porosity plays an important role in cement and concrete system. It can affect the mechanical properties of concrete such as the compressive strength-modulus of elasticity relationship (e.g. Popvics, 1973). Also, porosity has an important role in the frost resistance of concrete (Zhou et al., 2006; Zuber & Marchand, 2000). The ability of ions to migrate through cementitious materials influences the extent of several degradation mechanisms such as sulphate attack, carbonation, leaching, chloride transport in marine structures and contaminant transport in hazardous waste disposal systems (Patel et al., 2014, 2018). Therefore, improving the understanding of the transport mechanisms through cementitious materials is very important for predicting the long-term performance and service life of concrete structures.

The mathematical modeling of the flow in a porous system can be based on Darcy's law:

$$q = -\frac{k}{\mu}\nabla p \qquad \text{Equation 5.1}$$

q is the flux or discharge per unit area (m/s), k is the permeability (m^2), μ is the dynamic viscosity of the fluid (Pa·s), ∇p is the pressure drop (Pa).

The permeability of the 3D image is computed using Darcy's law by applying pressure gradient in the direction of interest. For this study, we apply pressure gradient in the x-direction. With these given boundary conditions fluid flow equation described later is solved to obtain a steady-state fluid velocity field inside the porous media. Using this steady-state velocity field, permeability can be computed as

$$\kappa_x = \frac{\langle u_x \rangle \mu}{\mathrm{d}P/\mathrm{d}X} \qquad \text{Equation 5.2}$$

Where, $\langle u_x \rangle$ is the average fluid velocity in the x-direction in the computational domain at steady state, κ is permeability, and $\mathrm{d}P/\mathrm{d}X$ is the applied pressure gradient in the x-direction. The pressure gradient is applied using a forcing scheme.

The average velocity in x-direction used for permeability computation is then computed from the velocity field as

$$\langle u \rangle = \frac{1}{V} \int_V u \, dv \approx \frac{1}{N} \sum_{N_f} u_x \qquad \text{Equation 5.3}$$

Where N_f are the number of fluid voxels, and N is the total number of voxels in the image.

To obtain the velocity to compute permeability, one needs to solve continuity and Navier-Stokes (NS) equations in the pore geometry

$$\nabla . \mathrm{u} = 0 \qquad \text{Equation 5.4}$$

$$\rho \frac{\partial \mathrm{u}}{\partial t} + \rho \mathrm{u} . \nabla \mathrm{u} = -\nabla \mathrm{P} + \mu \nabla^2 \mathrm{u} + \mathrm{F} \qquad \text{Equation 5.5}$$

where ρ is density, u is velocity, P is pressure, μ is dynamic viscosity, and F is body force.

The above equation is solved in this work using two relaxation time lattice Boltzmann method (Talon et al., 2012) implemented in open source code yantra (Patel, 2016). In LBM, instead of discretizing NS equations directly it solves the discretized version of the lattice Boltzmann equation (discretized in velocity space and physical space), which describes the behavior of probability distribution function of the particles (f). It can be shown that this discretized lattice Boltzmann equation can recover the NS equations using multiscale Chapman-Enskog expansion.

The two-relaxation time lattice Boltzmann method scheme provides additional tuning parameter which can be used to remove error terms related to no-slip boundary conditions on solid walls. In two relaxation time, the symmetric ($\mathrm{f_i^+}$)and anti-symmetric ($\mathrm{f_i^-}$) components of the distribution function defined below using separate relaxation parameters.

$$\mathrm{f_i^+} = \frac{\mathrm{f_i + f_{-i}}}{2} \;\&\; \mathrm{f_i^-} = \frac{\mathrm{f_i - f_{-i}}}{2} \qquad \text{Equation 5.6}$$

Where $\mathrm{C_i} = -C_i$. $\mathrm{c_i}$ is the discrete velocity of lattice defined later. The corresponding governing lattice Boltzmann equations is given as below []

$$\mathrm{f_i(x + c_i \Delta t, t + \Delta t) = f_i(x, t) + \Omega_i^+(f) + \Omega_i^-(f) + F_i^{LB} \Delta t} \qquad \text{Equation 5.7}$$

Where

$$\Omega_i(f)^{+/-} = \frac{-\Delta t}{\tau_{+/-}}(f_i^{+/-} - f_i^{eq\,+/-}) \quad \text{Equation 5.8}$$

$$f_i^{eq} = w_i \rho \left(1 + \frac{u.c_i}{c_s^2} + \frac{(u.c_i)^2}{2c_s^4} - \frac{u.u}{2c_s^2}\right) \quad \text{Equation 5.9}$$

$$F_i^{LB} = \Delta t\, w_i \left(1 - \frac{\Delta t}{2\tau_+}\right) F_\alpha^{TRT+} + \Delta t\, w_i \left(1 - \frac{\Delta t}{2\tau_-}\right) F_\alpha^{TRT-} \quad \text{Equation 5.10}$$

$$F_\alpha^{TRT} = \left(\frac{c_i - u_\alpha}{c_s^2} + \frac{c_i u_\alpha}{c_s^4} c_i\right) F_\alpha \quad \text{Equation 5.11}$$

$$c_s{}^2 = \frac{1}{3}.\left(\frac{\Delta x}{\Delta t}\right)^2 \quad \text{Equation 5.12}$$

In the above equations, Δx and Δt are space and time resolutions. f_i is discrete velocity distribution function, f_i^{eq} is equilibrium distribution function and τ_+ and τ_- are relaxation time for symmetric and anti-symmetric components of the distribution function. Discrete velocities c_i and their corresponding set of weighing coefficients w_i will form velocity sets.

5.2 Experimental Methods

The data used in this section are selected from the models from Chapter 3. Sample details are shown in Table 5.1. The cropped 3D model of C-S-H 1.0 at curing temperature 7° C is shown in Figure 5.1. The porosity is determined by ImageJ, referred to section 3.4.3.

The simulation of fluid flow is based on Darcy's law and the lattice Boltzmann method. The flux and dynamic viscosity are fixed. Then a constant gradient pressure is applied to all cropped models only in the X-direction. After the simulation, the permeability is generated.

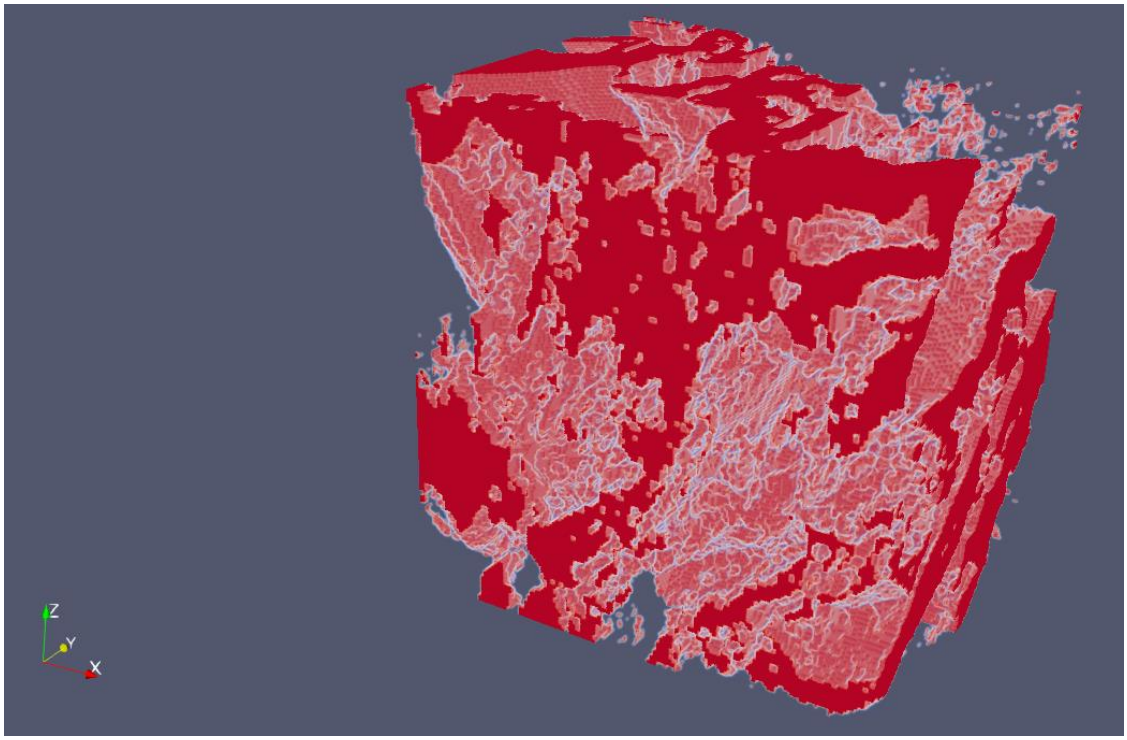

Figure 5.1 Cropped model of C-S-H 1.0 at 7° C from TEM tomography

5.3 Results and Discussion

Table 5.1 Details of 3D tomography models, porosity, and permeability for all samples.

Data	Original 3D model	Porosity (%)	Permeability (m^2)
Crop1	C-S-H 1.0 at 7° C	50.1	6.31E-19
Crop2	C-S-H 1.0 at 20° C	59.8	4.23E-18
Crop3	C-S-H 1.0 at 50° C	76.2	6.58E-18
Crop4	C-S-H 1.4 at 20° C	83.3	6.99E-18
Crop5	C-A-S-H 1.0, A/S 0.05 at 50° C	55.4	1.55E-18

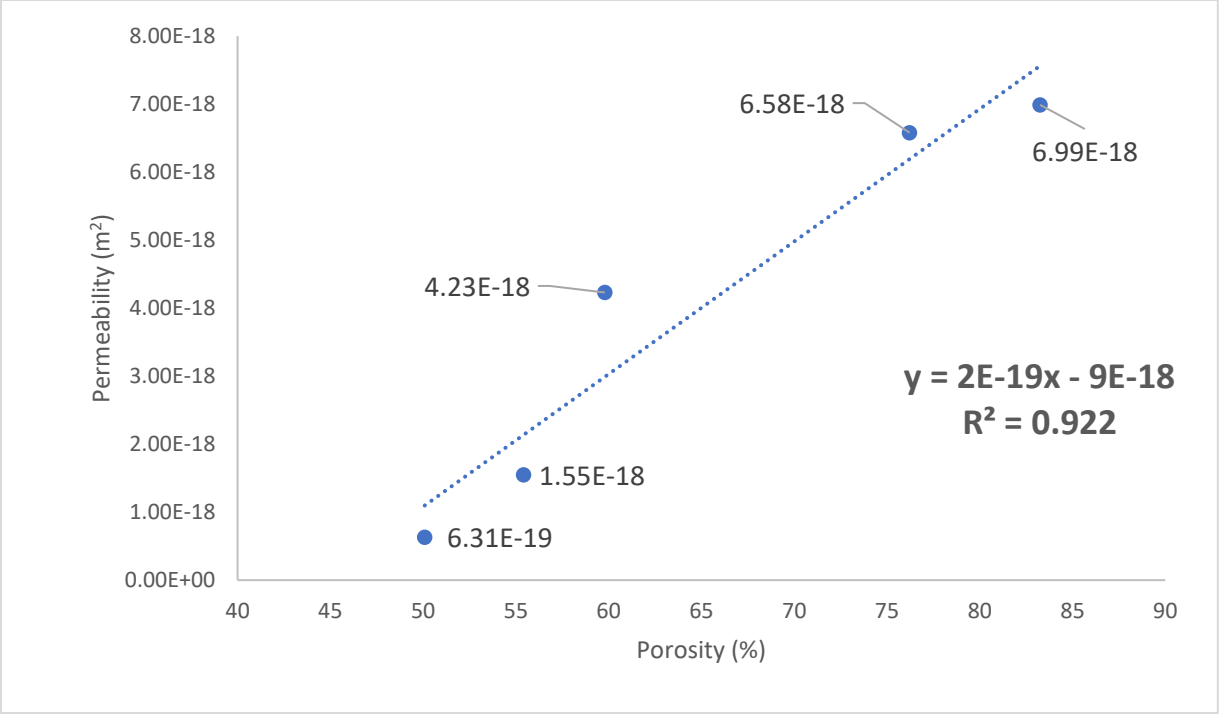

Figure 5.2 Graph shows relationship between porosity (%) and permeability (m^2) of 5 cropped samples

From Table 5.1, the porosity of all data ranges from 50.1 to 83.3%. The permeability ranges from $6.31x10^{-19}$ to $6.99x10^{-18}$ m^2. Figure 5.2 shows the graph between porosity and permeability show a very good linear relationship (R^2 = 0.922). This indicates the promising results for a good model of fluid flow.

The pores sizes range of cement pastes varies from nanometre spaces within the C-S-H to micron-sized capillary pores. This difference has a huge impact on the permeability of the system (Patel et al., 2018). The former research (Banthia & Mindess, 1989; Nyame & Illston, 1981; Song et al., 2019; Vichit-Vadakan & Scherer, 2003; Wong et al., 2009; Ye, 2005; Zalzale et al., 2013) on permeability values reported in the literature vary widely from 10^{-22} to 10^{-16} m^2 for cement pastes with various water-to-cement (w/c) ratios. Although the experimental conditions of this literature and our models are not identical, the results on permeability, which are range from $6.31x10^{-19}$ to $6.99x10^{-18}$ m^2, show a promising result on model fitting.

From the results, there are several characteristics between chemical composition, equilibrated temperatures, porosity, and permeability. Both porosity and permeability increase with samples with a higher Ca/Si ratio and higher

equilibrated temperatures. The stability of C-S-H depends on the permeability. If the water quickly flows through the structure, the deterioration, including corrosion of steel reinforcement, and freeze-thaw attack, occurred at a faster rate too (Dolado & van Breugel, 2011). These results indicate that the stability of C-S-H depends on the chemical compositions and equilibrated temperatures.

5.4 Conclusions

This chapter has presented a preliminary study of the flow model. The data show that the stability of C-S-H depends on the chemical compositions and equilibrated temperatures. The results show a good relationship between porosity and permeability and provide new insight into a fluid flow model of cementitious materials. However, more data need to be calculated to generate robust models. The successful model will enhance the understanding of the relationship of mechanical properties and porosity of cement and concrete.

6. Conclusions and further work

In this dissertation, electron tomography was applied to study synthetic C-S-H and C-A-S-H with various Ca/Si ratios and curing temperatures. The experimental studies include:

- Beam damage on TEM tomography
- Effects of Ca/Si ratio on the microstructure of C-S-H
- Effect of curing temperature on the structure of C-S-H and C-A-S-H
- Comparison between TEM and STEM tomography
- A model of fluid flow in C-S-H and C-A-S-H

The resulting information of pore analysis is critical for the development of a new generation of optimized green cement. The important conclusions from each chapter are listed below.

1. TEM tomography with simultaneous iterative reconstruction technique (SIRT) can generate the 3D reconstruction of C-S-H and C-A-S-H microstructures which can be found in Portland cement paste or C3S paste. The highest beam dose that can achieve this without significant beam damage is 5000 e-/(nm^2 s) for all samples. The 3D reconstructions and selected ROI analysis confirm that there are only foil-like structures for all C-S-H and C-A-S-H samples. Both CPSD and CMIP reveal that most of the pore sizes of all samples are below 40 nm. However, C-S-H1.0_AS0_20C, C-S-H1.6_AS0_20C, C-A-S-H1.0_AS0.05_7C, and C-A-S-H1.0_AS0.05_80C seem to have larger pore size than the rest. The higher curing temperature will make the lower porosity in the structure of both C-S-H and C-A-S-H. TEM tomography combine with the Beat plugin in ImageJ shows the capability to determine the 3D nanostructure and pore networks of C-S-H and C-A-S-H.

2. Both TEM and STEM tomography show the capability to determine the 3D nanostructure of cementitious materials. The 3D results of both TEM and STEM tomography show no distinguished difference, but the continuous pore size distribution with MIP simulation (CMIP) shows an outstanding difference. The pore network's size of TEM_C-S-H 1.0 is significantly larger but less dense than STEM_C-S-H 1.0.

3. A fluid flow model's preliminary results show a good relationship between porosity and permeability and provide new insight into a model of fluid flow of cementitious materials. Both porosity and permeability increase with samples with a higher Ca/Si ratio and higher equilibrated temperatures. The stability of C-S-H depends on the chemical compositions and equilibrated temperatures.

Based on the results of this dissertation, a few suggestions for future investigations of cementitious materials, designing high performance and green concrete can be addressed here:

- Studies of real hydration products like C_3S or cement paste to compare the results with idealized systems.
- Some advanced reconstruction methods like the algebraic reconstruction technique (ART), the equal slope tomography (EST) that can solve the missing wedge and other artifact problem better than the simultaneous iterative reconstruction technique (SIRT). However, these methods required longer analysis time, complex methodology, and high-performance computers.
- To generate models of fluid flow, more data are needed to confirm the results.

7. Appendix

7.1 Create a 3D model with Tomviz

Tomviz is an open source application for the processing, visualization, and analysis of 3D tomographic data. It can render and analyze voluminous 3D tomograms. The platform provides a graphical interface where objects can be rendered as shaded contours or volumetric projections. Tomographic reconstructions of experimental data are possible within Tomviz. This manual refers to the Tomviz version 1.8.0. First, the reconstruction is a lengthy work. To avoid any errors, saving state often by going to the File tab and clicking “Save State”. This saves a .tvsm file. To continue or recover your work, .tvsm files can be loaded into tomviz by going to File and clicking “Load State”.

1. Loading data set

   Go to File > Open Data
   Normal data sets are usually in .tiff or .mrc files.

2. Define tilt serie

   Go to tomography> Mark Data as Tilt Series
   Set number of images that want to use and the overall angle of the experiment.

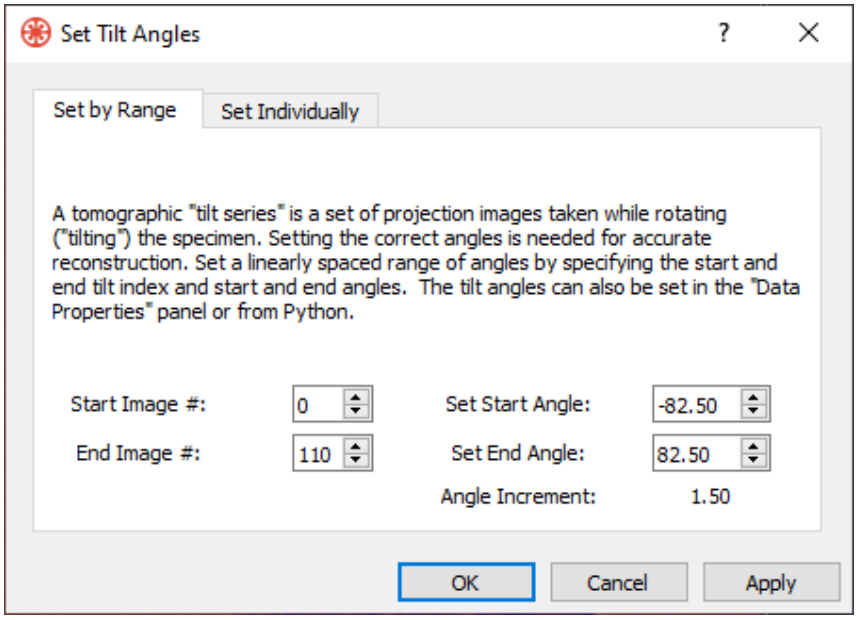

Figure 7.1 Set tilt angles in Tomviz

3. Image alignment

Go to tomography> Image Alignment (Manual)

Image Alignment (Manual) allows the user to align the data by manually shifting the images so that the position of fiducial markers are the same in every image. Manual alignment to very small fiducial particles is a very accurate and commonly used alignment method.

There are two display modes. “Toggle Images” flashes between two images that are being aligned at a frame rate specified by the user. “Show Difference” maps the difference in value between two images being aligned, plotted on a color scale specified by the user (Blue to Red shown below),

Images can be aligned to the previous image in the tilt series, the next image in the series, or to a fixed reference image in the series. Use the keyboard’s arrow keys to shift the images until the fiducial particles line up, or enter shifts manually into the shift array in the lower right of the dialog box.

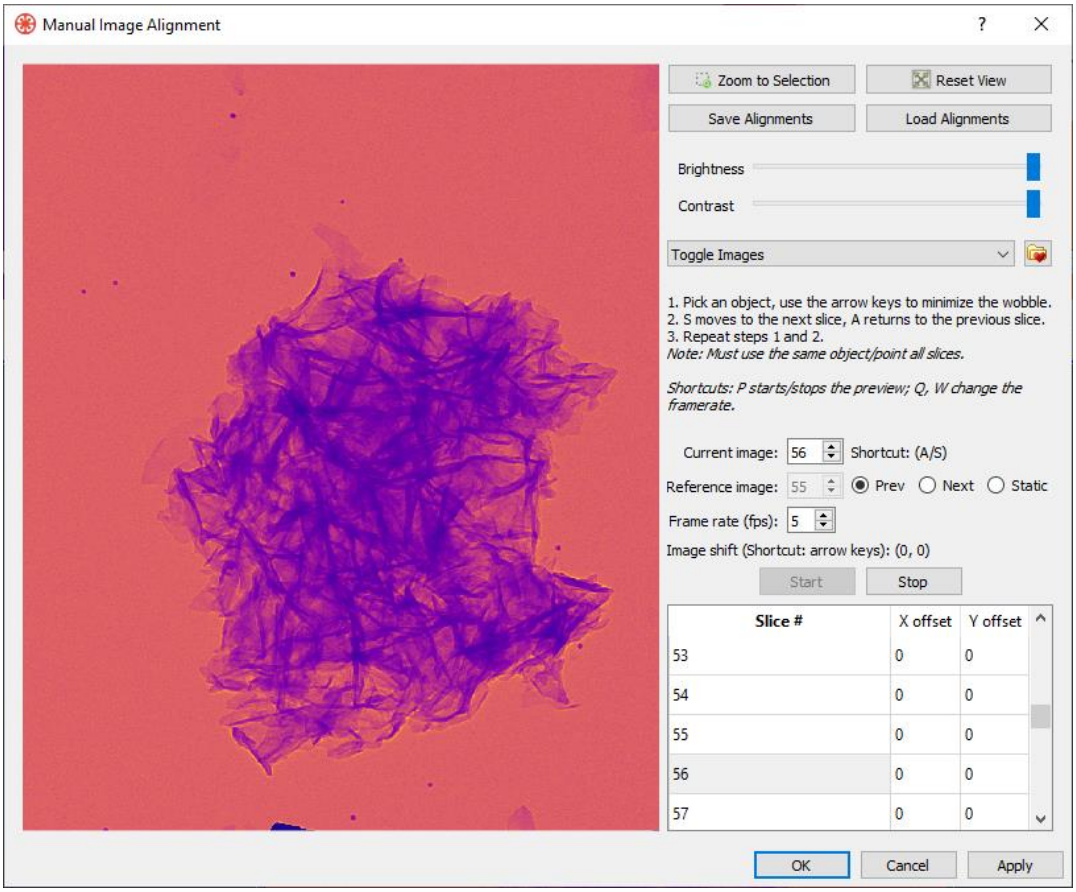

Figure 7.2 Manual image alignment in Tomviz

4. Tilt axis alignment

   Go to tomography> Tilt Axis Alignment (Manual)

   This brings up another dialog box. Here, you choose 3 slices (shown by the red lines), and the software computes a quick reconstruction showing you what each of those slices through the 3D volume will look like with your current tilt axis alignment. You should put one of your slices on a fiducial particle, and place the other two on interesting features of the sample if possible.
   Adjust the angle and position of the tilt axis (yellow line) to minimize artifacts. For example, the fiducial nanoparticles should be spherical but may appear crescent-shaped if the tilt axis is in the wrong position.
   The color map for each reconstructed slice can be changed separately to aid users in searching for artifacts. Once satisfied that the tilt axis is correct,

click “Transform Data to Axis of Rotation”. Wait for the software to transform the data, and then proceed to reconstruction.

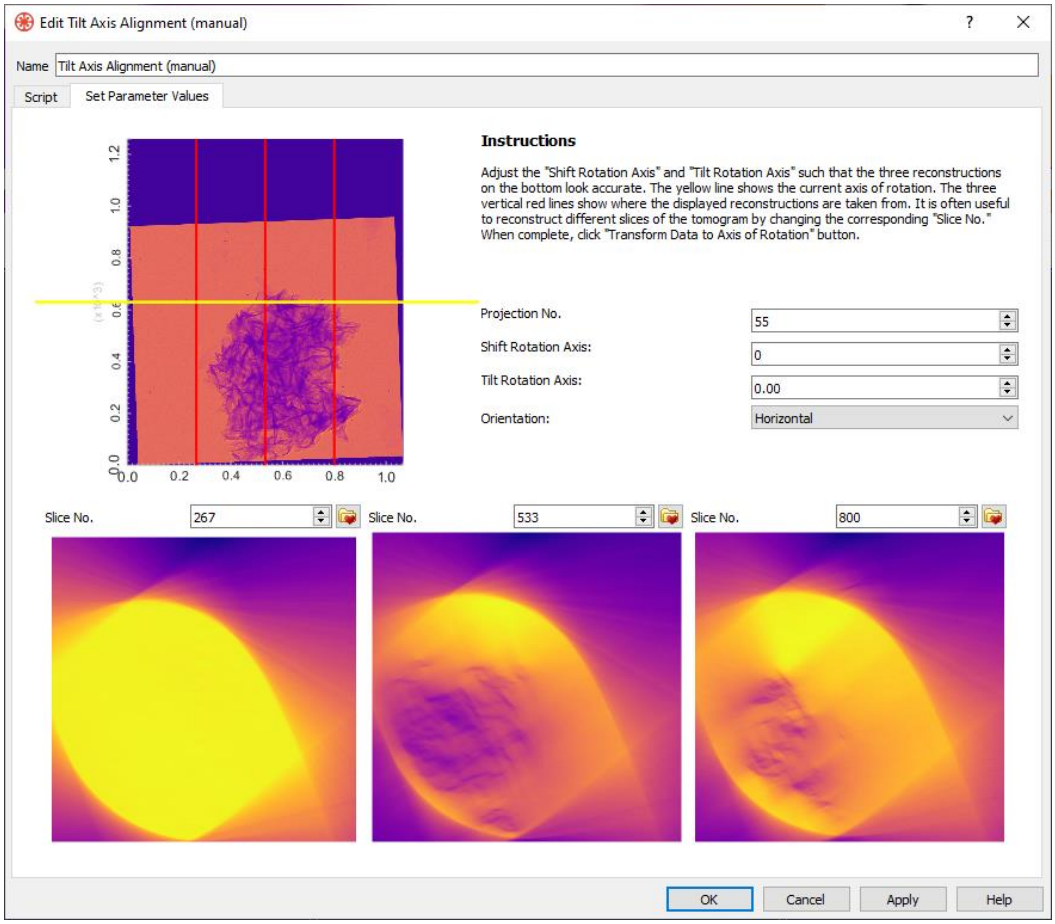

Figure 7.3 Manual tilt axis alignment in Tomviz

5. 3D reconstruction

   Go to tomography> Weighted Back Projection or Simultaneous Iterative Recon. Technique(SIRT)

   This step may take several hours to complete depend on tge reconstruct condition.

6. Visualizing 3D Data

Click the volume icon (the purple square at the far right) to see the 3D volume data.
Sometime, it may be good to see the contour by click the green contour icon (Second to the left).

Figure 7.4 Visualizing icons

7. Save model

   Go to File > Save Data

   The model can be saved either in .emd or .tiff files.

7.2 Create a 3D model with Etomo

Another method that can generate 3D model is Etomo. Etomo is a software based on linux system. Using Etomo on Windows is possible but not recommended due to many bugs and uncompatible issues.

In this manual, we refer to Etomo version 4.11.

1. Opening program
   Open the terminal (Ctrl + Alt + T) then type etomo. Click Built Tomogram.

2. Loading data set (Figure 7.5)

   - The files that can be opened are .st files. If your file is in .tiff or .mrc, you can just change it to .st file.
   - Select “Single axis”
   - Click “Scan Header”
   - Fill the the fiducial diameter size.
   - Click “Create Com Scripts”

3. Coarse Alignment (Figure 7.6)

   - Click “Calculate Cross-Correlation”
   - Click “Generate Coarse Aligned Stack”
   - Click “Done”

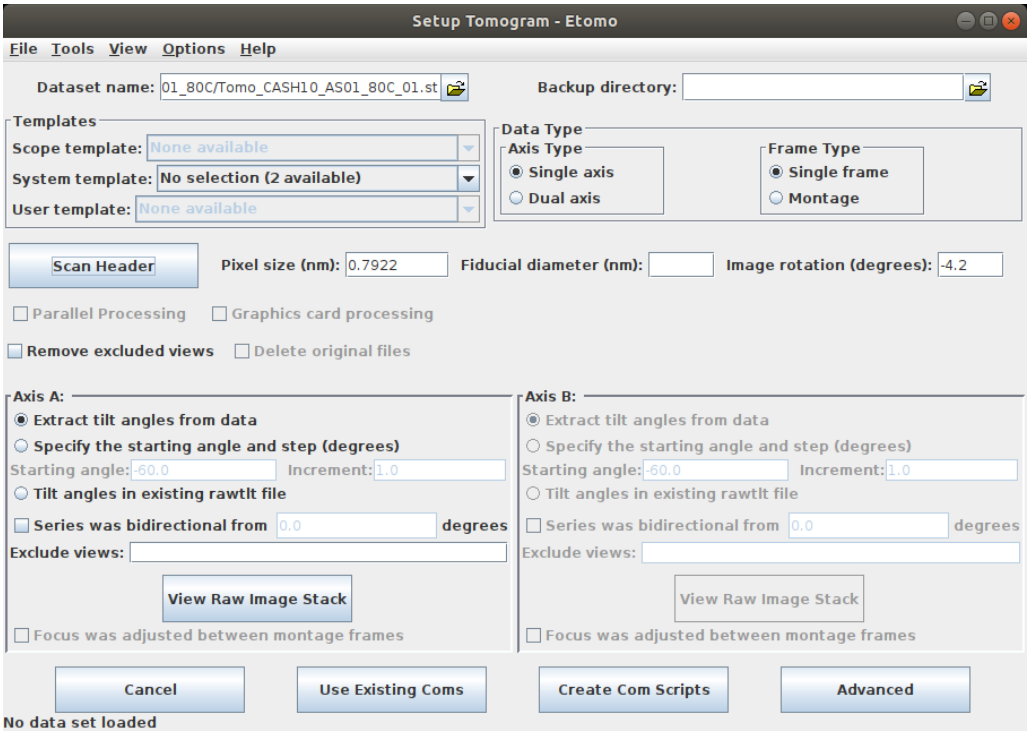

Figure 7.5 Setup tomogram in Etomo

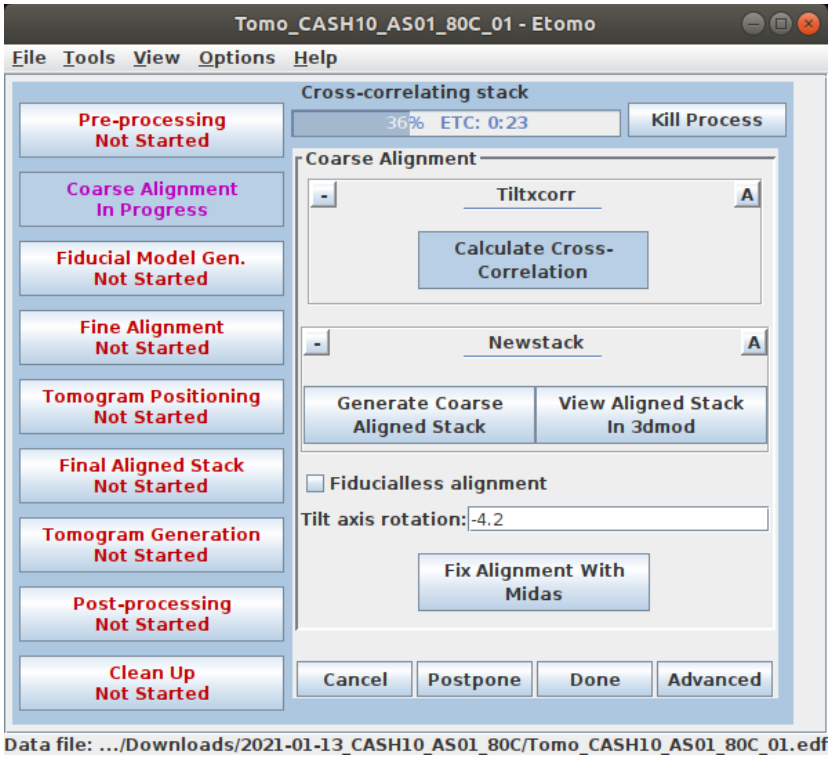

Figure 7.6 Coarse Alignment in Etomo

4. Fiducial model

- Click “Fiducial Model Gen.”.
- Fill the total number of fiducial markers in total number
- Click “Generate Seed Model”.
- Click tab “Track Beads”.
- Click “Track Seed Model” then click “Fix Fiducial Model” (Figure 7.8).
- Use the Page Up key (when an up arrow is above the point) or the Page Down key (when a down arrow is above the point) to find the section with the missing point and use the middle mouse button to add the point in the center of the fiducial markers (Figure 7.9).

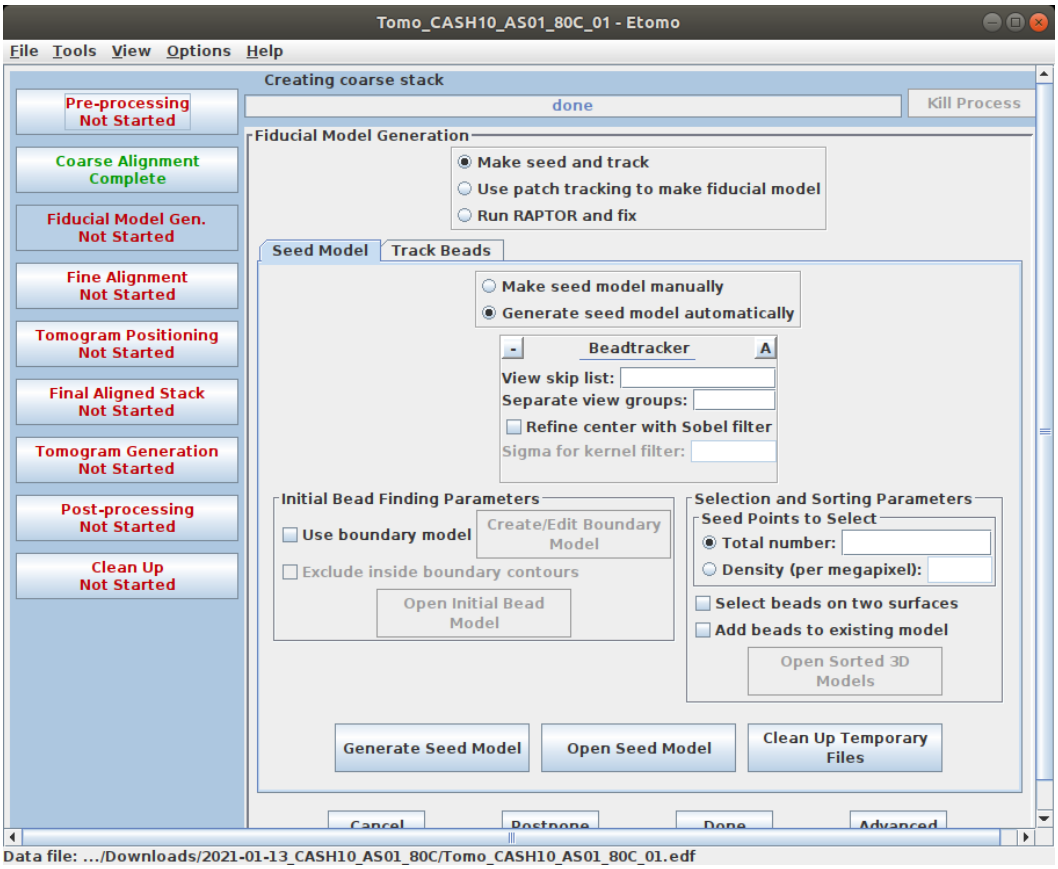

Figure 7.7 Fiducial Model Generate in Etomo

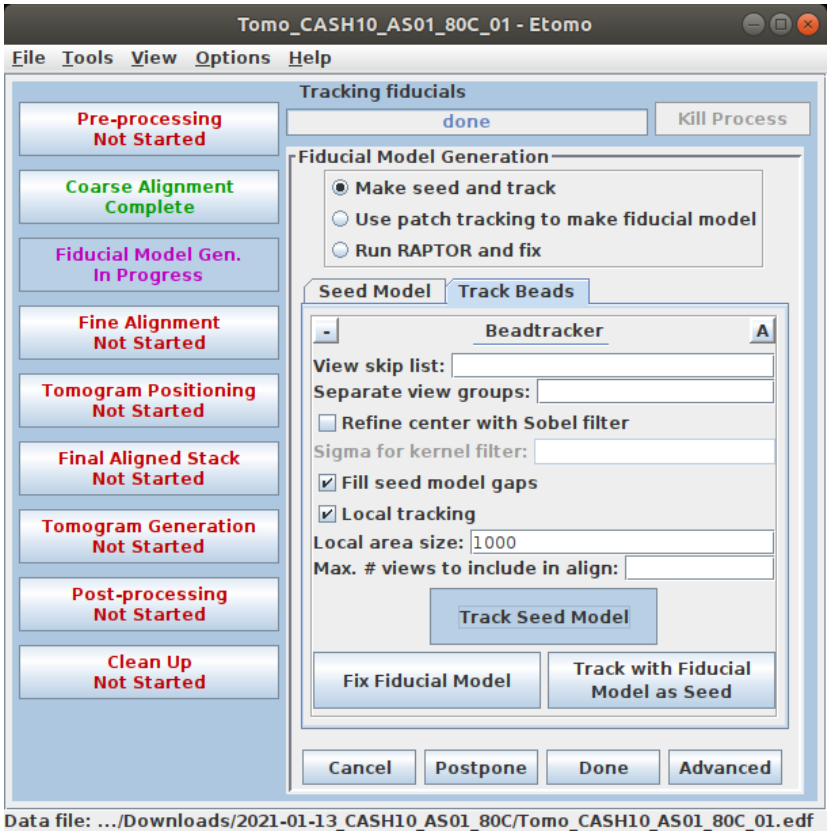

Figure 7.8 Fiducial Model Generate in Etomo (2)

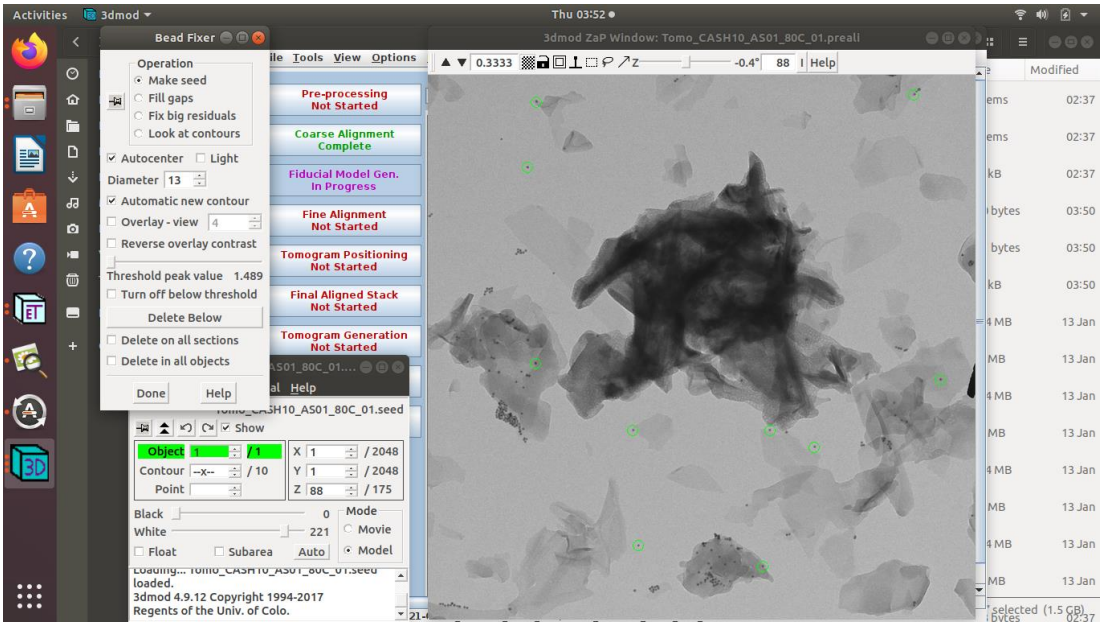

Figure 7.9 Fix Fiducial Model in Etomo

5. Fine Alignment

- Set all parameters as Figure 7.10 and Figure 7.11 then click “Compute Alignment”.
- Click “Done”.

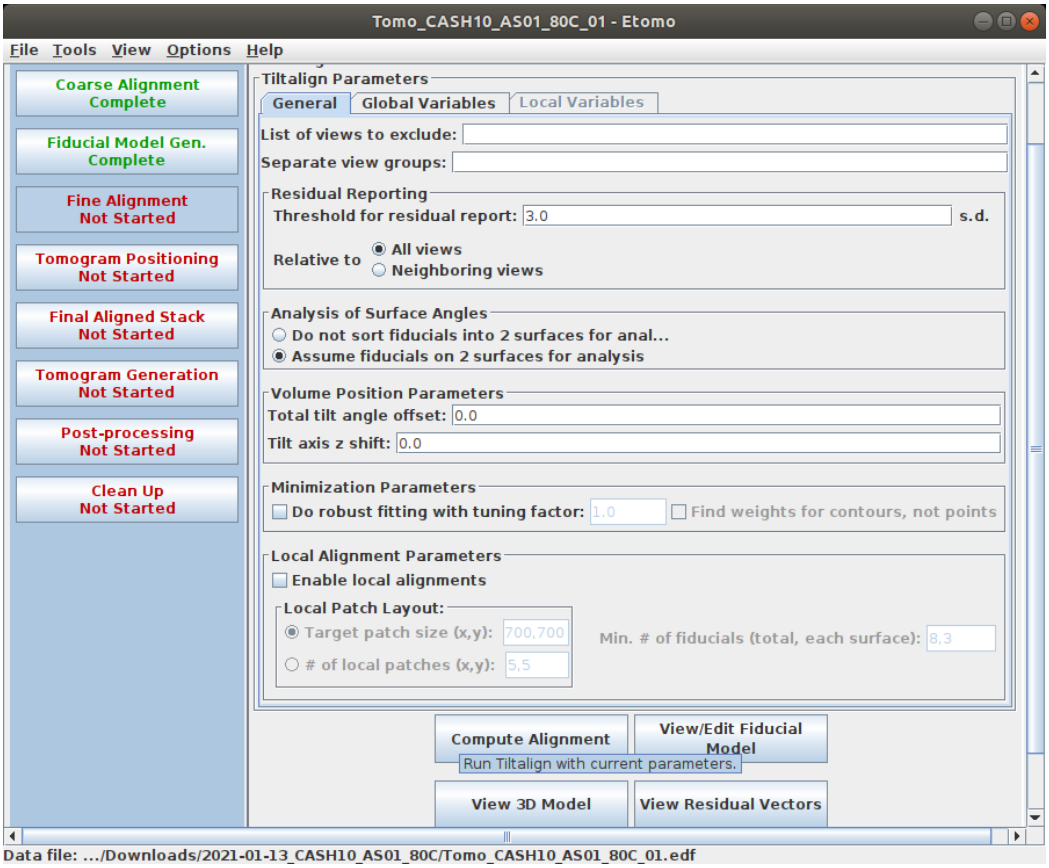

Figure 7.10 Fine Alignment in Etomo

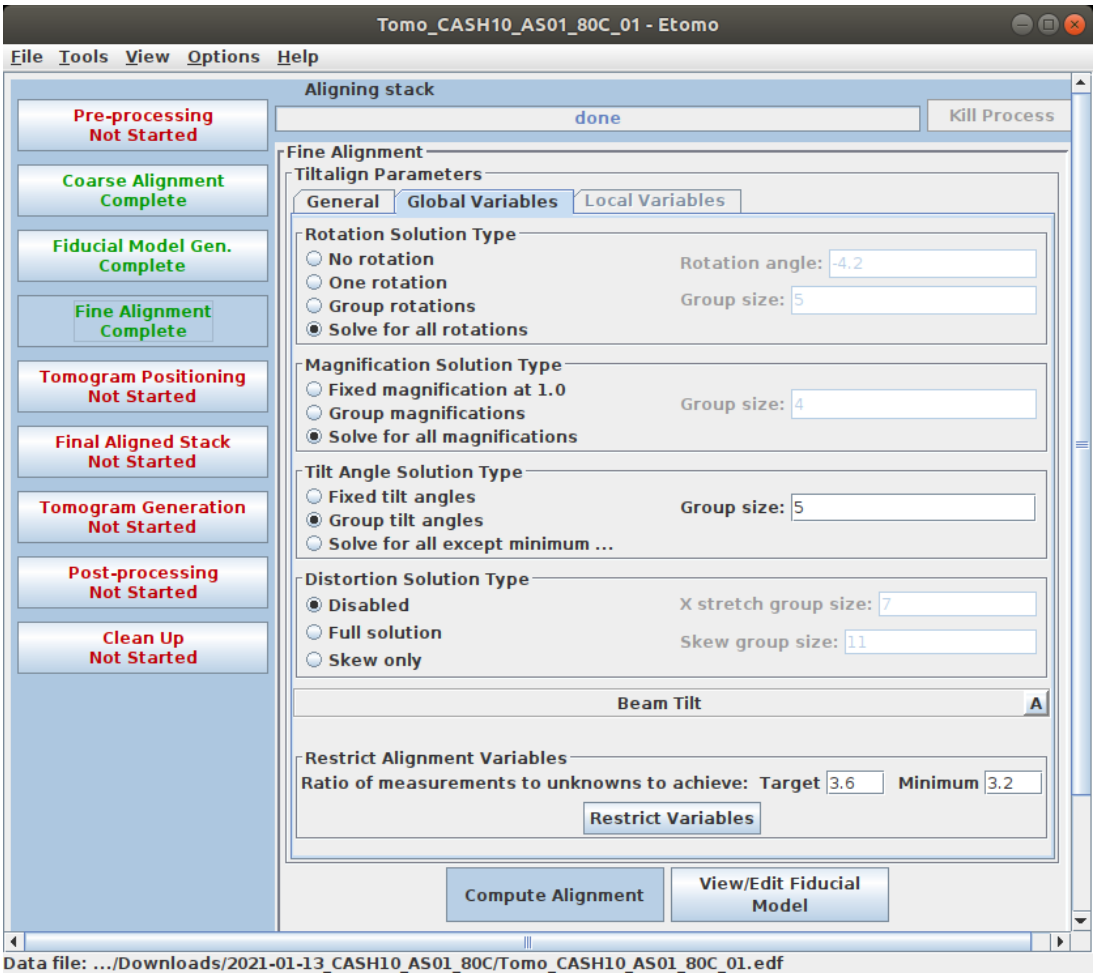

Figure 7.11 Set Global Variables in Etomo

6. Tomogram Positioning

- Set thickness to 2000
- Click “Create Sample Tomograms”.
- Click “Create Boundary Model”.
- Click “Compute Z Shift & Pitch Angles”.
- Click “Create Final Alignment”.
- Click “Done”.

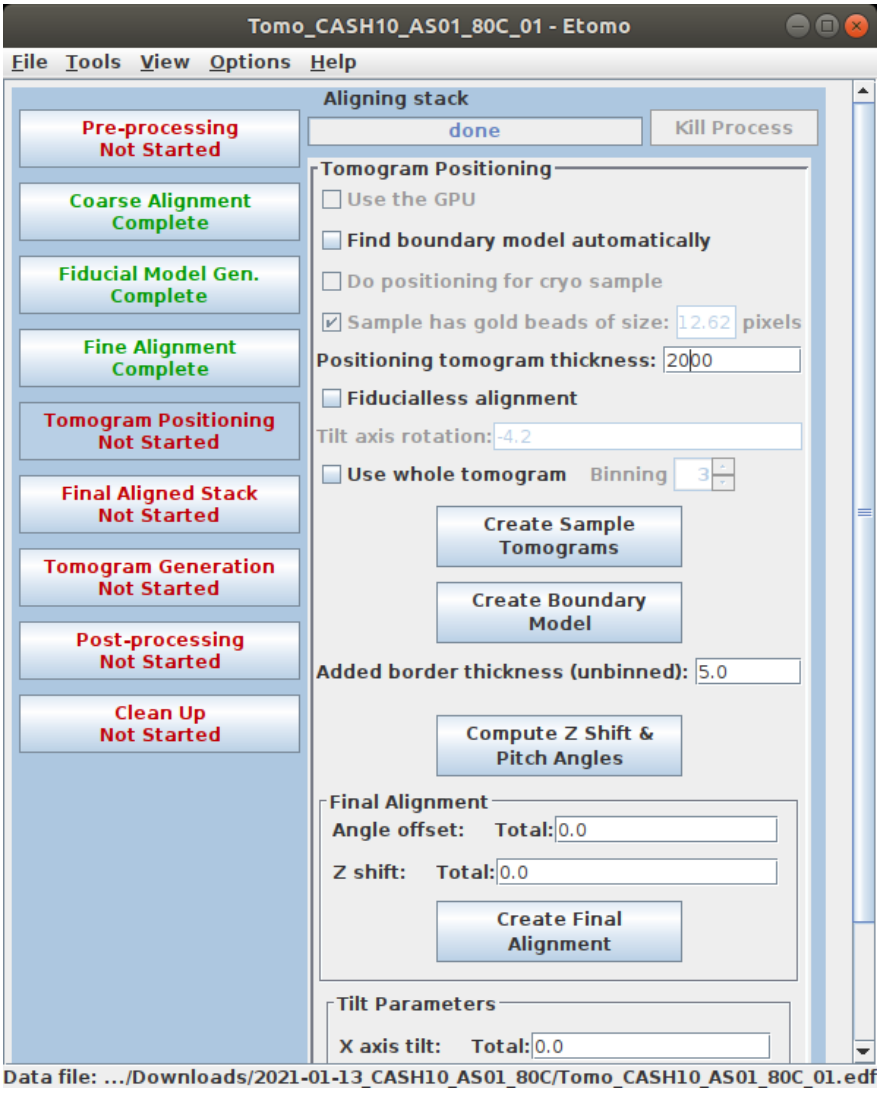

Figure 7.12 Tomogram Positioning in Etomo

7. Final Aligned Stack

- Set binning to “2”.
- Click “Create Full Aligned Stack”.
- Click “Done”.

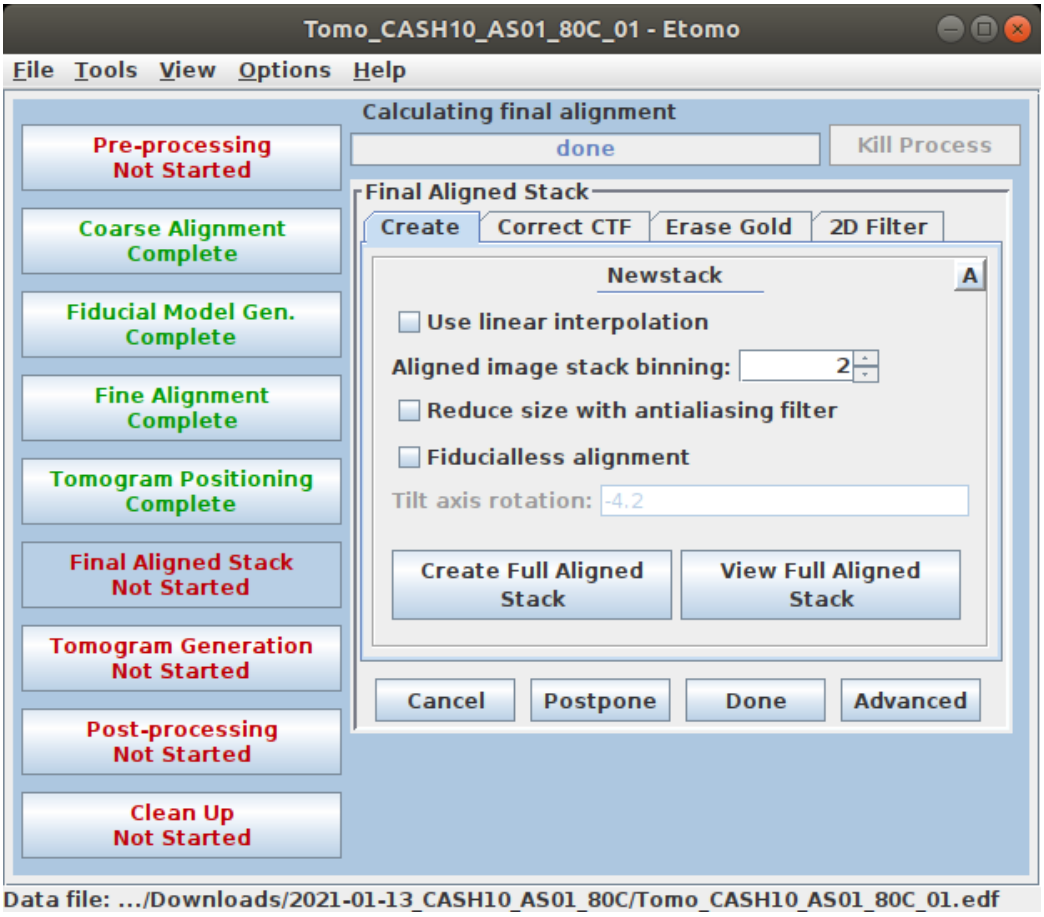

Figure 7.13 Final Aligned Stack in Etomo

8. Tomogram Generation

- Click “Back Projection” or “SIRT”
- If SIRT is selected, fill the number of iteration (can be filled more than one number).
- Click “Generate Tomogram”.
- Wait for several hours, depend on the number of iteration.
- The reconstructed model will be saved in .srecxx ,where xx is the number of iteration.
- To open the file in Tomviz, just change .srecxx to .rec.

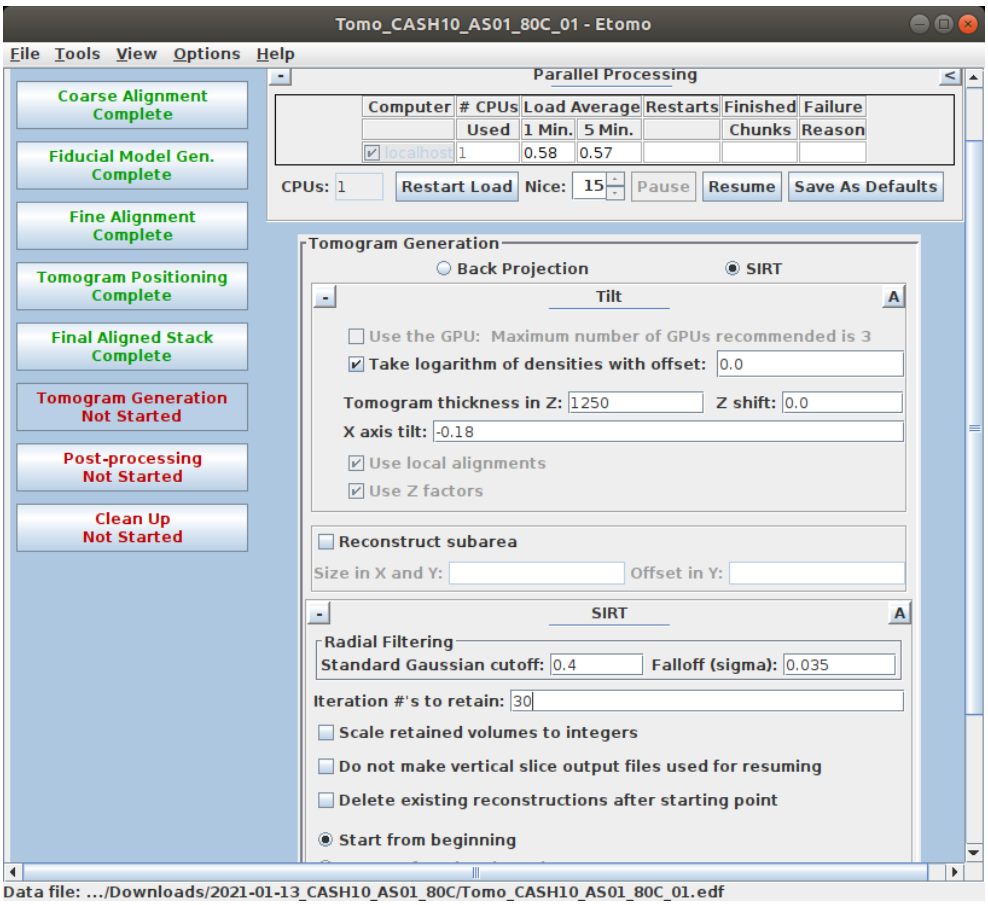

Figure 7.14 Tomogram Generation in Etomo

7.3 Visualization with napari

Napari is the software that help visualization 3D model. It also . This software can be downloaded from https://github.com/napari/napari. It can be installed as standalone software or python code.

1. First, click File > Open. Then select the data. Click the cube icon at the bottom to convert stack of 2D images to 3D model (Figure 7.15).

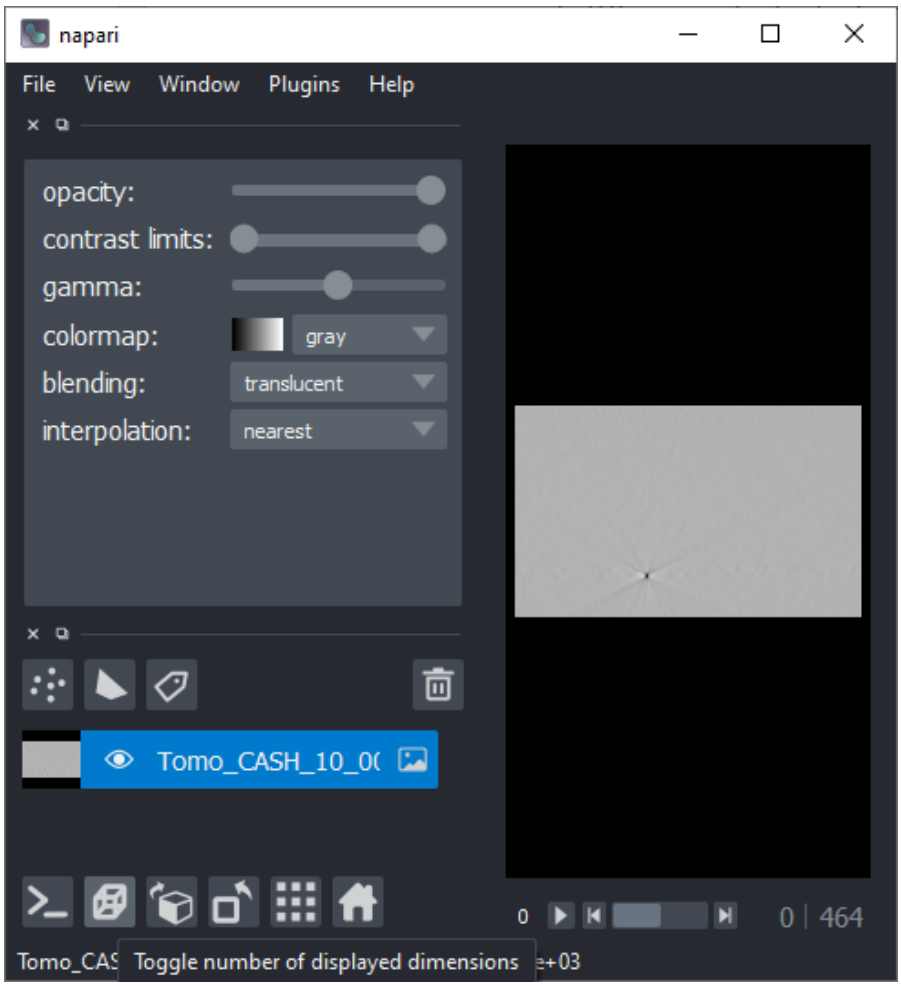

Figure 7.15 Software napari

2. Next, set the rendering package on the left console to “minip” to better see the model (Figure 7.16). Sometime, the default package (mip)

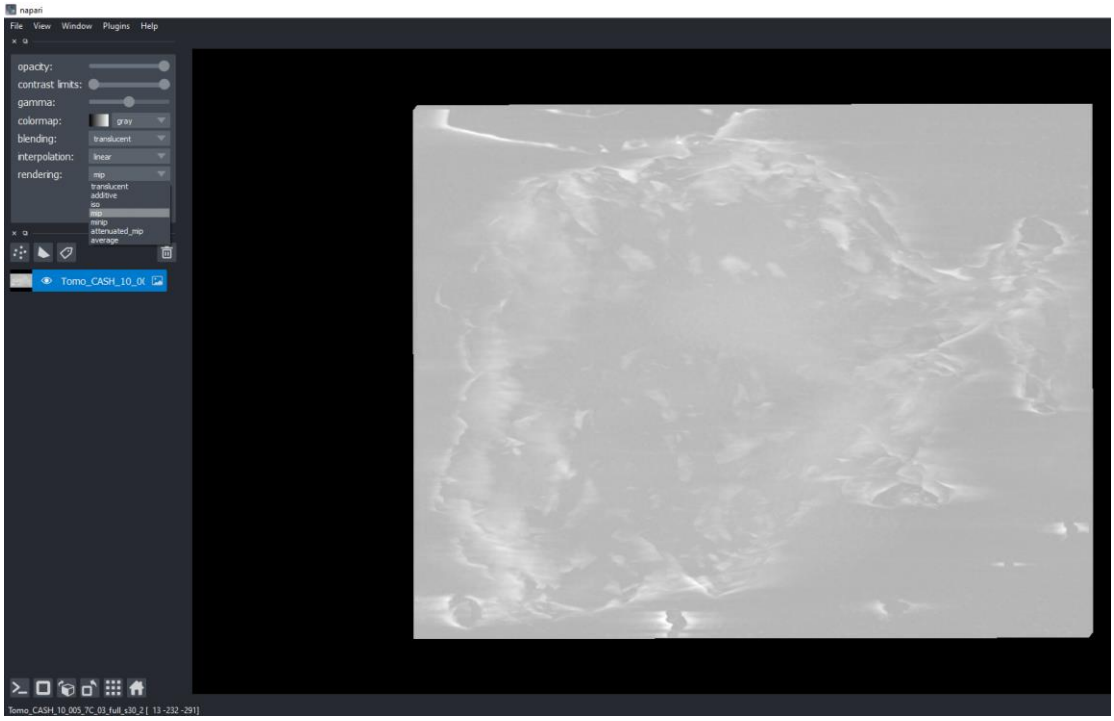

Figure 7.16 Set rendering package

3. Manually adjusting the contrast limits and gamma is required since the image characters will be appeared/disappeared based on these parameters. The example of model is shown in Figure 7.17.

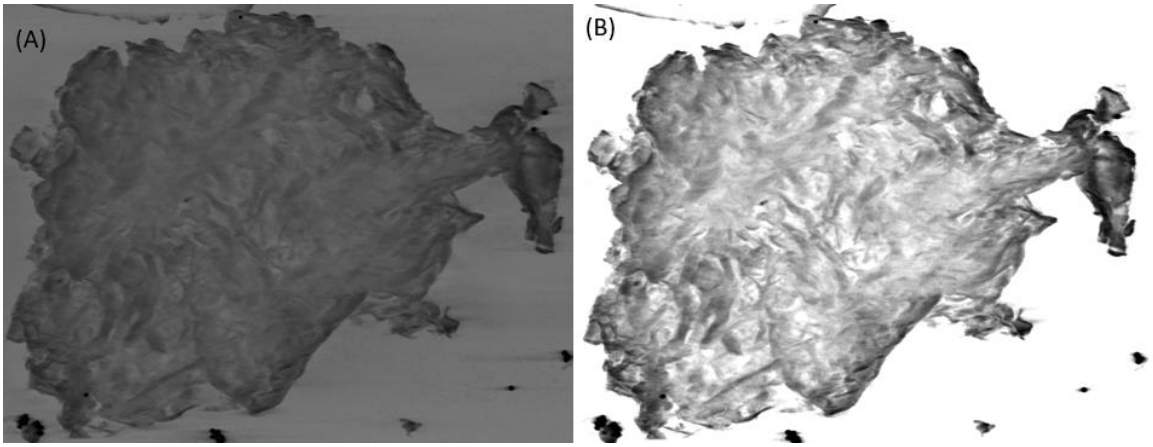

Figure 7.17 The 3D model of C-A-S-H at Ca/Si 1.0, Al/Si 0.05 at equilibrated temperature 7° C, before adjusting the contrast limits and gamma (A), After adjusting (B)

7.4 Particle and Pore Analysis with ImageJ

The main software in this session is Fiji (Fiji is an imageJ with plugins). Another important plugin that needed to be installed is Xlib (Münch & Holzer, 2008) which can downloaded from ftp://ftp.empa.ch/pub/empa/outgoing/BeatsRamsch/lib/ . After finish download, install from ImageJ Updater (Plugins > Install… > xlib_.jar). The new plugins can be found under Plugins > Beat.

1. Threshold data set
   - Go to Image > Adjust > Threshold. Then select the method that is appropriated (Figure 8.15).
   - Click “Convert to Mask”.
   - Check only “Calculate threshold for each image” then Click “OK”.
   - The result should be in black and white only (like Figure 8.16).

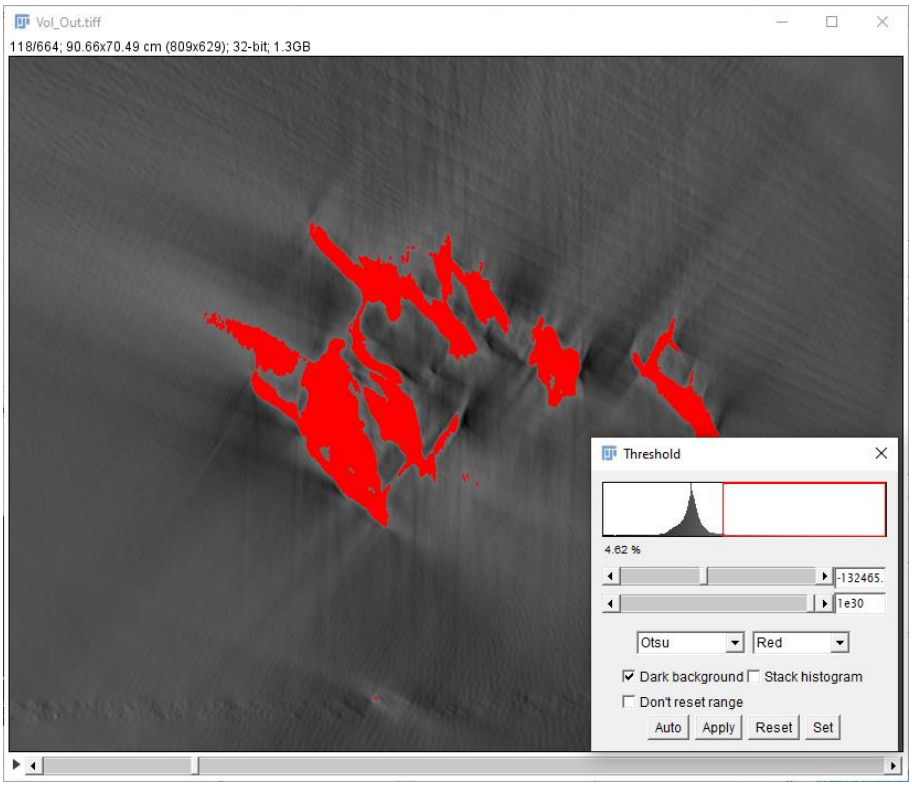

Figure 7.18 Threshold adjusting of C-S-H 1.0.

Figure 7.19 Threshold image of C-S-H 1.0.

2. Pore Size Distribution (Figure 7.20)
   - Go to Plugins > Beat > Pore Size Distribution
   - Choose “Continuous PSD” or “Discrete PSD”.
   - Check “Entire Stack Processing?” then select “3D PSD”.
   - Check “Write results to output files?” then select the location.
   - Click “OK”.
   - Wait for several minutes.
   - The result file is saved in the selected location.

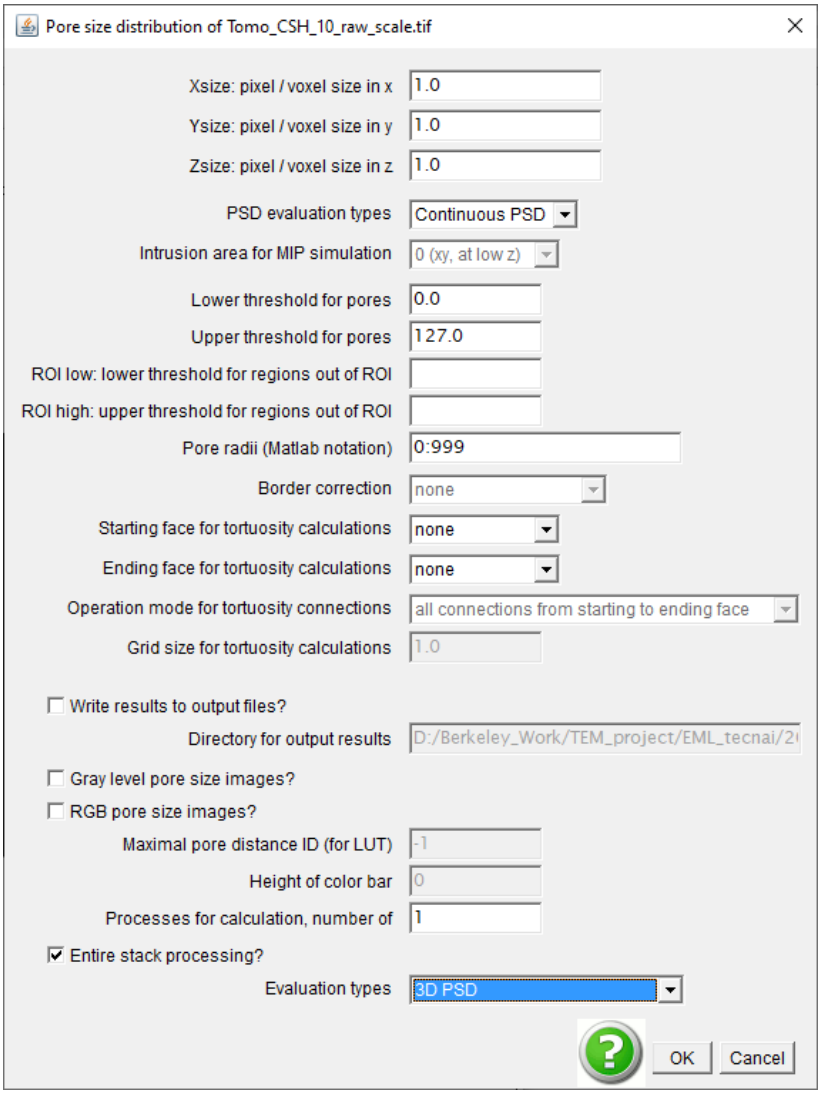

Figure 7.20 Pore Size Distribution in ImageJ

8. References

Abdolhosseini, Q., Mohammad, J., Ulm, F.-J., and Pellenq, R. J.-M. (2012). Evidence on the dual nature of aluminum in the calcium-silicate-hydrates based on atomistic simulations. *Journal of the American Ceramic Society*, *95*(3), 1128–1137.

Arslan, I., Yates, T. J. V., Browning, N. D., and Midgley, P. A. (2005). Embedded nanostructures revealed in three dimensions. *Science*, *309*(5744), 2195 LP – 2198.

Bae, S., Taylor, R., Hernández-Cruz, D., Yoon, S., Kilcoyne, D., and Monteiro, P. J. M. (2015). Soft x-ray spectromicroscopic investigation of synthetic C-S-H and C_3S hydration products. *Journal of the American Ceramic Society*, *98*(9), 2914–2920.

Bae, S., Taylor, R., Shapiro, D., Denes, P., Joseph, J., Celestre, R., Marchesini, S., Padmore, H., Tyliszczak, T., Warwick, T., Kilcoyne, D., Levitz, P., Monteiro, P. J. M., and Struble, L. (2015). Soft X-ray ptychographic imaging and morphological quantification of calcium silicate hydrates (C–S–H). *Journal of the American Ceramic Society*, *98*(12), 4090–4095.

Banthia, N., and Mindess, S. (1989). Water permeability of cement paste. *Cement and Concrete Research*, *19*(5), 727–736.

Berry, M. V., Gibbs, D. F., and Burch, C. R. (1970). The interpretation of optical projections. *Proceedings of the Royal Society of London. A. Mathematical and Physical Sciences*, *314*(1517), 143–152.

Bogue, R. H. (1947). *Chemistry of portland cement*. Reinhold.

Bonaccorsi, E., Merlino, S., and Kampf, A. R. (2005). The crystal structure of tobermorite 14 Å (plombierite), a C–S–H phase. *Journal of the American Ceramic Society*, *88*(3), 505–512.

Bonaccorsi, E., Merlino, S., and Taylor, H. F. W. (2004). The crystal structure of jennite, $Ca_9Si_6O_{18}(OH)_6{\cdot}8H_2O$. *Cement and Concrete Research*, *34*(9), 1481–1488.

Bossa, N., Chaurand, P., Vicente, J., Borschneck, D., Levard, C., Aguerre-Chariol, O., and Rose, J. (2015). Micro- and nano-X-ray computed-tomography: a step forward in the characterization of the pore network of a leached cement paste. *Cement and Concrete Research*, *67*, 138–147.

Bracewell, R. N., and Riddle, A. C. (1967). Inversion of fan-beam scans in radio astronomy. *The Astrophysical Journal*, 427–434.

Brandt, S. S. (2006). Markerless Alignment in Electron Tomography. In J. Frank (Ed.), *Electron Tomography: Methods for Three-Dimensional Visualization of Structures in the Cell* (pp. 187–215). Springer New York.

Bullard, J. W., Jennings, H. M., Livingston, R. A., Nonat, A., Scherer, G. W., Schweitzer, J. S., Scrivener, K. L., and Thomas, J. J. (2011). Mechanisms of cement hydration. *Cement and Concrete Research*, *41*(12), 1208–1223.

Dolado, J. S., and van Breugel, K. (2011). Recent advances in modeling for cementitious materials. *Cement and Concrete Research*, *41*(7), 711–726.

Doube, M., Kłosowski, M. M., Arganda-Carreras, I., Cordelières, F. P., Dougherty, R. P., Jackson, J. S., Schmid, B., Hutchinson, J. R., and Shefelbine, S. J. (2010). BoneJ: free and extensible bone image analysis in ImageJ. *Bone*, *47*(6), 1076–1079.

Ercius, P., Alaidi, O., Rames, M. J., and Ren, G. (2015). Electron tomography: a three-dimensional analytic tool for hard and soft materials research. *Advanced Materials*, *27*(38), 5638–5663.

Ercius, P., Weyland, M., Muller, D. A., and Gignac, L. M. (2006). Three-dimensional imaging of nanovoids in copper interconnects using incoherent bright field tomography. *Applied Physics Letters*, *88*(24), 243116.

Frank, J. (2008). *Electron tomography: methods for three-dimensional visualization of structures in the cell*. Springer.

Garboczi, E. J., and Bentz, D. P. (1992). Computer simulation of the diffusivity of cement-based materials. *Journal of Materials Science*, *27*(8), 2083–2092.

Gilbert, P. (1972). Iterative methods for the three-dimensional reconstruction of an object from projections. *Journal of Theoretical Biology*, *36*(1), 105–117.

Gilbert, P. F., and Aaron, K. (1972). The reconstruction of three-dimensional structure from projections and its application to electron microscopy II. direct methods. *Proceedings of the Royal Society of London. Series B. Biological Sciences*, *182*(1066), 89–102.

Gordon, R., Bender, R., and Herman, G. T. (1970). Algebraic reconstruction techniques (ART) for three-dimensional electron microscopy and X-ray photography. *Journal of Theoretical Biology*, *29*(3), 471–481.

Groves, G. W. (1981). Microcrystalline calcium hydroxide in Portland cement pastes of low water/cement ratio. *Cement and Concrete Research*, *11*(5–6), 713–718.

Groves, G. W., Le Sueur, P. J., and Sinclair, W. (1986). Transmission Electron Microscopy and Microanalytical Studies of Ion-Beam-Thinned Sections of Tricalcium Silicate Paste. *Journal of the American Ceramic Society*, *69*(4), 353–356.

Herman, G. T., Lent, A., and Rowland, S. W. (1973). ART: mathematics and applications: a report on the mathematical foundations and on the applicability to real data of the algebraic reconstruction techniques. *Journal of Theoretical Biology*, *42*(1), 1–32.

Hewlett, P., and Liska, M. (2019). *Lea's chemistry of cement and concrete*. Butterworth-Heinemann.

Holzer, L., Gasser, P., and Muench, B. (2006). Quantification of capillary pores and hadley grains in cement paste using FIB-nanotomography. In M. S. Konsta-Gdoutos (Ed.), *Measuring, Monitoring and Modeling Concrete Properties* (pp. 509–516). Springer Netherlands.

Huang, P. Y., Kurasch, S., Srivastava, A., Skakalova, V., Kotakoski, J., Krasheninnikov, A. V., Hovden, R., Mao, Q., Meyer, J. C., and Smet, J. (2012). Direct imaging of a two-dimensional silica glass on graphene. *Nano Letters*, *12*(2), 1081–1086.

Imbabi, M. S., Carrigan, C., and McKenna, S. (2012). Trends and developments in green cement and concrete technology. *International Journal of Sustainable Built Environment*, *1*(2), 194–216.

Jiang, H., Song, C., Chen, C.-C., Xu, R., Raines, K. S., Fahimian, B. P., Lu, C.-H., Lee, T.-K., Nakashima, A., and Urano, J. (2010). Quantitative 3D imaging of whole, unstained cells by using X-ray diffraction microscopy. *Proceedings of the National Academy of Sciences*, *107*(25), 11234–11239.

Königsberger, M., Hlobil, M., Delsaute, B., Staquet, S., Hellmich, C., and Pichler, B. (2018). Hydrate failure in ITZ governs concrete strength: a micro-to-macro validated engineering mechanics model. *Cement and Concrete Research*, *103*, 77–94.

Korpa, A., Kowald, T., and Trettin, R. (2009). Phase development in normal and ultra high performance cementitious systems by quantitative X-ray analysis and thermoanalytical methods. *Cement and Concrete Research*, *39*(2), 69–76.

Koster, A. J., Ziese, U., Verkleij, A. J., Janssen, A. H., and De Jong, K. P. (2000). Three-dimensional transmission electron microscopy: a novel imaging and characterization technique with nanometer scale resolution for materials science. *The Journal of Physical Chemistry B*, *104*(40), 9368–9370.

Kremer, J. R., Mastronarde, D. N., and McIntosh, J. R. (1996). Computer visualization of three-dimensional image data using IMOD. *Journal of Structural Biology*, *116*(1), 71–76.

Krivanek, O. L., Dellby, N., Nellist, P. D., Batson, P. E., and Lupini, A. R. (2001). Aberration-corrected STEM: The present and the future. *Microscopy and Microanalysis*, *7*(S2), 896–897.

Krivanek, O. L., Zhou, W., Chisholm, M. F., Dellby, N., Lovejoy, T. C., Ramasse, Q. M., Idrobo, J. C., Bell, D., and Erdman, N. (2013). Gentle STEM of single atoms: Low keV imaging and analysis at ultimate detection limits. *Low Voltage Electron Microscopy: Principles and Applications*, 119–161.

Kübel, C., Voigt, A., Schoenmakers, R., Otten, M., Su, D., Lee, T.-C., Carlsson, A., and Bradley, J. (2005). Recent advances in electron tomography: TEM and HAADF-STEM tomography for materials science and semiconductor applications. *Microscopy and Microanalysis*, *11*, 378–400.

LeBeau, J. M., Findlay, S. D., Allen, L. J., and Stemmer, S. (2008). Quantitative atomic resolution scanning transmission electron microscopy. *Physical Review Letters*, *100*(20), 206101.

Lee, E., Fahimian, B. P., Iancu, C. V, Suloway, C., Murphy, G. E., Wright, E. R., Castaño-Díez, D., Jensen, G. J., and Miao, J. (2008). Radiation dose reduction and image enhancement in biological imaging through equally-sloped tomography. *Journal of Structural Biology*,

164(2), 221–227.

Levin, B. D. A., Jiang, Y., Padgett, E., Waldon, S., Quammen, C., Harris, C., Ayachit, U., Hanwell, M., Ercius, P., Muller, D. A., and Hovden, R. (2018). Tutorial on the visualization of volumetric data using tomviz. *Microscopy Today*, *26*(1), 12–17.

Li, J., Geng, G., Myers, R., Yu, Y.-S., Shapiro, D., Carraro, C., Maboudian, R., and Monteiro, P. J. M. (2019). The chemistry and structure of calcium (alumino) silicate hydrate: A study by XANES, ptychographic imaging, and wide- and small-angle scattering. *Cement and Concrete Research*, *115*, 367–378.

Liu, Y., Penczek, P. A., McEwen, B. F., and Frank, J. (1995). A marker-free alignment method for electron tomography. *Ultramicroscopy*, *58*(3), 393–402.

Marks, L. D. (1999). Experimental studies of small particle structures. *Reports on Progress in Physics*, *57*, 603.

McDonald, P. J., Rodin, V., and Valori, A. (2010). Characterisation of intra- and inter-C–S–H gel pore water in white cement based on an analysis of NMR signal amplitudes as a function of water content. *Cement and Concrete Research*, *40*(12), 1656–1663.

Mehta, P. K., and Monteiro, P. J. M. (2014). *Concrete Microstructure, Properties, and Materials* (5th ed.). McGraw-Hill Companies.

Merlino, S., Bonaccorsi, E., and Armbruster, T. (2001). The real structure of tobermorite 11Å : normal and anomalous forms, OD character and polytypic modifications. *European Journal of Mineralogy*, *13*(3), 577–590.

Miao, J., Ercius, P., and Billinge, S. J. L. (2016). Atomic electron tomography: 3D structures without crystals. *Science*, *353*(6306), aaf2157.

Midgley, P. A., and Weyland, M. (2003). 3D electron microscopy in the physical sciences: the development of Z-contrast and EFTEM tomography. *Ultramicroscopy*, *96*(3–4), 413–431.

Mohan, K., and Taylor, H. F. W. (1982). A trimethylsilylation study of tricalcium silicate pastes. *Cement and Concrete Research*, *12*(1), 25–31.

Monteiro, P. J. M., Miller, S. A., and Horvath, A. (2017). Towards sustainable concrete. *Nature Materials*, *16*(7), 698–699.

Münch, B., and Holzer, L. (2008). Contradicting geometrical concepts in pore size analysis attained with electron microscopy and mercury intrusion. *Journal of the American Ceramic Society*, *91*(12), 4059–4067.

Navi, P., and Pignat, C. (1999). Three-dimensional characterization of the pore structure of a simulated cement paste. *Cement and Concrete Research*, *29*(4), 507–514.

Nyame, B. K., and Illston, J. M. (1981). Relationships between permeability and pore structure of hardened cement paste. *Magazine of Concrete Research*, *33*(116), 139–146.

Odgaard, A., and Gundersen, H. J. G. (1993). Quantification of connectivity in cancellous bone,

with special emphasis on 3-D reconstructions. *Bone*, *14*(2), 173–182.

Otsu, N. (1979). A threshold selection method from gray-level histograms. *IEEE Transactions on Systems, Man, and Cybernetics*, *9*(1), 62–66.

Patel, R. A. (2016). *Lattice Boltzmann method based framework for simulating physico-chemical processes in heterogeneous porous media and its application to cement paste*. Ghent University.

Patel, R. A., Perko, J., Jacques, D., De Schutter, G., Van Breugel, K., and Ye, G. (2014). A versatile pore-scale multicomponent reactive transport approach based on Lattice Boltzmann method: application to portlandite dissolution. *Physics and Chemistry of the Earth, Parts A/B/C*, *70–71*, 127–137.

Patel, R. A., Perko, J., Jacques, D., De Schutter, G., Ye, G., and Van Bruegel, K. (2018). Effective diffusivity of cement pastes from virtual microstructures: role of gel porosity and capillary pore percolation. *Construction and Building Materials*, *165*, 833–845.

Penczek, P. A. (2010). Chapter One - Fundamentals of Three-Dimensional Reconstruction from Projections. In G. J. B. T.-M. in E. Jensen (Ed.), *Cryo-EM, Part B: 3-D Reconstruction* (Vol. 482, pp. 1–33). Academic Press.

Pennycook, S. J. (1989). Z-contrast STEM for materials science. *Ultramicroscopy*, *30*(1–2), 58–69.

Phair, J. W. (2006). Green chemistry for sustainable cement production and use. *Green Chemistry*, *8*(9), 763–780.

Popvics, S. (1973). Method for developing relationships between mechanical properties of hardened concrete. *Journal Proceedings*, *70*(12), 795–798.

Reimer, L., and Kohl, H. (2008). Scattering and Phase Contrast. In *Transmission Electron Microscopy: Physics of Image Formation* (pp. 193–269). Springer New York.

Richardson, I. G. (1999). The nature of C-S-H in hardened cements. *Cement and Concrete Research*, *29*(8), 1131–1147.

Richardson, I. G. (2000). Nature of the hydration products in hardened cement pastes. *Cement and Concrete Composites*, *22*(2), 97–113.

Richardson, I. G. (2002). Electron microscopy of cements. In *Structure and Performance of Cements* (pp. 500–556). Spon Press: London.

Richardson, I. G. (2004). Tobermorite/jennite- and tobermorite/calcium hydroxide-based models for the structure of C-S-H: applicability to hardened pastes of tricalcium silicate, β-dicalcium silicate, portland cement, and blends of portland cement with blast-furnace slag, metakaol. *Cement and Concrete Research*, *34*(9), 1733–1777.

Richardson, I. G. (2008). The calcium silicate hydrates. *Cement and Concrete Research*, *38*(2), 137–158.

Richardson, I. G., and Groves, G. W. (1992). Models for the composition and structure of calcium silicate hydrate (C-S-H) gel in hardened tricalcium silicate pastes. *Cement and Concrete Research*, *22*(6), 1001–1010.

Richardson, I. G., and Groves, G. W. (1993). The incorporation of minor and trace elements into calcium silicate hydrate (C-S-H) gel in hardened cement pastes. *Cement and Concrete Research*, *23*(1), 131–138.

Richardson, I. G., Skibsted, J., Black, L., and Kirkpatrick, R. J. (2010). Characterisation of cement hydrate phases by TEM, NMR and Raman spectroscopy. *Advances in Cement Research*, *22*(4), 233–248.

Saghi, Z., Xu, X., and Möbus, G. (2008). Three-dimensional metrology and fractal analysis of dendritic nanostructures. *Phys. Rev. B*, *78*(20), 205428.

Scherzer, O. (1936). Some defects of electron lenses. *Journal of Physics*, *101*(9–10), 593–603.

Scherzer, O. (1947). Spharische und chromatische Korrektur von Elektronen-Linsen. *Optik*, *2*, 114–132.

Scott, M. C., Chen, C.-C., Mecklenburg, M., Zhu, C., Xu, R., Ercius, P., Dahmen, U., Regan, B. C., and Miao, J. (2012). Electron tomography at 2.4-ångström resolution. *Nature*, *483*, 444.

Scrivener, K. L., Crumbie, A. K., and Laugesen, P. (2004). The interfacial transition zone (ITZ) between cement paste and aggregate in concrete. *Interface Science*, *12*(4), 411–421.

Scrivener, K. L., and Nonat, A. (2011). Hydration of cementitious materials, present and future. *Cement and Concrete Research*, *41*(7), 651–665.

Sofroniew, N., Lambert, T., Evans, K., Winston, P., Nunez-Iglesias, J., Bokota, G., Yamauchi, K., Solak, A. C., ziyangczi, Buckley, G., Bussonnier, M., Pop, D. D., Peña-Castellanos, G., Tung, T., Hilsenstein, V., Hector, Freeman, J., Boone, P., alisterburt, … Bryant. (2021). *napari/napari: 0.4.6rc1*.

Song, Y., Davy, C. A., Troadec, D., and Bourbon, X. (2019). Pore network of cement hydrates in a high performance concrete by 3D FIB/SEM — implications for macroscopic fluid transport. *Cement and Concrete Research*, *115*, 308–326.

Talon, L., Bauer, D., Gland, N., Youssef, S., Auradou, H., and Ginzburg, I. (2012). Assessment of the two relaxation time Lattice-Boltzmann scheme to simulate stokes flow in porous media. *Water Resources Research*, *48*(4).

Taylor, H. F. W. (1992). Tobermorite, jennite, and cement gel. In *Zeitschrift für Kristallographie - Crystalline Materials* (Vol. 202, p. 41).

Taylor, H. F. W. (1997). *Cement Chemistry, 2nd edition*. Thomas Telford.

Taylor, R., Richardson, I. G., and Brydson, R. M. D. (2010). Composition and microstructure of 20-year-old ordinary portland cement–ground granulated blast-furnace slag blends containing 0 to 100% slag. *Cement and Concrete Research*, *40*(7), 971–983.

Taylor, R., Sakdinawat, A., Chae, S. R., Wenk, H.-R., Levitz, P., Sougrat, R., and Monteiro, P. J. M. (2015). Developments in TEM nanotomography of calcium silicate hydrate. *Journal of the American Ceramic Society*, *98*(7), 2307–2312.

Thomas, J. J., Jennings, H. M., and Allen, A. J. (2010). Relationships between Composition and Density of Tobermorite, Jennite, and Nanoscale $CaO{-}SiO_2{-}H_2O$. *The Journal of Physical Chemistry C*, *114*(17), 7594–7601.

Trusilewicz, L., Fernández-Martínez, F., Rahhal, V., and Talero, R. (2012). TEM and SAED characterization of metakaolin. pozzolanic activity. *Journal of the American Ceramic Society*, *95*(9), 2989–2996.

U.S. Geological Survey. (2018). *Cement Statistics and Information*. https://minerals.usgs.gov/minerals/pubs/commodity/cement/

Uhlemann, S., and Haider, M. (1998). Residual wave aberrations in the first spherical aberration corrected transmission electron microscope. *Ultramicroscopy*, *72*(3–4), 109–119.

Vichit-Vadakan, W., and Scherer, G. W. (2003). Measuring permeability and stress relaxation of young cement paste by beam bending. *Cement and Concrete Research*, *33*(12), 1925–1932.

Williams, D. B., and Carter, C. B. (2009). *The Instrument BT - Transmission Electron Microscopy: A Textbook for Materials Science* (D. B. Williams & C. B. Carter (eds.); pp. 141–171). Springer US.

Wong, H. S., Zobel, M., Buenfeld, N. R., and Zimmerman, R. W. (2009). Influence of the interfacial transition zone and microcracking on the diffusivity, permeability and sorptivity of cement-based materials after drying. *Magazine of Concrete Research*, *61*(8), 571–589.

Yang, J., Hou, D., and Ding, Q. (2018). Structure, dynamics, and mechanical properties of cross-linked calcium aluminosilicate hydrate: a molecular dynamics study. *ACS Sustainable Chemistry & Engineering*, *6*(7), 9403–9417.

Ye, G. (2005). Percolation of capillary pores in hardening cement pastes. *Cement and Concrete Research*, *35*(1), 167–176.

Zalzale, M., McDonald, P. J., and Scrivener, K. L. (2013). A 3D lattice Boltzmann effective media study: understanding the role of C-S-H and water saturation on the permeability of cement paste. *Modelling and Simulation in Materials Science and Engineering*, *21*(8), 85016.

Zhou, Q., Milestone, N. B., and Hayes, M. (2006). An alternative to portland cement for waste encapsulation—the calcium sulfoaluminate cement system. *Journal of Hazardous Materials*, *136*(1), 120–129.

Zuber, B., and Marchand, J. (2000). Modeling the deterioration of hydrated cement systems exposed to frost action: Part 1: Description of the mathematical model. *Cement and Concrete Research*, *30*(12), 1929–1939.